Optofluidic Biolasers in Tissues: Applications in Biology and Biomedicine

by

Yu-Cheng Chen

A dissertation submitted in partial fulfillment
of the requirements for the degree of
Doctor of Philosophy
(Biomedical Engineering)
in the University of Michigan
2017

Doctoral Committee:

Professor Xudong Fan, Chair
Professor Somin E. Lee
Professor Allen P. Liu
Professor Ariella Shikanov
Professor Zhen Xu

Yu-Cheng Chen

yucchen@umich.edu

ORCID iD: 0000-0002-0008-5601

Dedication

To my parents, and my brother for all their love, encouragement, sacrifice, and putting me through the best education possible. I would not have been able to get to this stage without them.

To my grandpa, for his kindness and support, this is what I had promised him before he left. I would not have gotten through this doctorate if it were not for him.

Acknowledgements

First and foremost, I would like to express the deepest appreciation to my committee chair Professor Xudong Fan, who has the attitude and the substance of a genius: he continually and convincingly conveyed a spirit of adventure in regard to research and scholarship, and wisdom in regard to teaching. Without his guidance, precious time, and persistent support this dissertation would not have been possible. Besides, I am grateful to have excellent labmates who have provided extremely helpful resources to my study.

I would also like to acknowledge my committee members, Professor Ariella Shikanov, Professor Somin Lee, Professor Allen Liu, and Professor Zhen Xu, who were always willing to spend time to have discussion and share their academic careers with me. Their encouragement and advices have helped me a lot not only in my Ph.D. study but also in my future career. Financial support for my Ph.D. program was provided by the University of Michigan, NSF ECCS-1607250 and National Institutes of Health (1R21EB016783)

Finally, I would like to thank my family, my dearest friends, and especially my grandpa. It was my grandpa who triggered me to complete this degree in such a short time, and who always gave me the inspiration of this research. Although he passed away during the half way of my PhD journey, I would like to devote my highest respect to him.

TABLE OF CONTENTS

List of Figures

Abstract

Biolaser are an emerging technology for next generation biochemical detection and clinical applications. Laser-based detection offers the distinct advantages over fluorescence-based detection in terms of signal amplification, narrow linewidth, and strong intensity, leading to orders of magnitude increase in detection sensitivity. Recent advances have been made to achieve lasing from biomolecules and single cells. Tissues, which consist of cells embedded in extracellular matrix, mimic more closely the actual complex biological environment in living bodies, and thus are of more practical significance in medicine. The aim of this research is to develop optofluidic biolasers at the tissue level in order to provide a novel analytical tool for a wide range of biological and biomedical applications.

During my research, several types of micro-laser cavities, such as optofluidic ring resonators and high-Q Fabry-Pérot resonators were implemented to achieve lasing in tissues. Distinct and controllable laser emissions from various tissues thus enable highly multiplexed/multifunctional detection with superior contrast and high spectral/spatial resolution. In terms of biological applications, we first demonstrated chlorophyll lasing with intrinsic gain medium extracted from leaves, suggesting the possibility to lase with natural biological tissues. In addition, we developed a versatile tissue laser platform in which biological tissues were doped with different dyes and sandwiched within a high-Q Fabry-Perot cavity. Detailed investigation on how tissue structure/geometry, tissue thickness, and staining dye concentration affect the tissue laser was conducted.

To signify potential implementations of the tissue lasers in biomedicine, lasing in two major types of clinical tissues were investigated, including liquid biopsy and surgical biopsy. Herein, we demonstrated the first "blood laser" using the only FDA approved near infrared dye, Indocyaine Green, in human whole blood with the ICG concentration within the normal range of clinical dosage. Furthermore, we developed the first "laser emission-based microscope" (LEM) for improved cancer evaluation by mapping the lasing emissions from nuclear biomarkers in human lung and colon cancer tissues. As a proof-of-concept, tissue samples from patients labelled with cancer biomarkers were tested while an excitation laser beam was scanned to build a laser-emission image. It is found that nuclei in the cancer and normal tissues have vastly different lasing thresholds due to different expressions of nucleic acids and nuclear proteomic biomarkers, which enables the LEM to distinguish, with a high contrast, the cancer and normal tissues, and the cancer tissues with and without nuclear proteomic biomarkers. Significantly, the LEM has demonstrated a great potential to diagnose early stage cancer tissues with a high sensitivity of 97.5%. We also presented the wavelength-multiplexed immuno-lasing capability of LEM. As a final remark, we achieved lasing in living neurons/neuronal networks and employed laser emission to detect the subtle transients of intracellular calcium dynamics in neurons *in vitro*. Calcium imaging and recording of spontaneous neuronal activities were demonstrated with the "neuron lasing" method, in which the relative changes were significantly improved 1000 fold compared to fluorescence-based measurement. This thesis marks a critical step towards eventual clinical and biomedical applications of optofluidic biolasers, which may find broad use in precision medicine with on-chip cancer screening and immunodiagnostics, as well as in brain-on-chip devices, neuro-analysis, tissue engineering, and fundamental cell biology.

Chapter 1

Introduction

1.1. Optofluidic biolasers

Optofluidic biolasers are an emerging technology for next generation biochemical detection and clinical applications. In particular, optofluidic biolasers are a class of lasers in which the gain medium is composed of biologically related materials submerged in a liquid environment and integrated with a micro-laser cavity[1-6]. With the development of micro-fabrication technology, various types of bio-compatible cavities have been developed for biolasers such as ring resonator[7], Fabry-Pérot cavity (FP)[8,9], distributed feedback laser cavity[10], microsphere resonator[11], photonic crystal[12], and random laser cavity[13], as shown in Fig. 1.1. Additionally, there exist numerous types of gain media compatible with liquid and biological environments such as fluorescent compounds (luciferin[14], vitamins[15], and dyes[16]), natural fluorescent proteins[17-19], and quantum dots[20,21].

In particular, one of the most prominent applications for the optofluidic biolaser is the highly sensitive bioanalysis[5,6,22]. Fig. 1.2 illustrates the major differences between the conventional fluorescence-based and the laser-based bioanalysis. In the conventional detection, the fluorescent sample is in a cuvette or on a glass slide. Fluorescence (*i.e.*, spontaneous emission) is used as the sensing signal. A small change in the underlying biological process/interaction leads to a small change in fluorescence, which may be undetectable due to the omnipresent background noise. In contrast, in the optofluidic laser based detection, the fluorescent sample is placed inside a laser cavity and becomes part of the laser (as the laser gain medium). Rather than fluorescence, the laser

emission (*i.e.*, stimulated emission) is used as the sensing signal. Thanks to the strong optical feedback provided by the cavity, a small change in the gain induced by the underlying biological

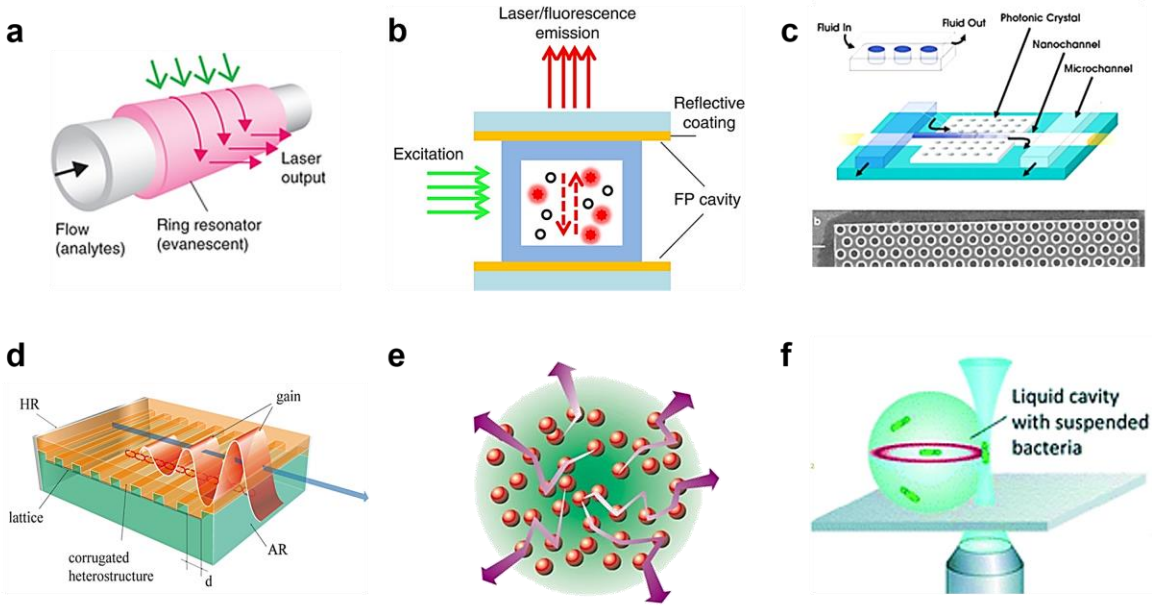

Figure 1.1. Biolasers with different optical cavities. (**a**) Optofluidic ring resonator[23]. (**b**) Fabry-Perot mirror cavity[9]. **(c)** Photonic crystal based biolaser integrated with microfluidics[24]. **(d)** Distributed feedback biolaser[25]. **(e)** Random laser without external cavity. **(f)** Microsphere/droplet based whispering gallery mode laser[17].

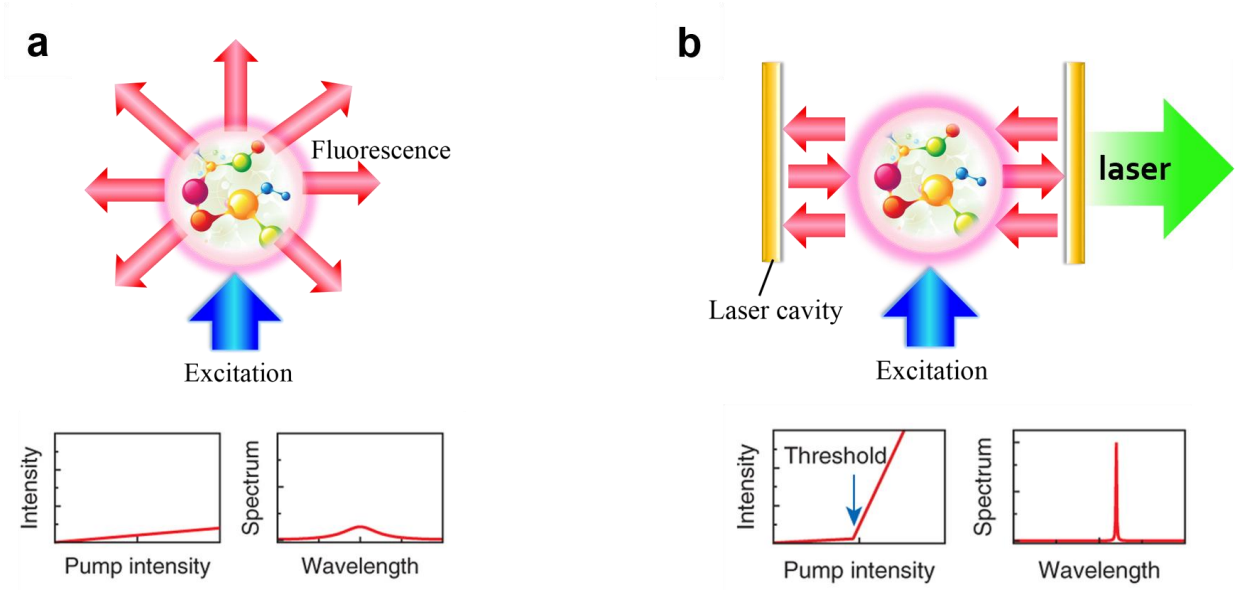

Figure 1.2. Comparison between conventional fluorescence-based and laser-based detection. (a) Fluorescence based method does not have threshold behavior and the spectrum is usually very broad. Laser based method provides a lasing threshold and narrow linewidth (<1 nm).[6]

processes/interaction are significantly amplified, leading to a drastic change in the laser output characteristics (*e.g.*, intensity, lasing threshold, emission directionality, and spatial mode distribution). Through recent theoretical analysis and experimental work , optofluidic biolasers have revealed the distinct advantages in signal amplification[26,27], narrow linewidth[14,28], and strong intensity without fluorescence or scattering background[29], leading to huge increase in detection sensitivity (>100X) and improved signal-to-noise ratios (>1000X) over the fluorescence based detection[30-32]. The significantly enhanced sensitivity and multi-parameter analysis further enables us to analyze minute changes in biomolecules, cells, and tissues, with a huge potential for biological and medical applications.

Taking a closer look at the basic principles of optofluidic biolasers, an optofluidic biolaser consists of three essential components: (i) a gain medium in the fluidic environment, (ii) an optical cavity and (iii) pumping. The photons emitted from the gain medium are trapped by the cavity, and the optical feedback induces stimulated emission. When a sufficient number of gain molecules in the cavity are excited by pumping, the available gain becomes greater than the total loss in the cavity, and laser oscillation builds up. The lasing threshold condition is expressed as

$$n_1\sigma_e(\lambda) = n_0\sigma_a(\lambda) + \gamma_c,$$

where n_1 and n_0 are the concentration of the gain molecules in the excited and ground state, respectively. σ_e and σ_a are the emission and absorption cross-section of the molecule, respectively, at the lasing wavelength λ. γ_c is the cavity-loss coefficient. Below the threshold, the output through the highly reflecting mirror comprises only weak spontaneous fluorescence emission. Above the threshold, the output intensity increases dramatically as coherent stimulated emission builds up

and grows linearly with the pump energy with a much greater slope than that of fluorescence emission[6] (see Fig. 1.2).

The lasing threshold can be reached with sufficient pumping, which relies on several parameters, such as the emission cross-section (σ_e), the concentration of fluorophores (n_1) in the excited states, the absorption cross-section (σ_a) ,the cavity loss (γ_c), and Q-factor of the laser cavity. In particular, the Q-factor, or cavity quality factor determines the cavity's capability to trap photons, A higher Q-factor means a lower concentration of gain molecules and lower pump energy are required to reach the threshold. In an optofluidic biolaser, these parameters can vary in response to specific biomolecular interactions and conformation changes. In turn, monitoring the changes in the laser output characteristics such as intensity, spectrum and threshold allows the underlying biochemical and biological processes to be revealed.

To date, optofluidic biolasers have been extensively demonstrated at the molecular level for highly sensitive biomolecular detection, including lasing with fluorescent proteins[17], DNA[33], and fluorescent products generated by enzyme-substrate reactions[9]. In addition, fluorescence resonance energy transfer (FRET) lasing has also been successfully demonstrated[18] via protein pairs, whose lasing efficiencies can be modulated by underlying biological interactions. Commercial dye labeled DNA Holliday junction has also shown FRET lasing capability in a bio-switchable manner[34]. Recently, biolasers based on single cells using fluorescent proteins synthesized directly inside cells or externally added/labeled dyes as the gain medium *in-vitro* have also been accomplished[35]. Figure 1.3(a) shows the single cellular lasing with green fluorescent proteins (gfp) synthesized within the cell when the cells are placed between a FP microcavity. Besides using an external cavity, standalone cellular lasers has also been demonstrated by using intracellular micro-resonators and suitable optical gain materials[36], as shown in Fig. 1.3 (b). These

results suggest that the lasing modes can be used to analyze cell structures and gain distribution[37-40]. However, all the cellular lasers developed to date are merely a laser embodiment in cells which do not carry any biofunctions, *i.e.*, their gain media are not designed to be modulated by (or respond to) biological interactions inside cells, and therefore, cannot be used for sensitive biosensing[35,37].

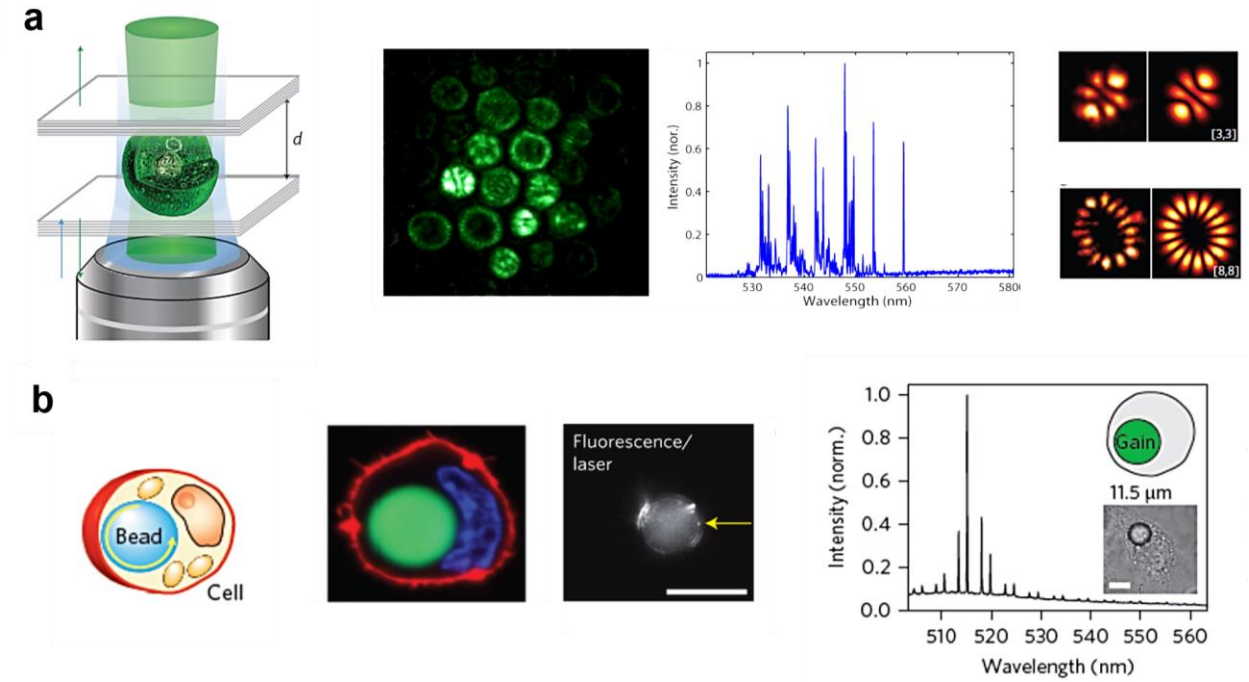

Figure 1.3. Cellular lasers. (**a**) Single cellular laser demonstrated by using cell expressed with GFP sandwiched between two mirrors (F-P cavity). The lasing spectrum and CCD images of laser modes are also shown on the right panel. (**b**) Intracellular microlasers with fluorescent PS micobead in the cell body. Here the microbead serves as the WGM lasing cavity. The second image shows the PS bead in green, while the laser emission and spectrum are also given on the right panel.

1.2. Motivation for lasing in tissues

Moving to the next biological hierarchy, detailed characterization of tissues, which consists of a collection of cells embedded in extracellular matrix, is generally considered to be more practical since it mimics the actual complex biological environment in a living body. As a result, lasing in tissue (tissue lasers) is particularly significant for a broad range of applications such as

tissue engineering and medical diagnosis. Given that tissue-based lasers have been studied in the past by using random laser cavities[41-43], the random lasers are incapable of providing repeatable, trackable, and precise laser emission signals. Due to the lack of the fixed external cavities. Moreover, random lasers are unable to detect biochemical/biological reactions from specific targets (*e*,*g*., antibodies), as the underlying lasing mechanism is mainly based on the physical properties of tissues (inhomogeneities).

The challenges of tissue lasers described above motivated us to explore and develop an analytical platform capable of detection with lasing signals in a biological tissue, which can broadly be applied to a variety of targets, tissues, and diseases. Therefore, this thesis is aimed to develop optofluidic biolasers consisting of fluorescent biosensors as the gain medium inside tissue, which responds to intratissue or intercellular activities for tissue analysis (liquid biopsy and surgical biopsy). The unique spectral and spatial characteristics of the laser output will be used to better understand minute interactions within tissues with a superior sensitivity and imaging quality than fluorescence counterparts. The significance of this thesis is to pioneer a novel on-chip device for future medical diagnostics, examination of excised tissues, and image-guided surgery, as well as monitoring and differentiating of biological transformations in tissue engineering.

1.3. Types of high-Q optical cavities

In order to develop tissue lasers for various biological and medical applications, different types of optical cavities are available. In particular, here we would like to introduce two types of high-quality factor (high-Q) micro-cavities which enable us to implement tissue diagnostics for liquid biopsy (whole blood, sweat, urine, saliva) and surgical biopsy (excised tumor, skin lesions).

For a liquid biopsy, optofluidic ring resonator (OFRR) is an ideal device for optofluidic tissue laser as given in Fig. 1.4(a). OFRR is a piece of thin-walled glass capillary waveguide with a closed loop[44], which supports the circulating resonant waveguide mode or whispering gallery mode (WGM) by total internal reflection of light at the curved boundary. The resonant light circulates along the OFRR and has evanescent field into the surrounding medium, thus interacts repetitively with the liquid or analytes near the resonator surface, to provide the optical feedback for biological samples to lase. The intrinsic compatibility with microfluidics and high Q factor of OFRR makes it of great advantage to a low lasing threshold while low energy operation is particularly important for biological applications. Most importantly, the ring resonator devices take the advantage of small footprint, enabling large scale integration to lab-on-chip devices for point-of-care diagnostics.

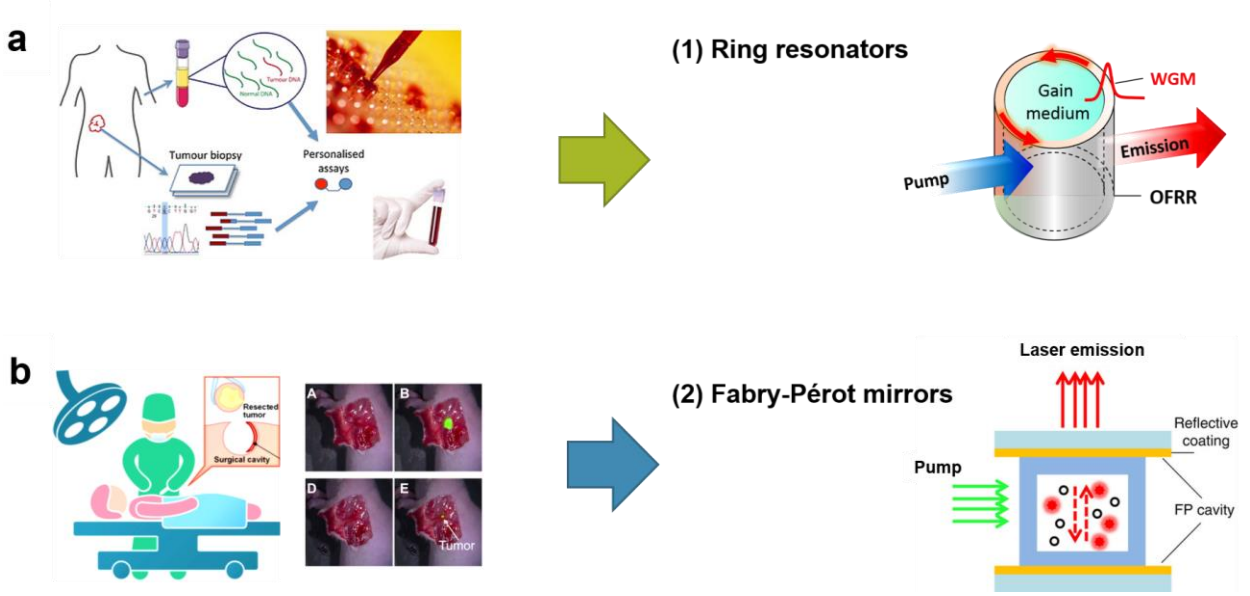

Figure 1.4. Optical cavities for different biopsy samples. (**a**) Liquid biopsy- whole blood, which has high potential for non-invasive molecular disease detection on chip. An optofluidic ring resonator which supports WGM lassing is plotted on the right panel. **(b)** Surgical biopsy- excised cancer tissue. An example of FP cavity formed by two high reflectivity dielectric mirrors is plotted on the right panel.

For a surgical biopsy, Fabry-Pérot (FP) cavities which consist of two highly reflective parallel mirrors has advantages regards to the ease of implementation and the planar format[45-51], as shown in Fig. 1.4(b). Additionally, FP cavity provides a whole-body interaction between the electromagnetic field and the gain medium, *i.e*., a predominant portion of the optical field is within the body of the gain medium, in contrast to the evanescent interaction such as in ring resonators. This arrangement is particularly important when the gain medium is inside a specific localization of cell or tissue. The gain media here can be either cellular networks or solid tissue labeled with fluorescent compounds, which are designed to respond to cellular activities, thus producing the sensing signal that is then amplified by the laser cavity. Furthermore, the integration with an imaging spectrometer will allow us to accomplish laser emission-based tissue mapping with improved spectral resolution and spatial information.

1.4. Organization of thesis

In this thesis, we explored and achieved lasing in several types of tissues by utilizing various micro-laser cavities. Furthermore, our work opens the new field to implement laser emission in biomedical imaging for improved cancer evaluation. This study marks a critical step towards eventual clinical and biomedical applications of optofluidic biolasers, which provides a novel tool for on-chip diagnostics in blood, cancer screening, immuno-diagnosis, and better understanding of fundamental cell biology.

For Chapter 2 and 3, lasing in biological tissues by using an optofluidic ring resonator were demonstrated. In Chapter 2, we first show optofluidic chlorophyll lasers with intrinsic gain medium extracted from leaf, indicating the possibility to lase with natural biological tissues (published in *Lab Chip*, 2016)[52]. In Chapter 3, we carried out a systematic investigation on ICG

lasing in human whole blood, which represents the first optofluidic biolasers using FDA approved fluorophores (published in *Optica*, 2016)[30]. From Chapter 4 to 6, we developed tissue-based lasers with a FP cavity, in which the tissues/cells were sandwiched between two dielectric mirrors. In Chapter 4, we demonstrated the first FP tissue laser and its multiplexing capability labeled with non-specific fluorophores. We further investigated how the tissue structure/geometry, tissue thickness, and staining dye concentration affect the tissue laser (published in *Lab Chip*, 2017)[29]. Based on the similar concept, Chapter 5 proposes a novel imaging tool for high contrast cancer screening and immuno-diagnosis. In Chapter 5, the first scanning-based "laser emission-based microscope" (LEM) was developed for improved cancer evaluation by mapping the lasing emissions from nuclear biomarkers in human tissues (published in *Nature Biomed. Eng.*, 2017)[53]. Finally, we present an ongoing work in Chapter 6 which shows the potential to monitor living biological networks/tissues using laser scheme. Lasing in living neurons and neuronal networks with a sub-cellular/single-spike resolution were demonstrated to monitor the intracellular calcium dynamics during spontaneous neuronal activities. To conclude, Chapter 7 covers a brief summary and outlook towards future biological and medical applications of biolasers in tissues.

Chapter 2

Bioinspired Lasers with Chlorophylls from Leaf Tissue

As the first attempt, we used natural plant leaf tissues to demonstrate the feasibility of optofluidic laser in tissue, using intrinsic auto-fluorescent compounds in leaves- chlorophylls, as the gain media for lasing (Fig. 2.1(a)). Chlorophylls are essential for photosynthesis and also one of the most abundant pigments on earth[54,55]. Using the optofluidic ring resonator of extremely high Q-factors (>10^7), we investigated unique characteristics and revealed the underlying mechanism of chlorophyll lasers. The first demonstration of chlorophyll lasers with two lasing bands were achieved for the first time in isolated chlorophyll *a* (Chla). Detailed theoretical analysis, elucidated the mechanism that determines when and why the laser emission band appears at one of the two bands, or concomitantly at both bands. Finally, Chla was exploited as the donor in fluorescence resonance energy transfer with an unprecedented wavelength shift as large as 380 nm.

2.1. Motivation

Chlorophylls are not only essential for photosynthesis and genetic engineering, but also particularly important for regulating metabolic functions in living organisms[54,55]. Chlorophyll fluorescence has been extensively studied for fundamental understanding of energy transfer mechanisms inside chloroplasts[56,57]. Two bands of emission corresponding to the (0,0) and (0,1) vibronic regions of the $S_1 \rightarrow S_0$ transition are usually observed[58,59] , as shown in Fig. 2.1(b). The quantum yield of most chlorophylls is approximately 30% [60,61], similar to that of other organic dyes such as Cy5, Cy5.5, and Alexa Fluor 647. The strong fluorescent capability of chlorophylls

suggests that they can possibly be used as the laser gain medium. In turn, stimulated emission of chlorophylls provides insight into the energy transfer processes during photosynthesis. It can also be used to better understand the S_1 electronic states and interpret fluorescence results (such as intensity dependent fluorescence lifetime and quantum yield) [62].

In comparison with many other laser gain media, chlorophylls are biocompatible and biodegradable, making them very attractive in *in-vitro* and *in-vivo* sensing applications. Meanwhile, the unique dual-absorption bands in the visible spectrum (Fig. 2.1(c)) with extremely high extinction coefficients (~10^5 $M^{-1}cm^{-1}$ at 430 nm) render chlorophylls excellent light harvesting capability to achieve lower lasing thresholds. This characteristic, together with the large Stokes shift, suggests that chlorophylls can serve as an excellent donor in a fluorescence resonance energy transfer (FRET) laser, which allows implementation of a laser in the red or near infrared (NIR) spectrum with blue or ultra-violet (UV) excitation.

The laser of chlorophylls was briefly studied nearly 40 years ago using a low quality optical cavity based on a 1-cm long cuvette[62], whose Q-factor (Q) and finesse (F) were only 1.3x10^5 and 6, respectively. However, while laser emission at the 680 nm band was observed, which corresponds to the (0,1) vibronic region, no laser emission was found around 730 nm and the mechanism behind the missing 730 nm band was not fully understood. Here we investigated both experimentally and theoretically the optofluidic laser using chlorophyll *a* as the gain medium and a thin-walled glass capillary based optofluidic ring resonator (OFRR, Fig. 2.1(d)) as the laser microcavity. The purposes of this work were two-fold. First, we aimed to develop novel chlorophyll based optofluidic lasers using chlorophyll as the outstanding gain medium and the donor. Second, we took advantage of the extremely high Q-factor (>10^7) and finesse (F~10^4) of the OFRR to study unique characteristics and reveal the mechanism of chlorophyll lasers.

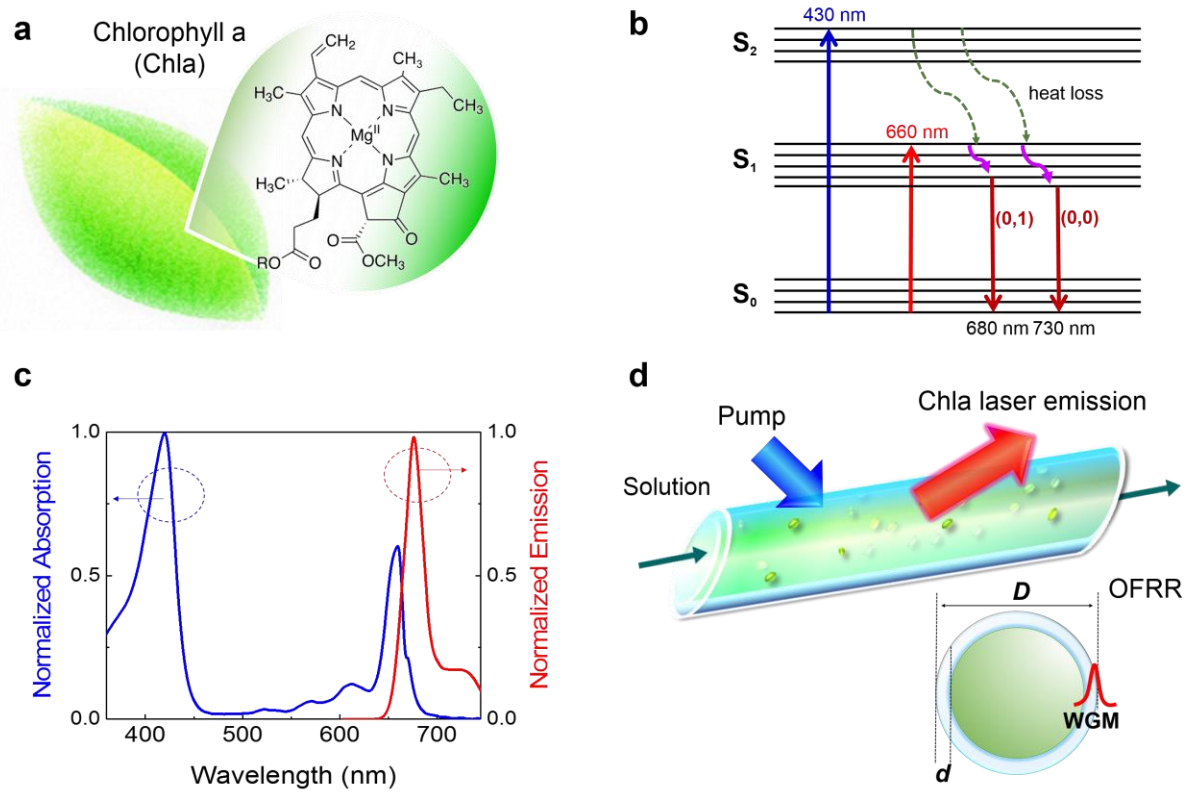

Figure 2.1. Optical properties of chlorophylls. (**a**) Molecular structure of chlorophyll *a* (Chla) extracted from spinach leaves. (**b**) Energy level of Chla. S_0 stands for ground state, S_0 stands for the first excited state, and S_2 stands for higher excited states. Chla absorbs photons around 430 nm and 660 nm, whereas the emission bands at 680 nm and 730 nm in our experiment correspond to the (0,0) and (0,1) vibronic regions in the $S_1 \rightarrow S_0$ transition, which are related to Photosystem II and I in chloroplasts, respectively. (**c**) Normalized absorption and emission spectrum of Chla in ethanol. (**d**) Schematic diagram of the chlorophyll laser using a high Q-factor optofluidic ring resonator (OFRR). Green particles represent the chlorophyll molecules dissolved in ethanol. The laser was excited by a pulsed optical parametric oscillator (OPO) (wavelength=430 nm). The diagram on the right side shows the profile of the OFRR and the whispering gallery mode (WGM) circulating along the OFRR circumference. D=80 μm; d=2 μm.

Due to the high Q-factor, a new laser emission band around 730 nm with a lasing threshold as low as 8 μJ/mm^2 was achieved for 0.1 mM Chla. The second laser emission band around 680 nm was realized with much higher excitation. In addition, competition between the lasing at the 680 nm and 730 nm band was observed. It is found that lasing at the 680 nm band can quench or significantly reduce the laser emission at 730 nm band, effectively increasing the lasing threshold

for the 730 nm band. Further concentration dependent studies, along with the detailed theoretical analysis, elucidated the mechanism that determines when and why the laser emission band appears at 680 nm or 730 nm, or concomitantly at both wavelengths. Finally, Chla was exploited as the donor in FRET to extend the optofluidic laser emission into the near infrared regime with an unprecedented wavelength shift as large as 380 nm, respectively and lasing threshold lower than 0.5 $\mu J/mm^2$.

Our work will open a door to the development of novel biocompatible and biodegradable chlorophyll based lasers for various applications such as on-chip tunable coherent light sources and *in-vitro*/*in-vivo* biosensing. It will also provide important insight into the energy transfer process inside plants and help resolve critical issues in plant biology.

2.2. Experimental setup

The experimental setup of the chlorophyll laser based on the OFRR is illustrated in Fig. 2.1(d). Here Chla was chosen as the gain medium due to its primary role in photosynthesis. Chlorophyll *a* was purchased from Sigma-Aldrich (Product #C5753). It is known that Chla is dissolved in organic solvents, such as ethanol and acetone, not in water [62,63]. Therefore in our experiments, we chose ethanol as the solvent. Both AF680 and AF700 dyes were purchased from Thermo-Fisher (Product #A37574 & Product #A-20110). Each dye (powder) was first dissolved in ethanol (99.9%, Sigma-Aldrich) to form a 10 mM solution, and then diluted with ethanol to lower concentrations. For FRET lasing experiments, the compound solutions were prepared by mixing 10 mM Chla with 10 mM AF680 solutions (and 10 mM AF700 solutions) to achieve the desired Chla-AF680 and Chla-AF680-AF700 concentrations.

In our experiments, Chla was dissolved in ethanol and flowed through the OFRR. The

whispering gallery modes (WGMs) circulate along the circumference of the OFRR circular cross section (Fig. 2.1(d), right). The evanescent field of the WGM in the OFRR core interacts with the gain medium (Chla) and provides the optical feedback for lasing[64]. Fabrication of the OFRR have been well documented elsewhere[64-66]. Briefly, a fused silica capillary preform (Polymicro Technologies TSP700850) was first etched with diluted hydrofluoric acid and then rapidly stretched under CO_2 laser irradiation. The resulting OFRR capillary was slightly bulged with a diameter of 80 μm at the center and of a few microns smaller at the two necking points approximately 1 mm apart. The wall thickness of the OFRR was approximately 2-4 μm and the Q-factor is approximately 10^7 [64,67]. A typical confocal optical setup was used to excite the sample and collect emission light from the OFRR (Fig. 2.1(d)). In this work, a pulsed OPO laser (pulse width: 5 ns, repetition rate: 20 Hz) was used as the excitation source and loosely focused through a cylindrical lens (20 mm focal length) to excite a 1-mm portion of the OFRR capillary. The pump intensity was adjusted by a continuously variable neutral density filter. The emission light was collected through the same lens and sent to a spectrometer (Horiba iHR550) for analysis.

2.3. Results and discussion

2.3.1. Lasing characteristics

Fig. 2.2(a) demonstrates the lasing emission spectra of Chla at a concentration of 0.1 mM under low pump energy densities. Initially, a number of periodic lasing peaks emerge around 730 nm. The multiple lasing peaks are the result of multi-mode nature of the WGMs. With the increased pump energy density, those lasing peaks grow accordingly, but remain within the same spectral range around 730. Fig. 2.2(b) plots the total laser emission in the 730 nm band as a function of the pump energy density, from which the lasing threshold is derived to be approximately 8.2 $\mu J/mm^2$.

Such a low lasing threshold at a low Chla concentration results from the extremely high Q-factor of the OFRR ($>10^7$)[64,67,68]. Lasing emission gradually levels off as the pump intensity is beyond 110 μJ/mm^2. During experiments, the Chla laser at the 730 nm band exhibits high photostability when the pump energy density is below 100 μJ/mm^2, suggesting practical use of the Chla laser. However, as the pump energy density reaches 250 μJ/mm^2, the lasing emission at the 730 nm band suddenly vanishes and meanwhile the lasing emission at shorter wavelengths starts to emerge around 680 nm. This extraordinary phenomenon can clearly be seen in Fig. 2.2(c) that plots the Chla lasing emission spectra under various high pump energy densities. Similar to the lasing profile at the 730 nm band, periodic lasing peaks grow but remain consistently within the same spectral range with the increased pump energy density. Interestingly, at very high pump energy densities, the lasing peaks at the 730 nm band start to re-emerge and compete with those at the 680 nm band. No other lasing emission bands are observed between the two competing bands. In order to better illustrate the competition between the two lasing bands, Fig. 2.2(d) shows the lasing profile recorded over a time interval of 15 seconds. Due to conservation of the Chla in the excited states, competition in emission between two laser bands can be clearly observed under a constant pump energy density. According to our experiments, the corresponding lasing threshold is approximately 230 μJ/mm^2 for the laser emission at the 680 nm band.

The above results reveal important characteristics of chlorophyll lasers. First, there exist two separate lasing bands at 680 nm and 730 nm in Chla lasers, which correspond to the (0,0) and (0,1) vibronic regions in the $S_1 \rightarrow S_0$ transition (Fig. 2.1). Second, lasing emission emerges at the 730 nm band first. With the increased pump energy density, lasing emission at the 680 band becomes dominant with concomitant significant reduction in lasing emission at the 730 nm band. Third, at very high pump energy densities, lasing emission at the 730 nm band re-emerges and

competes with that in the 680 nm band. The above phenomenon is in sharp contrast to the previous observation four decades ago[62]. In that study while the 680 nm lasing band was observed, stimulated emission at the 730 nm band was never achieved, even at high chlorophyll concentration (2 mM). Although not completely understood, the disappearance of the 730 nm band was attributed to the formation of non-fluorescent Chla dimers at high concentrations.

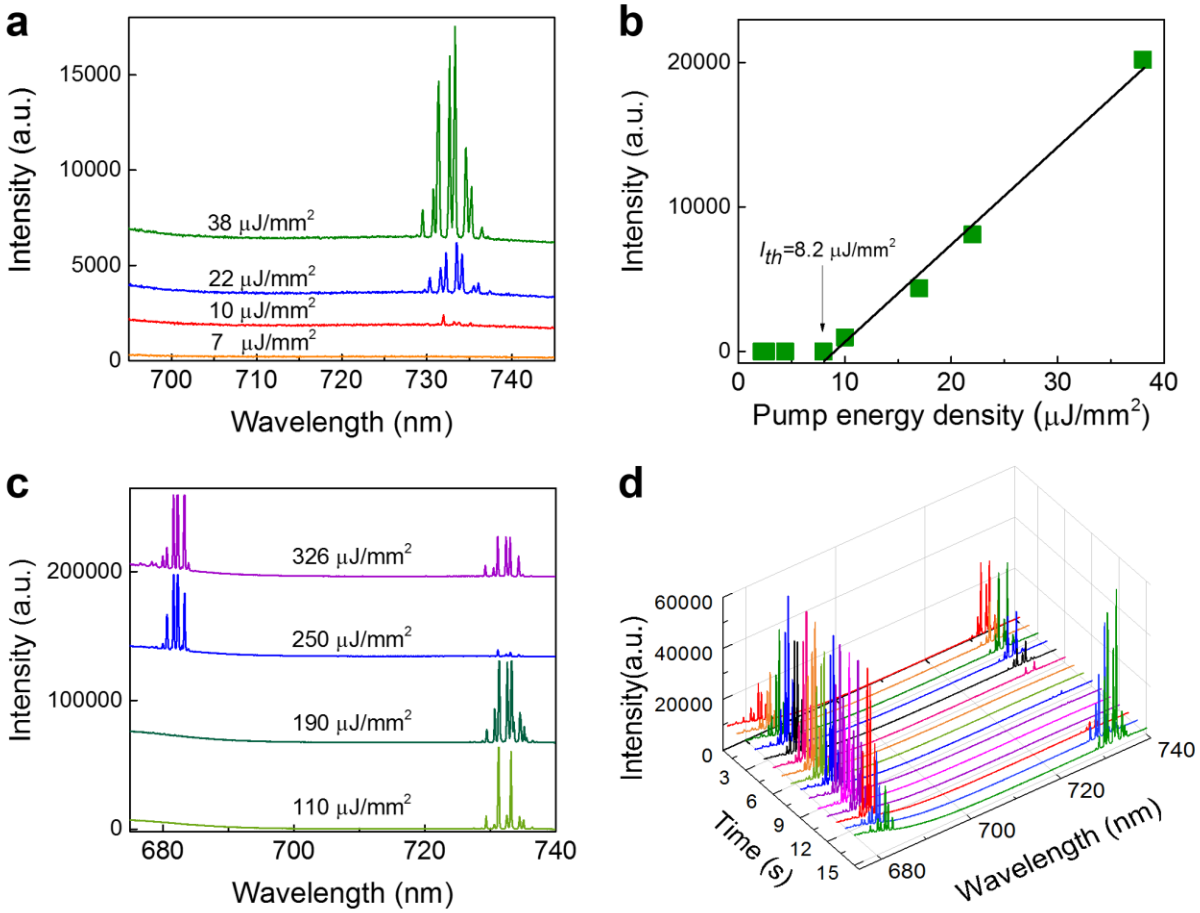

Figure 2.2. Chlorophyll lasing under low and high pump intensity. (**a**) Lasing spectra of 0.1 mM Chla in ethanol with relatively low pump energy densities. Curves are vertically shifted for clarity. (**b**) Spectrally integrated laser output as a function of pump energy density extracted from the spectra in (a). The solid line is the linear fit above the lasing threshold, showing a laser threshold of ~8.2 μJ/mm^2. Spectral integration takes place between 728 and 738 nm. (**c**) Lasing spectra of 0.1 mM Chla in ethanol with relatively high pump energy densities. Curves are vertically shifted for clarity. (**d**) Competition emission between two laser bands under a constant pump energy density of 326 μJ/mm^2. Different colors represent the measured lasing spectra at different timing (seconds).

2.3.2. Theoretical analysis

To resolve the contradictory experimental observations and to elucidate the underlying lasing mechanisms of Chla lasers, we carried out the following theoretical analysis. At the lasing threshold, we have [69]

$$n_1\sigma_e(\lambda_L) = (n_T - n_1)\sigma_a(\lambda_L) + \frac{2\pi m}{\lambda_L \eta Q_0}, \quad (1)$$

where n_T is the total concentration of Chla and n_1 is the concentration of the Chla in the excited state (S_1). $\sigma_e(\lambda_L)$ and $\sigma_a(\lambda_L)$ are the Chla emission and absorption cross sections at the lasing wavelength (λ_L), η is the fraction of the light in the evanescent field of the OFRR, Q_0 is the OFRR empty-cavity Q-factor, and m is the effective refractive index of the WGM (m~1.4 for the OFRR). Rewriting Eq. (1) we obtain the fractional Chla at the excited state, γ_{th}:

$$\gamma_{th} = \frac{n_1}{n_T} = \frac{1}{\sigma_e(\lambda_L) + \sigma_a(\lambda_L)}[\sigma_a(\lambda_L) + \frac{2\pi m}{n_T \lambda_L \eta Q_0}]. \quad (2)$$

Figures 2.3(a) and (b) plot γ_{th} values for various representative concentrations of Chla based on Eq. (2), in which the absorption and emission cross sections were measured (Fig. 2.3 (c)), under the assumption of a high Q-factor ($\eta Q_0 = 1 \times 10^6$)[67]. At relatively high Chla concentrations (Fig. 2.3(a)), two γ_{th} minima around 680 nm and 730 nm are found, but γ_{th} at the 730 nm band is much lower than that at the 680 nm band, indicating that the laser emission emerges around 730 nm first. Below we use the 0.1 mM Chla in Fig. 2.3(a) as an example to elucidate the Chla lasing mechanism. When the excitation is low (Curve 1), no laser emission can be observed. With the increased excitation (Curve 2), the 730 nm band is the first to reach the lasing threshold, and consequently, lasing emission emerges at this band. When the excitation continues to increase (Curve 3), the 680 nm band reaches the lasing threshold and starts to lase. Since the number of the excited states is

fixed at a given pump energy density, lasing action at the 680 nm band results in quenching or significant reduction in lasing emission at the 730 nm, effectively increasing the lasing threshold for the 730 nm band. Finally, at very high pump energy density, the laser emission at the 680 nm band continues to grow and meanwhile the 730 band laser emission re-emerges and competes with the 680 nm band. The above simulation agrees well with the experimental observations in Fig. 2.2(a) and Fig. 2.2(c). It is interesting to note that laser emission at the 680 nm band can easily overtake that at 730 nm, despite the fact that γ_{th} is lower at 730 nm than at 680 nm. This unconventional phenomenon is due to the fact that the (0,1) vibronic band at 680 nm in Chla, which is populated first before further relaxation down to the (0,0) vibronic band at 730 nm. Once the lasing threshold at the 680 nm band is reached, very rapid population depletion occurs due to stimulated emission between S_1 and S_0, thus making it much more difficult for the 730 nm band to achieve population inversion.

To further understand the lasing mechanism in Chla, in Fig. 2.3(b) we plot γ_{th} for two very low Chla concentrations. Both curves show two minima at 680 nm and 730 nm, respectively. In contrast to Fig. 2.3(a), γ_{th} is lower at the 680 nm than at the 730 nm, indicating that the laser emission should occur around 680 nm first and play a dominant role in overall lasing action. At low excitation (Curve 4), no lasing emission is expected for either 0.03 mM or 0.01 mM Chla. With the increased excitation, 0.03 mM Chla should start to lase at the 680 nm band. When the excitation continues to increase (Curve 5), laser emission should be observed at both the 680 nm and 730 nm band for 0.03 mM Chla, whereas only laser emission at the 680 nm band can be observed for 0.01 mM Chla. Finally, at very high excitation (Curve 6), laser emission from 0.03 mM Chla continues to increase at both the 680 nm and 730 nm band, whereas only laser emission at the 680 nm band can be observed for 0.01 mM Chla.

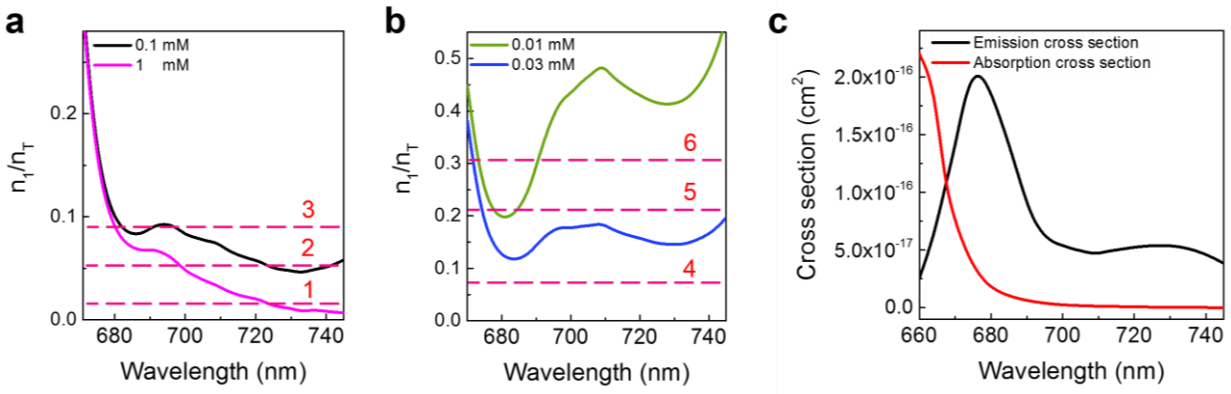

Figure 2.3. Theoretical analysis of chlorophyll laser condition. (**a**) and (**b**) Fraction of Chla molecules in the excited states needed at the laser threshold for various representative Chla concentrations based on Eq. (2) with η=0.1 and $Q_0=10^7$. Curves 1-6 corresponds to various excitation levels of Chla molecules. Curve 1: At a very low pump energy density, the Chla excitation is quite low. No laser emission is expected to emerge for 0.1 mM Chla. Curve 2: At an intermediate pump energy density, the lasing emission at the 730 nm band emerges for 0.1 mM Chla. Curve 3: At a relatively high pump energy density, both 680 nm and 730 nm bands emerge and compete with each other. Curve 4: At a low pump energy density, the Chla excitation is low. No laser emission is expected to emerge for either 0.03 mM or 0.01 mM Chla. Curve 5: At an intermediate pump energy density, two lasing bands are expected to appear around 680 nm and 730 nm for 0.03 mM Chla, and only one lasing band is expected to appear at 680 nm. Curve 6: With further increased pump energy density, the lasing emission increases in comparison with the case for Curve 5, but no laser emission is expected to appear at the 730 nm band for 0.01 mM Chla due to the requirement for extremely high Chla excitation. (**c**) Absorption cross sections (black curve) and emission cross sections (red curve) of Chla in ethanol from 660 nm to 745 nm.

To validate the above theoretical analysis and simulation results at low Chla concentrations, the measured lasing spectra of 0.01 mM and 0.03 mM Chla under different pump energy densities are exemplified in Fig. 2.4(a) and (b), respectively. We chose three pump energy densities (65 $\mu J/mm^2$, 250 $\mu J/mm^2$, and 580 $\mu J/mm^2$) to represent the low, intermediate, and high Chla excitation described by Curves 4-6 in Fig. 2.3(b). Note that Curves 4-6 plotted in Fig. 2.3(b) are only representatives of different excitation levels and not equivalent to the exact excitation shown in Fig. 2.4. Initially, no lasing emission is observed for either 0.01 mM or 0.03 mM Chla, as shown by 65 $\mu J/mm^2$ in Fig. 2.4(a) and (b). When the pump energy density reaches 250 $\mu J/mm^2$, two lasing bands emerge for 0.03 mM Chla; however, only one lasing band around 680 nm appears for

0.01 mM Chla. At 580 $\mu J/mm^2$, laser emission around 680 nm and 730 nm continues to grow for 0.03 mM Chla. In contrast, for 0.01 mM Chla despite intensity increase in the 680 nm band, no laser emission is observed at 730 nm, as it requires much higher pump energy density. The experimental observation in Fig. 2.4 matches perfectly the phenomena described in Fig. 2.3(b).

Based on the above theoretical analysis and experimental observation, it becomes clear that there exist two lasing band around 680 nm and 730 nm for Chla. Depending on the Q-factor and the Chla concentration, either 680 nm or 730 nm band can start to lase first. In addition, there exists competition between the lasing at the 680 nm band and 730 nm band. Lasing at the 680 nm band can quench or significantly reduce the laser emission at 730 nm band, effectively raising the lasing threshold for the 730 nm band. The reason that the 680 nm overtakes the 730 nm is due to the fact that the 680 nm is populated first during the energy transfer process in chlorophylls upon photo-excitation. Capability to control which band to lase first and observation of the competition between the two bands will have significant impact on optofluidic laser development and provide vital information to better understand the energy transfer mechanism in Chla.

Previous work showed lasing emission around 680 nm, but failed to achieve lasing emission at the 730 nm band. This was actually due to the low Q-factor cavity (1-cm long cuvette) and the competition between the 680 nm and the 730 nm band. Fig. 2.5 plots γ_{th} for the Chla concentration ranging from 0.1 mM to 2 mM with a low Q-factor. It can be seen easily at the 680 nm band dominates for all concentrations of interest, in particular, at relatively low concentrations (0.1 mM – 0.5 mM). At a high concentration of 2 mM, γ_{th} at the 730 nm is close to that at the 680 nm band and lasing at 730 nm is seemingly possible. However, due to the competition of the 680 nm band lasing, the lasing threshold for the 730 nm band is actually much higher than theoretically predicted in all concentrations. Furthermore, the penetration depth was only about 200 μm at the

excitation wavelength of 337.1 nm for 2 mM Chla[62], which made the 730 nm lasing emission even more difficult to realize for Chla solution in a 1-cm long cuvette. Previous studies attributed the disappearance of the 730 nm band lasing to the formation of non-fluorescent Chla dimers at 2 mM, which we believe does not reflect the actual underlying mechanism. As a control experiment, lasing at the 730 nm band from 5 mM Chla can easily be achieved in Fig. 2.6 with relatively low pump energy density using our high Q-factor OFRR.

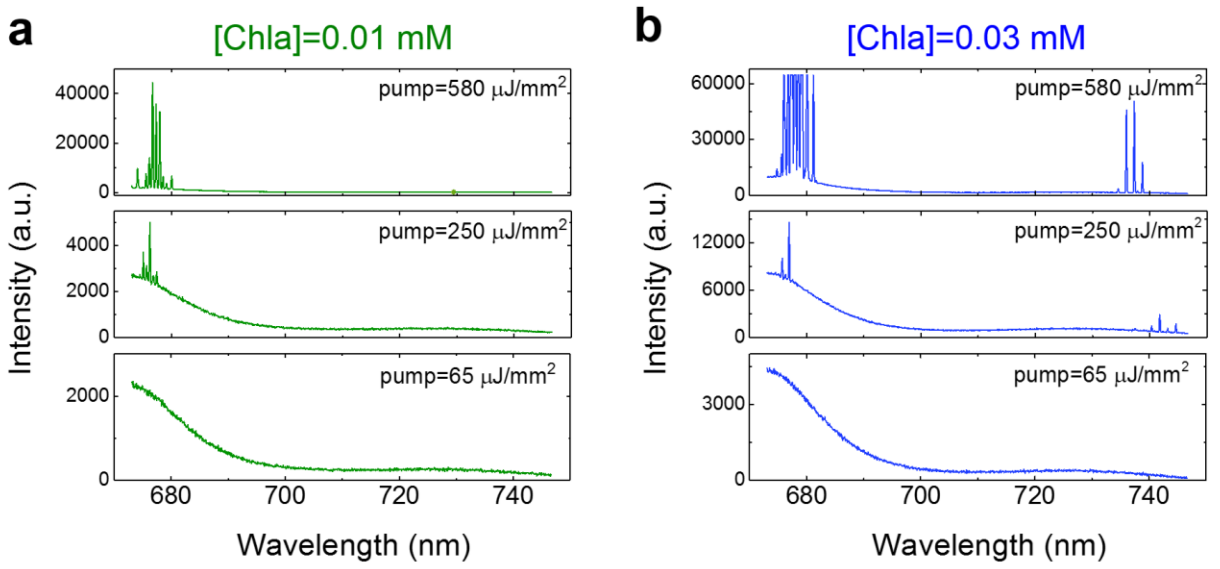

Figure 2.4. Lasing under different concentration and pump energy density. Lasing spectra for 0.01 mM (**a**) and 0.03 mM (**b**) Chla under the pump energy density of 65 μJ/mm^2, 250 μJ/mm^2, and 580 μJ/mm^2. The chosen three pump energy densities correspond to the low, intermediate, and high Chla excitation described by Curves 4-6 in Fig. 3.

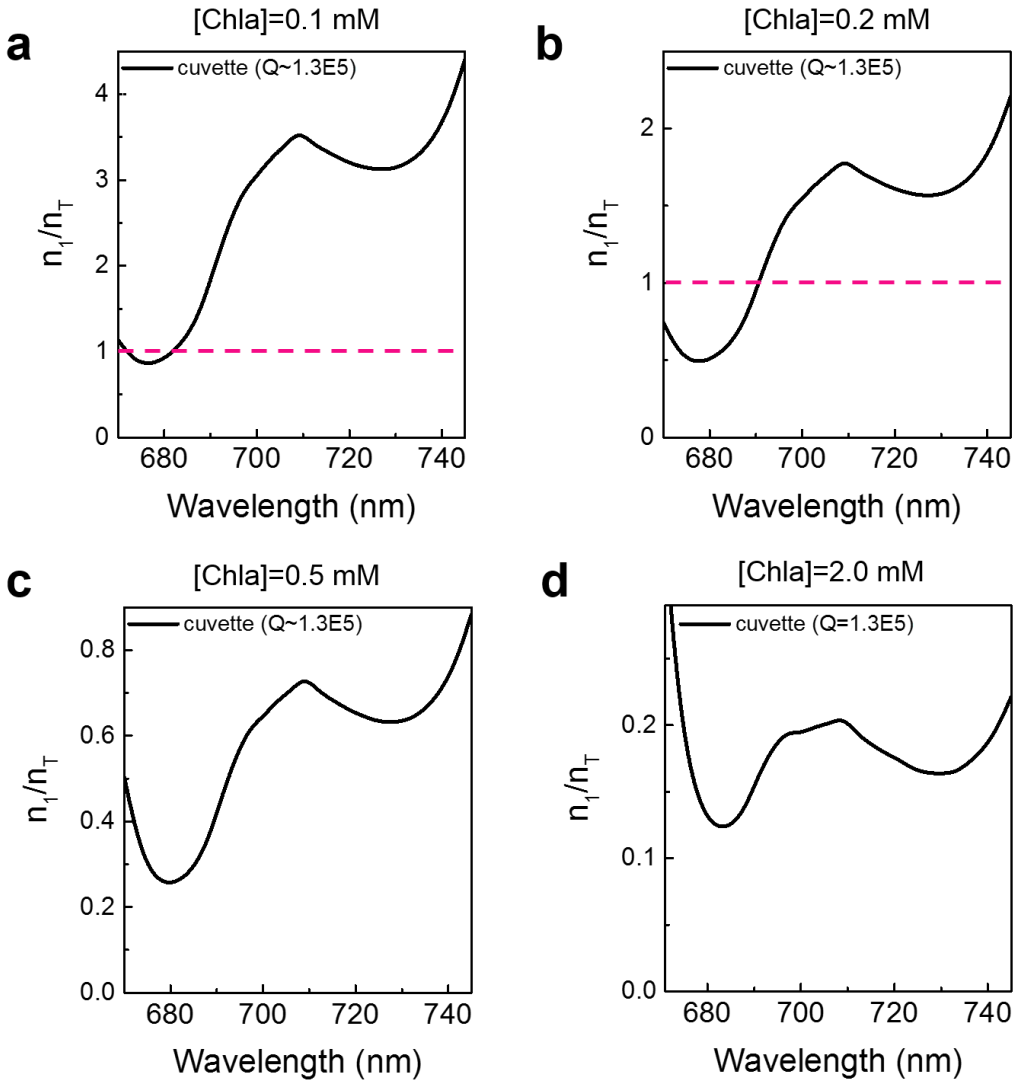

Figure 2.5. Theoretical analysis of chlorophyll lasing under low-Q factor cavity. Fraction of Chla molecules in the excited states needed at the threshold for (a) 0.1 mM, (b) 0.2 mM, (c) 0.5 mM, and (d) 2.0 mM of Chla based on Eq. (2) in the main text with η=1.0 and Q_0=1.3x10^5, which corresponds to the situation where a low Q-factor 1-cm long cuvette is used as the laser cavity. In all concentrations, the minimum occurs around 680 nm, suggesting that the lasing band at 680 nm is dominant. Lasing at the 730 nm band either is non-physical (*i.e.*, n_1/n_T>1) or requires much higher excitation.

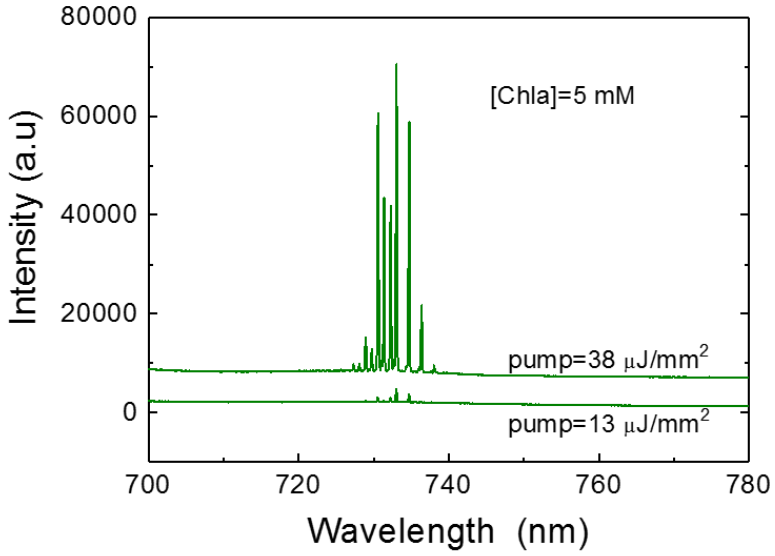

Figure 2.6. Chlorophyll lasing at 5mM. Lasing at the 730 nm band can be achieved even with the Chla concentration as high as 5 mM in ethanol. Curves are vertically shifted for clarity.

2.3.3. Chlorophyll FRET lasing

In order to further explore the unique properties of chlorophylls such as high absorption at blue and UV spectrum and large Stokes shift, we developed and studied an optofluidic chlorophyll FRET laser using chlorophyll and dye molecules as the donor and acceptor, respectively. In our experiments, Chla and Alexa Fluor 680 dye (AF680) were chosen to be the FRET pair (see Fig. 2.7 for spectral overlap between Chla and AF680). As a control experiment, Fig. 2.8 shows that AF680 alone has a lasing threshold of 31 μJ/mm^2. In comparison, Curve 1 in Fig. 2.9(a) shows the FRET (Chla+AF680) lasing emission around 780 nm under a very low pump energy density of 1.1 μJ/mm^2 at 430 nm. Meanwhile, only featureless emission spectra are observed for Chla and AF680, as exemplified in the Curve 2 and Curve 3, respectively. Therefore, the lasing emission at 780 nm at 1.1 μJ/mm^2 is from AF680 under FRET excitation, which extends the lasing emission to the NIR. We further investigated the FRET laser emission spectra at different pump energy

densities, as shown in Fig. 2.9(b). A significant blue-shift of the FRET lasing peaks is observed as the pump intensity increases, which is typical for dye lasers[67]. Note that at 38 μJ/mm^2, the AF680 alone can lase through direct excitation at 430 nm (see Fig. 2.8). However, such laser emission (around 780 nm) can be easily distinguished from that via FRET (around 750 nm in Fig. 2.9). The spectrally integrated FRET emission versus pump energy density for Chla-AF680 is plotted in Fig. 2.9(c), in which the lasing threshold is derived to be as low as 0.7 μJ/mm^2 from the inset, which is 40 times lower than that of AF680 alone.

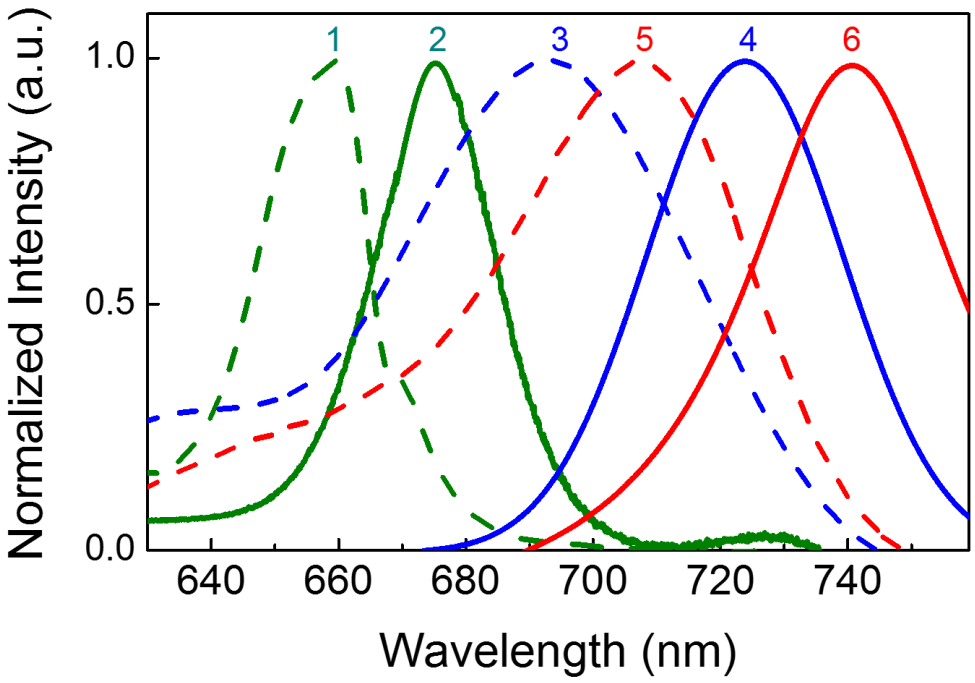

Figure 2.7. Absorption and emission spectra for FRET. (a) Normalized absorption (dashed line) and emission (solid line) spectrum of Chla (Curves 1 and 2), AF680 (Curves 3 and 4), and AF700 (Curves 5 and 6) in ethanol.

In order to extend the laser emission further into the NIR, a third dye (Alexa Fluor 700 - AF700) was used in conjunction with Chla and AF680 (see Fig. 2.7 for the spectral overlap among Chla, AF680, and AF700) to form a cascade FRET laser, in which the pump energy is first

absorbed by Chla, subsequently transferred to AF680, and finally to AF700. Curve 1 in Fig. 2.9(d) shows the cascade FRET laser emission from AF700 at a pump energy density of 0.8 μJ/mm^2. Multiple lasing peaks around 810 nm, which represent a spectral shift over 380 nm, are obtained. Further pump energy density dependent experiment in Fig. 2.10(a) shows that the lasing threshold is approximately 0.5 μJ/mm^2. To confirm the laser emission was indeed from AF700 via cascade FRET, two control experiments were carried out. Curve 2 in Fig. 2.9(d) shows no laser emission from AF700 in the absence of AF680 due to insufficient energy transfer between Chla and AF700 caused by small spectral overlap. Curve 3 further shows that no laser emission from AF700 alone at 0.8 μJ/mm^2, since its lasing threshold is 1.8 μJ/mm^2 (Fig. 2.10(b)), 3.6 times higher than that obtained in Curve 1. Finally, to demonstrate the versatility of the cascade FRET laser, in Fig. 2.11 we replaced AF700 with DyLight 700 (Dyl700) and achieved laser emission around 810 nm.

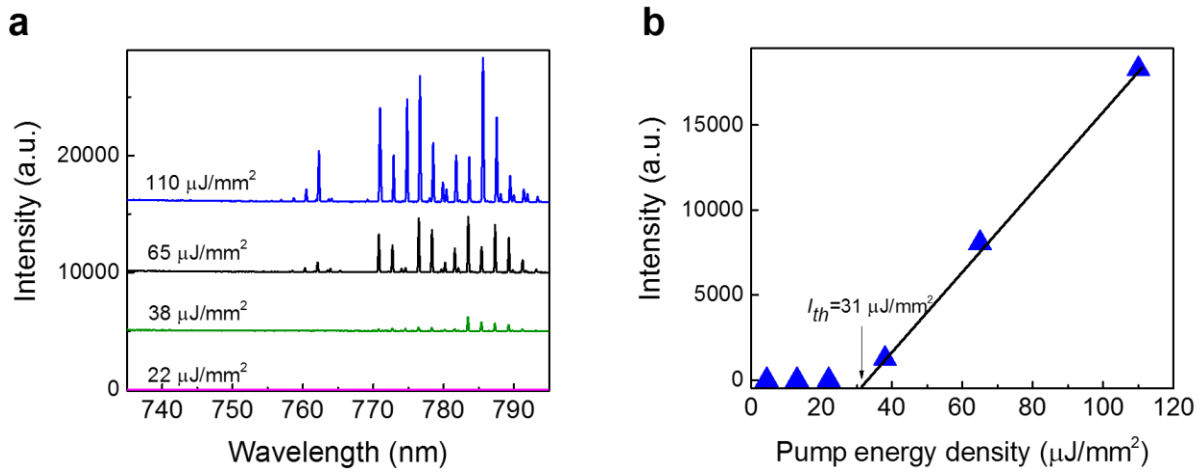

Figure 2.8. Direct lasing of AF680. (a) Lasing spectra of AF680 (5 mM) alone in ethanol under various pump energy densities. Excitation wavelength=430 nm. (b) Spectrally integrated (745 nm – 790 nm) laser output as a function of pump energy density extracted from (a). Solid line is the linear fit above the threshold, showing a lasing threshold of approximately 31 μJ/mm^2.

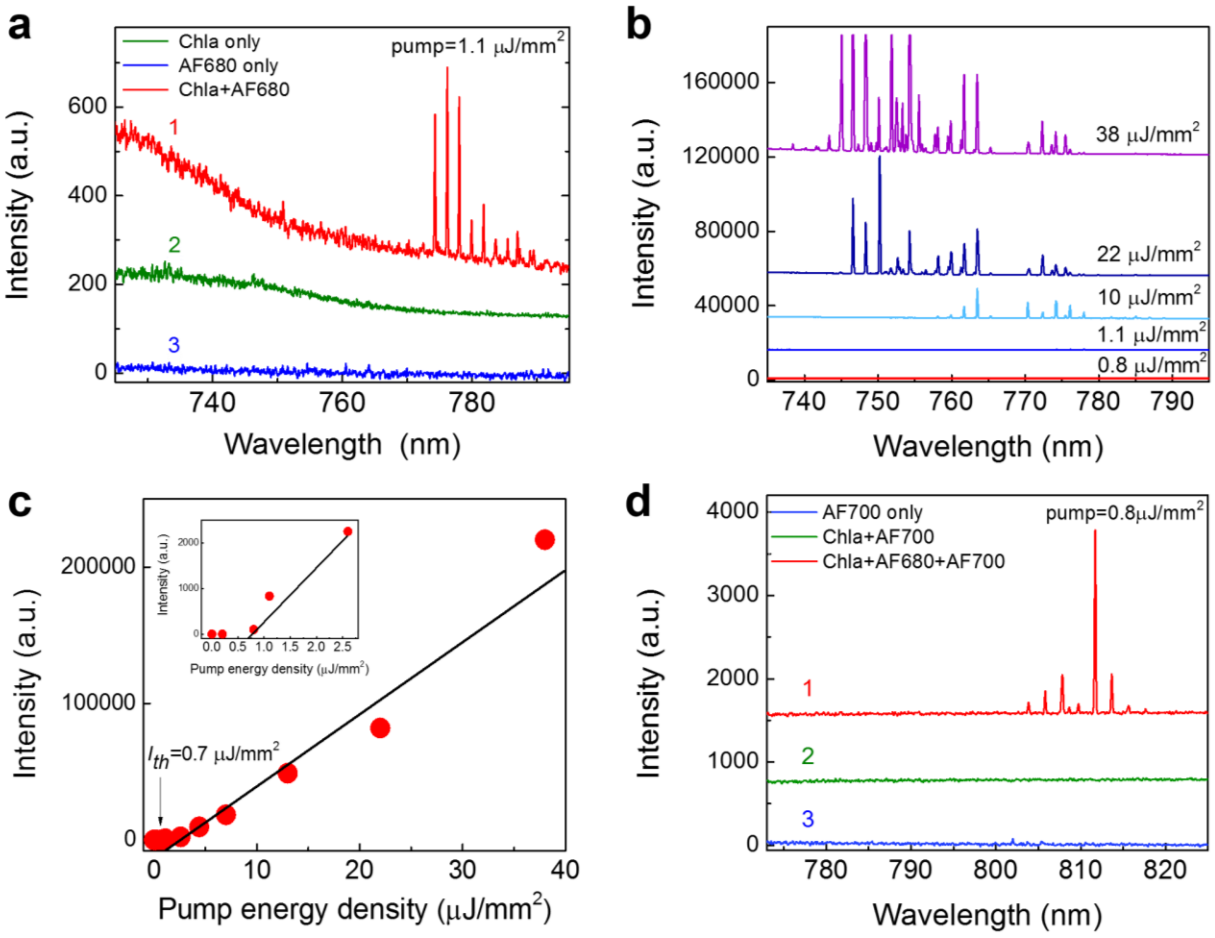

Figure 2.9. Two-level and three-level chlorophyll FRET lasing. (**a**) Comparison of the lasing spectra of mixture of Chla-AF680 in ethanol (Curve 1), Chla alone in ethanol (Curve 2), and Alexa Fluor 680 (AF680) alone in ethanol (Curve 3) under the same pump energy density of 1.1 μJ/mm^2. (**b**) Lasing spectra of AF680 in ethanol via energy transfer from Chla under various pump energy densities. In (a) and (b), [Chla]=5 mM and [AF680]=5 mM for all curves. Excitation wavelength=430 nm. (**c**) Spectrally integrated (745 nm – 790 nm) FRET laser output as a function of pump energy density extracted from (b). The inset presents the enlarged portion for the pump energy density below 3.0 μJ/mm^2. Solid lines are the linear fit, showing a lasing threshold of approximately 0.7 μJ/mm^2. (**d**) Emission spectra of mixture of Chla-AF680-AF700 (1), mixture of Chla-AF700 (2), and Alexa Fluor (AF700) dye alone (3) under the same pump energy density of 0.8 μJ/mm^2. [Chla]=5 mM, [AF680]=5 mM, and [AF700]=5 mM for all curves. Curves are shifted for clarity.

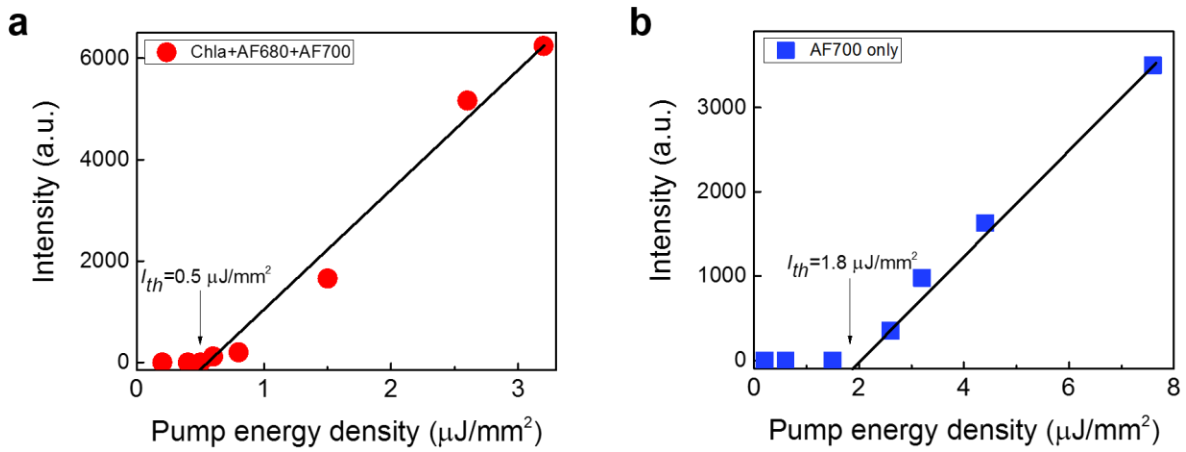

Figure 2.10. Lasing threshold of three-level FRET and pure AF700. Spectrally integrated (800 nm – 825 nm) laser output as a function of pump energy density of **(a)** cascade FRET laser emissions (CHla+AF680+AF700) and **(b)** AF700 laser emissions. Solid line is the linear fit above the threshold, showing a lasing threshold of approximately 0.5 μJ/mm² and 1.8 μJ/mm², respectively. [Chla]=5 mM, [AF680]=5 mM, and [AF700]=5 mM for all experiments. Excitation wavelength=430 nm.

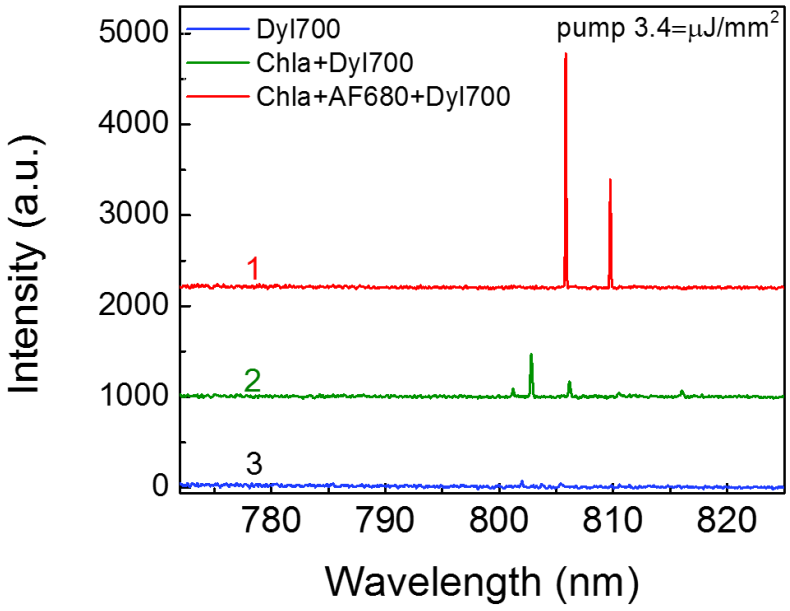

Figure 2.11. Lasing spectra of Chla-AF680-Dyl700 FRET. Emission spectra of mixture of Chla-AF680-Dyl700 in ethanol (Curve 1), mixture of Chla-Dyl700 in ethanol (Curve 2), and Dyl700 alone in ethanol (Curve 3) under the same pump energy density of 3.4 μJ/mm². [Dyl700]=5 mM, [AF680]=5 mM, and [Chla]=5 mM for all curves. Excitation wavelength=430 nm. Dyl700: DyLight 700-B1.

2.4 Conclusion

We have investigated the chlorophyll based optofluidic laser, in which two competing lasing bands at the 680 nm and 730 nm were observed for the first time. The lasing threshold for the 730 nm as low as 8 $\mu J/mm^2$ was achieved for 0.1 mM Chla. Furthermore, we found that the lasing emission at the 680 nm band results in the quenching or significant reduction in the lasing emission at the 730 nm, effectively increasing its lasing threshold. The theoretical analysis and experimental measurement revealed the detailed mechanism that determines when and why the laser emission band appears at 680 nm or 730 nm, or concomitantly at both wavelengths. In addition, using Chla as the donor, we have achieved FRET laser at the NIR with a wavelength shift as large as 380 nm.

We envision that our work lead to the development of novel biocompatible optofluidic devices and optofluidic FRET lasers with low lasing thresholds and large wavelength shifts. The ability to control the laser emission band will enable us to engineer and optimize optofluidic lasers for various applications. Our work may offer scientists to resolve critical issues in plant biology, such as the role of stimulated emission in chlorophyll fluorescence and photosynthesis.

Chapter 3

Lasing in Human Whole Blood

In this chapter, we first demonstrate optofluidic lasers in tissues by using liquid biopsy, including human serum and whole blood. Here we utilized Indocyanine green (ICG) as the gain material for lasing in tissues. ICG is the only near-infrared dye approved by the U.S. Food and Drug Administration for clinical diagnosis of cancer. Here we successfully demonstrated the first ICG lasing in human serum and whole blood with the clinical ICG concentrations and the pump intensity far below the clinically permissible level. Furthermore, we systematically studied ICG laser emission within each major serological components and revealed the critical conditions for lasing. Detailed blood components that are investigated in this chapter are plotted in Fig. 3.1(a).

3.1. Introduction

ICG is the *only* near-infrared dye approved by the U.S. FDA for clinical use [70,71], such as hepatobiliary surgery [72], sentinel lymph node biopsy [73], and assessment of surgical tumor resection margins [70,74]. ICG has low toxicity and exhibits absorption and emission maxima around 730 nm and 800 nm (Fig. 3.1(b)) - both wavelengths are within the ideal spectral window of human tissues for clinical imaging. When injected in blood, ICG binds primarily to plasma proteins and lipoproteins, resulting in enhanced fluorescence [70,75-78] (as shown in Fig. 3.1(c)). In practice, ICG is injected in the blood circulation within the normal clinical dosage range to locate the tumor site and its margin by the higher fluorescence above the background since more blood vessels are grown within/around the tumor site [79,80]. In addition, ICG has been extensively used in *in-vitro*

preclinical studies of cell lines or animal tissues[77,80-82] with an aim to develop innovative technologies and methodologies for potential clinical applications. In cancer surgery, one of the main prognostic factors for survival rate is complete tumor resection and imaging modalities that allow the specific differentiation and identification of vital structures, would be of huge benefit during image guided surgery. However, in clinical applications, due to background fluorescence and omnipresent tissue scattering, it remains challenging to obtain high contrast in ICG emission between the tumor and normal tissue for precise tumor detection and margins of excision[81,83-85]. In *in-vitro* applications, ICG emission is often not sensitive enough to detect or monitor subtle changes in concentrations or structures in biomolecules, cells, and tissues. Therefore, ICG emission with a superior signal-to-background ratio (SBR) is highly desirable.

As discussed in chapter 1, laser emission has distinct advantages over fluorescence, particularly at the molecular [6,9,23,27,52,86,87] and cellular level [6,20,35,36]. First, it is significantly more sensitive to biomolecular and cellular changes than fluorescence [6,23,86-88], thanks to the optical feedback in lasing. Second, the laser signal is orders of magnitude stronger and has much narrower linewidth (so that the broad-band background can be spectrally filtered out). Finally, due to the threshold behavior in lasing emission, a large contrast (10^2-10^3 fold) can be obtained between before and after lasing [27,89]. All of those result in unprecedented SBR in imaging for tumor localization and sensitivity in in-vitro biosensing. Therefore, using ICG laser emission could lead to a paradigm change in clinical practice and theranostics. However, while a plethora of previous work have shown the great promise of optofluidic lasers in in-vitro biomolecular and cellular analysis [6,18,23,27,35,36,87-89], no research has been conducted on feasibility of laser emission from an FDA approved dye in whole human blood (which is tissue), particularly at the clinically acceptable dye concentration and external pump intensity.

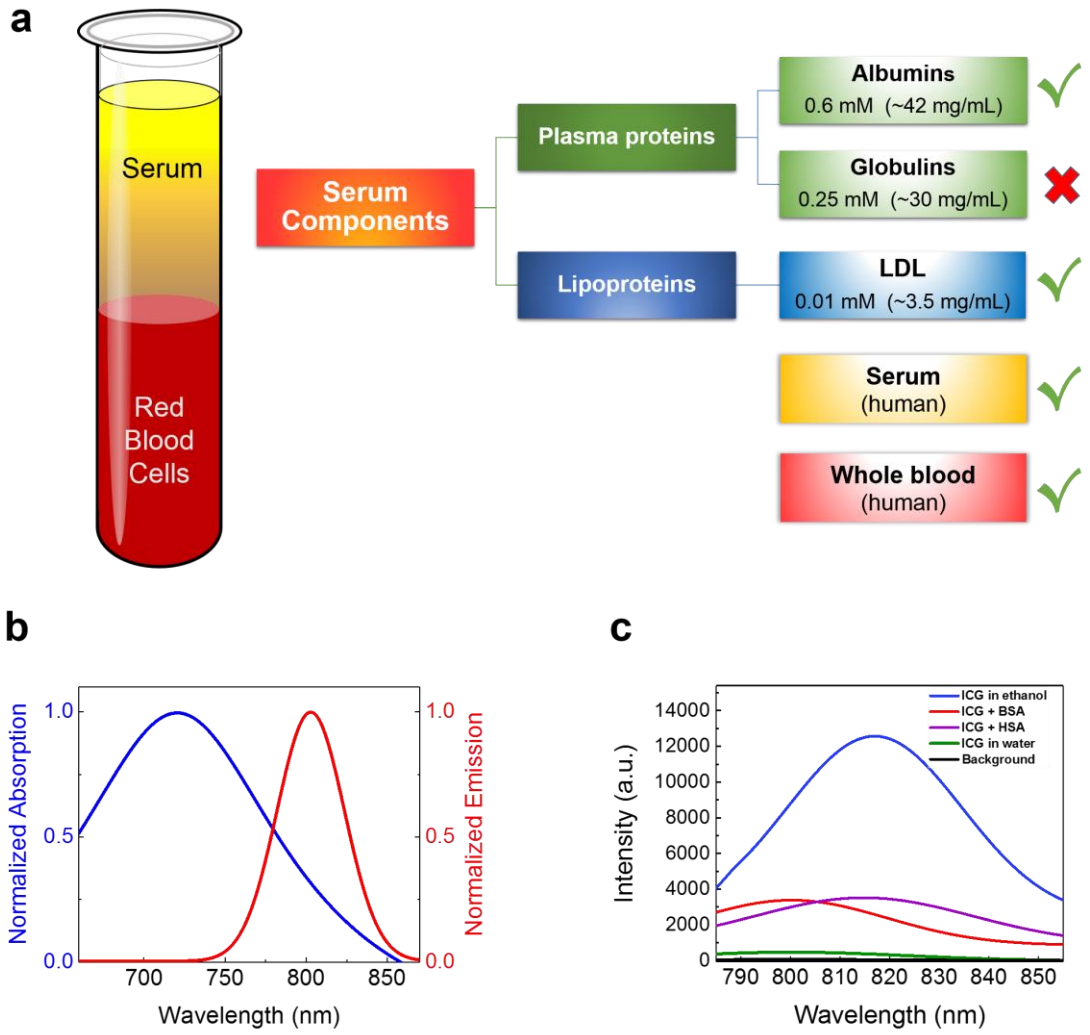

Figure 3.1. Concept of whole blood and ICG emission properties. (a) Schematic diagram showing the composition of blood. The diagram on the rightmost column lists the serological components along with their respective typical concentrations in serum, which we have investigated in the current work. Green checks denote that lasing was achieved with those components when Indocyanine Green (ICG) within the clinically acceptable concentration range was added, whereas the red cross denotes the component that no lasing was observed from ICG. **(b)** Normalized absorption spectrum (blue curve) and emission spectrum (red curve) of purified ICG in DI water from 660 nm to 880 nm. **(c).** Emission spectra of ICG in water (green curve), ICG in ethanol (blue curve), ICG with BSA (0.6 mM) in PBS (red curve), ICG with HSA (0.6 mM) in PBS (purple curve), and background signal (black curve) under the same pump energy density. Excitation wavelength=660 nm. The ICG concentration was fixed at 0.2 mM for all measurements. To estimate the quantum yield (QY), we used the well-known QY of ICG in ethanol (13.2%) as the reference. The measured QY is 0.48% for ICG alone in water, 4.1 % for ICG-HSA, and 3.9 % for ICG-BSA.

In this chapter, we carried out for the first time systematic investigation on ICG lasing. We started with each of major serological components (albumins, globulins, and lipoproteins) to elucidate the critical elements and conditions responsible for ICG lasing. Then, we demonstrated ICG lasing in human serum. Finally, we studied ICG lasing in human whole blood. All the ICG concentrations in serological component studies were well below the commonly used level in in-vitro biological studies (~1 mM) [90-92] with the lasing threshold on the order of 1 $\mu J/mm^2$. More significantly, lasing could be achieved in human serum and whole blood using ICG within the normal range of clinical dosage (0.01 mM – 0.07 mM in human blood [93,94]). The threshold of laser emission in whole blood was 10 $\mu J/mm^2$, 20 times lower than the laser exposure limit for tissues (~200 $\mu J/mm^2$) [95]. In the end of the Chapter, we will present a few possible clinical, preclinical, and biomedical opportunities where the ICG laser may help improve the existing practices and also discuss the challenges that it faces, in particular, for *in-vivo* clinical applications where the current high-Q cavities may not be applicable.

3.2. Experimental design

Throughout the experiments, we used the optofluidic ring resonator (OFRR) based on a thin-walled fused silica capillary, as illustrated in Fig. 3.2(a). The circular cross section of the capillary forms the ring resonator that that supports the high-Q ($>10^7$) whispering gallery modes (WGMs). The liquid was injected into the OFRR, in which the evanescent field of the WGM present inside the capillary interacts with gain medium in the liquid and provides the optical feedback for lasing.

The ICG used in this work was purchased from Sigma-Aldrich (Product #C5753). Other components including HSA (P8119), LDL (L8292), γ-globulins (G4386) and human serum (H4522) were all purchased from Sigma-Aldrich. BSA and PBS were purchased from R&D

systems (Product#841380, #896009). Human whole blood was purchased from *ZenBio* Inc. (Product# SER-WB10ML), which were collected from healthy volunteers (1 male and 1 female) through Interstate Blood Bank, USA. First, ICG powder was dissolved in DI water to form 2 mM solution, and then diluted with DI water to lower concentrations (1 mM and 0.2 mM). LDL, BSA, HSA and human serum were originally ordered in solution form, whereas γ-globulins powder was prepared by dissolving it in 0.9% saline. The measured concentration of LDL, BSA and HSA in this work were diluted by mixing with 2 mM, 1 mM, or 0.2 mM ICG solutions to obtain the desired compound solutions. For the serum experiments, 200 μL of pure serum was mixed with 50 μL of ICG (1 mM, 0.2 mM) to obtain ICG (0.2 mM, 0.04 mM) compound solutions, respectively. Regarding the whole blood experiments, fresh human blood was first diluted two times with PBS, then added with 0.2 mM ICG to form 0.04 mM compound solution. Other concentrations of ICG used in experiments were prepared similarly. All the prepared samples were allowed to stand for 20 minutes under room temperature before measuring to ensure the completion of binding reactions of ICG.

The fabrication of the OFRR have been well documented elsewhere [64]. The resulting OFRR capillary was slightly bulged with a diameter of 80 μm at the center and of a few microns smaller at the two necking points approximately 1 mm apart. The wall thickness of the OFRR was approximately4 μm and the Q-factor is approximately 10^7 [64,67].

Similar to Chapter 2, a typical confocal setup was used to excite the sample and collect emission light from the OFRR (Fig. 3.2(c)). A pulsed OPO laser (pulse width: 5 ns, repetition rate: 20 Hz) with 660 nm was used as the excitation source to excite a 1-mm portion of the OFRR capillary. Detailed setup is illustrated in Fig. 3.2(c).

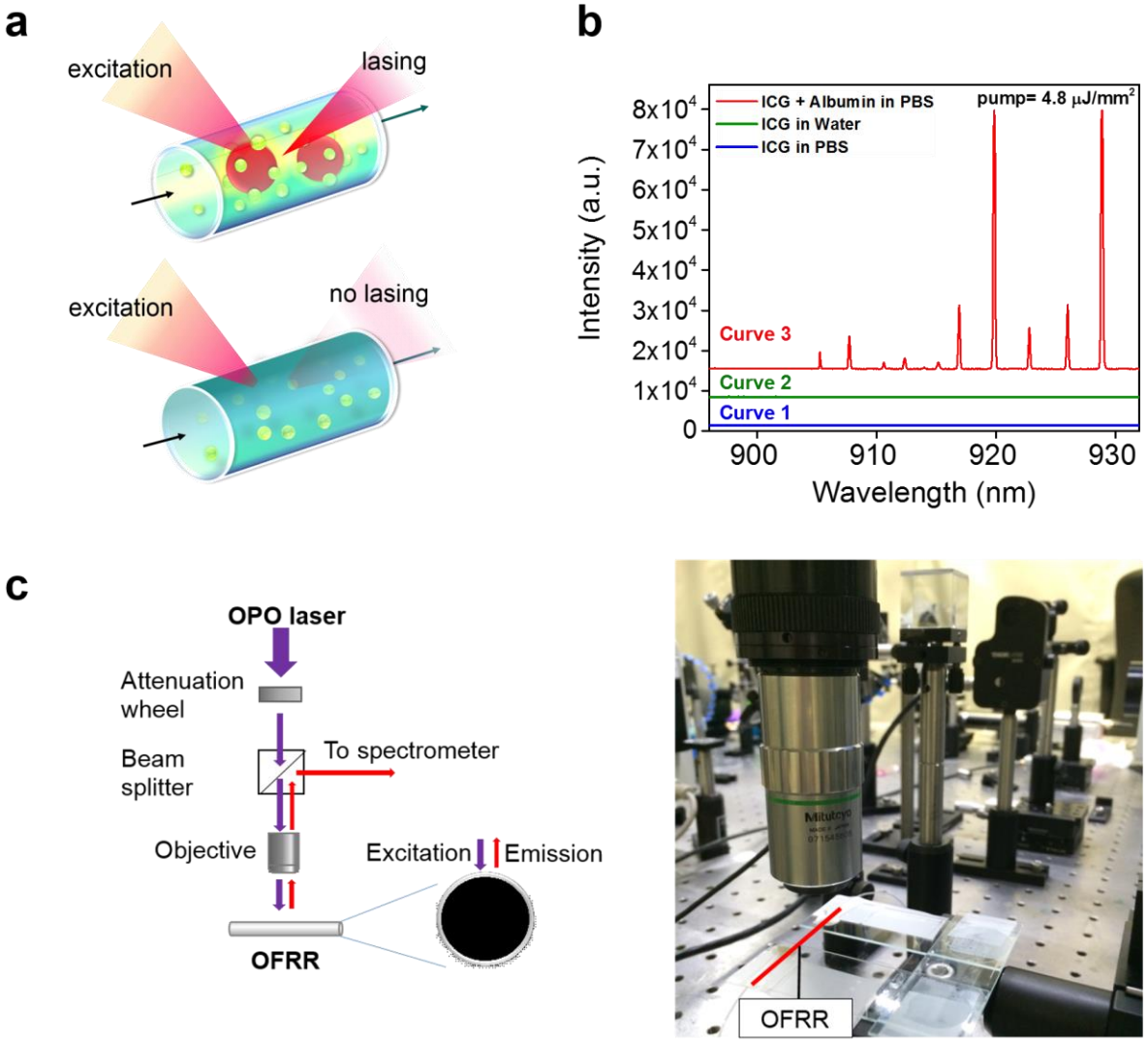

Figure 3.2. Experimental setup and ICG lasing. (a) Schematic of the ICG laser using a high Q-factor optofluidic ring resonator (OFRR). It also illustrates that the ICG lasing can only be achieved when ICG binds to serological components such as albumin and lipoprotein. The green circles denote ICG molecules, whereas the red circles denote serological components. During the experiment, ICG was excited by a pulsed optical parametric oscillator (OPO) (pulse width=5 ns; wavelength=660 nm). **(b),** Comparison among various emission spectra of ICG. Curve 1: ICG alone in PBS. Curve 2: ICG alone in DI water. Curve 3: ICG with albumin (BSA) in PBS. All curves were obtained under the same pump energy density of 4.8 μJ/mm^2 with the same ICG concentration of 0.4 mM. Curves are vertically shifted for clarity. **(c)** Illustration of the experimental setup. The right photo shows the experimental setup. The red line indicates the position of the OFRR, as the actual OFRR is too thin to be visible.

3.3. Results and discussion

3.3.1. Indocyanine green (ICG) lasing

First, as a control experiment, Curves 1 and 2 in Fig. 3.2(b) show no laser emission from ICG (0.4 mM) alone in either phosphate buffered saline (PBS) or deionized (DI) water at the excitation of 4.8 μJ/mm^2. In fact, no laser emission was observed even when the excitation was as high as 25 μJ/mm^2. This is due to the extremely low quantum yield (0.48%) of ICG in PBS or water. In contrast, in the presence of proteins rapid binding to ICG results in a significant increase in quantum yield (~4.0 %, Fig. 3.1). Although such a quantum yield is still quite low in comparison with that for many other dyes (such as Rhodamine 6G, Cy3 and Cy5, *etc*.), it is sufficient to support laser emission. In turn, since laser emission is stimulated emission, which process is much faster than many non-radiative recombination processes, the quantum yield becomes significantly enhanced once the lasing threshold is achieved. Curve 3 in Fig. 3.2(b) displays the first demonstration of the ICG lasing with bovine serum albumin (BSA, 1.2 mM) in PBS under the same excitation as Curves 1 and 2. Strong laser emission peaks emerge on the red side of the ICG fluorescence spectrum (900 nm – 935 nm). The linewidth of each peak is approximately 0.18 nm, limited by the resolution of the spectrometer. Those lasing peaks exhibit an SBR as high as 800, nearly 20-fold improvement over that obtained with the fluorescence based measurement with the same BSA-ICG mixture under the same excitation (Fig. 3.1(c) shows a SBR of 40 for ICG-BSA fluorescence vs. background), attesting to the advantage of using laser emission in accurate determination of tumor boundaries and sensitive measurement analyte concentration changes [87].

In order to comprehensively understand the ICG lasing for prospective clinical and preclinical applications, we first studied the ICG lasing behavior of albumin, globulin and lipoprotein (Fig. 3.1(a)) with the ICG concentration well below the commonly used level in *in-*

vitro biological studies [91], as described in section 3.3.2.

3.3.2. Lasing with serological components

Albumins

As presented in Fig. 3.3, we investigated the ICG laser under different albumin/ICG molar ratios (Figs. 3.3(a-c)) and various ICG concentrations (Figs. 3.3(d-g)). Bovine serum albumin (BSA) in PBS was used as our model albumin, since it is the most abundant protein in blood plasma. We used five solutions with the molar ratio of BSA:ICG ranging from 2:1 to 3.3:1 while fixing the ICG concentration (0.4 mM). Fig. 3.3(a) presents the lasing spectra for different BSA/ICG molar ratios under the same excitation. Detailed studies reveal that different BSA/ICG ratios resulted in different lasing thresholds, as shown in Figs. 3.3(b) and 3.3(c), with a minimal lasing threshold of 0.38 $\mu J/mm^2$ for a molar ratio around 3:1. This phenomenon suggests that the ICG binding efficiency (or activation efficiency) plays an important role in ICG lasing. Indeed, in Fig. 3.4 we carried out regular fluorescence measurement with various BSA/ICG ratios. At a low BSA/ICG ratio, the fluorescence is relatively weak, suggesting that not all ICG molecules are activated (*i.e.*, bound to BSA molecule). When BSA/ICG=3, nearly all ICG molecules are bound to BSA and the fluorescence starts to saturate. Here our fluorescence results not only correlate well with our laser experiments, but also are consistent with a recent finding that a BSA molecule can bind at most one ICG molecule at a time [96,97]. Note that the slight reduction in fluorescence (and hence increase in the ICG lasing threshold) when excessive amount of BSA was added may be attributed to the additional absorption and scattering loss from BSA.

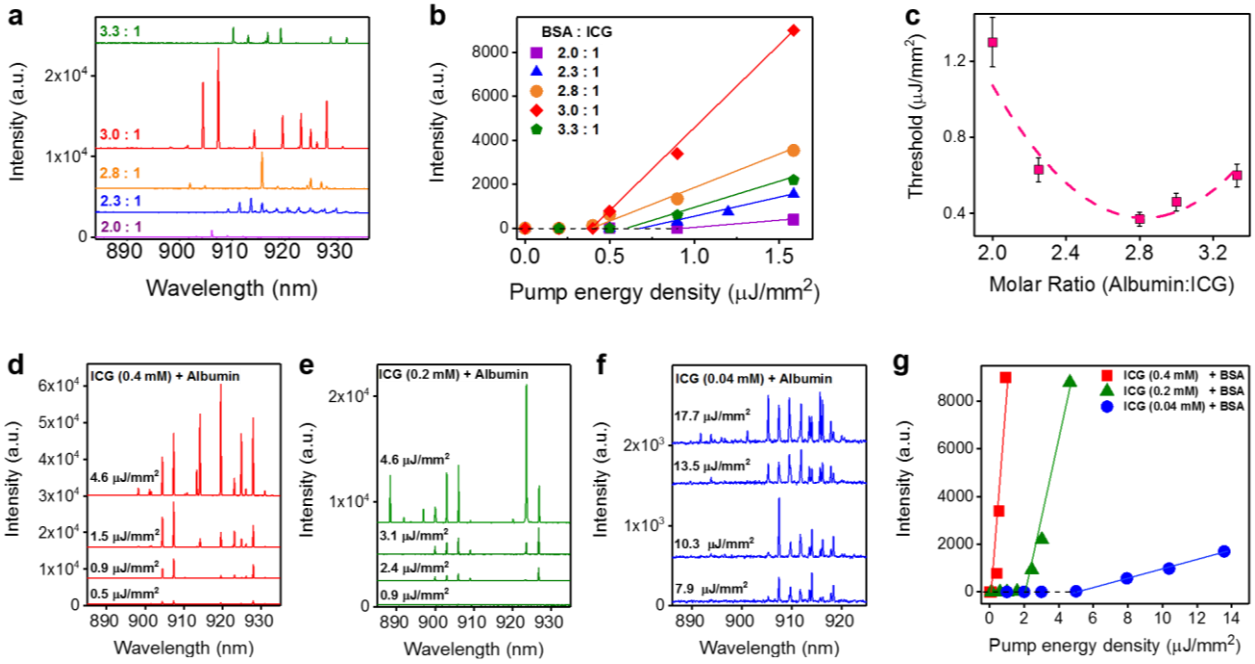

Figure 3.3. ICG lasing with bovine serum albumins. (a), Lasing spectra of ICG bound to albumin (BSA) with different molar ratios (BSA:ICG varying from 2:1 to 3.3:1)). All curves were obtained at the same concentration of ICG (0.4 mM) and same pump energy density of 1.4 μJ/mm^2. Curves are vertically shifted for clarity. **(b)** Spectrally integrated (900 nm – 930 nm) laser output as a function of pump energy density extracted from the spectra in a. The solid lines are the linear fit above the lasing threshold. **(c)** Lasing threshold as a function of the BSA:ICG molar ratio extracted from the linear fit in b. The minimum threshold of 0.38 μJ/mm^2 was observed around 3:1. The dashed curve is a quadratic fit to guide an eye. (d-f) Lasing spectra of 0.4 mM ICG **(d)**, 0.2 mM ICG **(e)**, and 0.04 mM ICG **(f)** bound to BSA under various pump energy densities. Multimode lasing with irregular spacing was observed as pump intensity increases. All curves in d-f were obtained with the same BSA:ICG molar ratio of 3:1. Curves are vertically shifted for clarity. **(g)** Spectrally integrated (900 nm – 930 nm) laser output as a function of pump energy density extracted from the spectra in d-f. The threshold based on the linear fit (solid lines) is approximately 0.4 μJ/mm^2, 2.3 μJ/mm^2, and 5.3 μJ/mm^2, respectively, for 0.4 mM, 0.2 mM, and 0.04 mM of ICG.

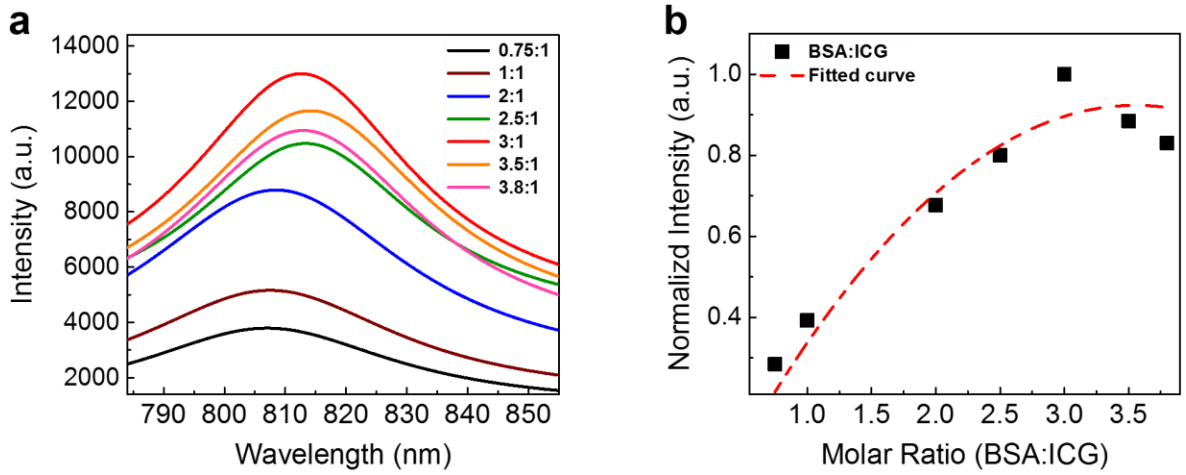

Figure 3.4. Fluorescence emission of ICG with different BSA ratios. (a) Fluorescence emission spectra of ICG in different concentrations of BSA. The concentration of ICG was fixed at 0.2 mM. The BSA/ICG ratio varied from 0.75 to 3.8. **(b)** Normalized fluorescence intensity as a function of the BSA/ICG molar ratio extracted from the peak value in (a). The red dashed curve shows the quadratic fitting of experimental data to guide an eye ($R^2 > 0.95$). Excitation wavelength=660 nm.

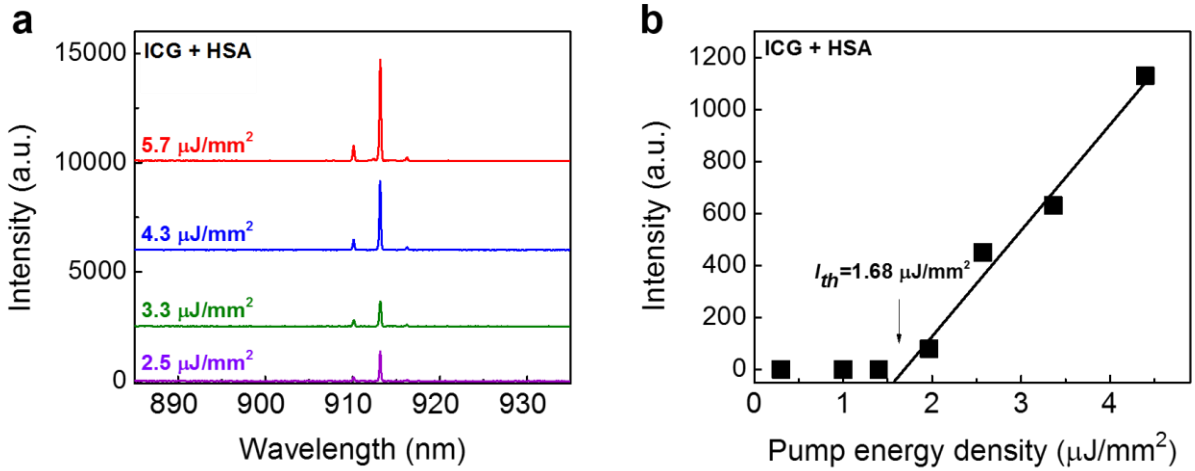

Figure 3.5. ICG lasing with human serum albumins. (a) Lasing spectra of ICG (0.2 mM) with Human Serum Albumin (HSA) under various pump energy densities. Curves are vertically shifted for clarity. **(b)** Spectrally integrated (900 nm – 920 nm) laser output as a function of pump energy density extracted from (a). Solid line is the linear fit above the threshold, showing a lasing threshold of approximately 1.68 μJ/mm².

To study the concentration dependency of the ICG lasing, Figs. 3.3(d-f) show the lasing spectra of three ICG concentrations at 0.04 mM, 0.2 mM and 0.4 mM, respectively, when the BSA/ICG ratio was fixed at 3:1. The corresponding lasing threshold curves are plotted in Fig. 3.3(g), showing the decreased threshold with the increased ICG concentration, which is typical for an optofluidic laser [67]. Even with the lowest ICG concentration (0.04 mM), the lasing threshold was only 5.3 μJ/mm^2. To mimic human plasma, we replaced BSA with human serum albumin (HSA) (fluorescence spectrum in Fig. 3.1(c)). Once again, a low lasing threshold of 1.68 μJ/mm^2 was obtained when ICG (0.2 mM) binds to HSA (0.6 mM) (Fig. 3.5). The slightly lower lasing threshold for HSA than for the BSA counterpart (2.3 μJ/mm^2) is due to the relatively high binding affinity of ICG to HSA [96] (hence the ICG quantum yield) as well as the red-shifted fluorescence (and the gain) spectrum (see Fig. 3.1(c)).

Globulins

Next, we studied globulins (GLBs), which take up nearly 35% of the plasma proteins. We used three different concentrations (0.1 mM, 0.2 mM and 0.3 mM in saline) of γ-GLB (one type of GLBs in blood) to cover the clinically relevant globulin concentration (~0.25 mM). The ICG concentration was fixed at 0.2 mM. However, no lasing emission could be observed even at a high excitation of 25 μJ/mm^2 (Fig. 3.6). Given that globulins have been reported to bind ICG molecules in previous papers [75,98-100], our result is surprising that GLB is unable to produce lasing. In Fig. 3.7, we investigated the cause of such negative results and discovered that the quantum yield of ICG when bound to GLB (~0.56%) is not as high as generally thought. It is actually about 7 times lower than that of ICG bound to BSA.

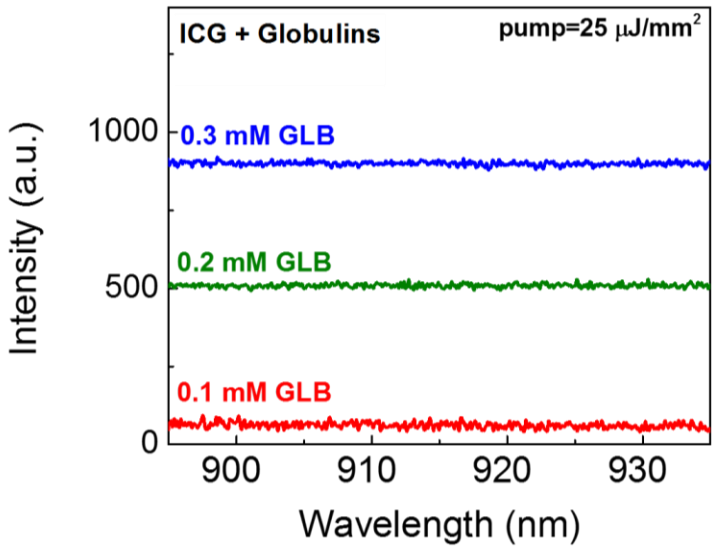

Figure 3.6. ICG lasing with globulins. Emission spectra of the mixture of ICG (0.2 mM) and γ-globulins of different concentrations. All curves were pumped under a pump energy density of 25 μJ/mm^2. In human, the average concentration of γ-globulins was approximately 0.25 mM, within the concentration range that we investigated in the current work. No lasing was observed.

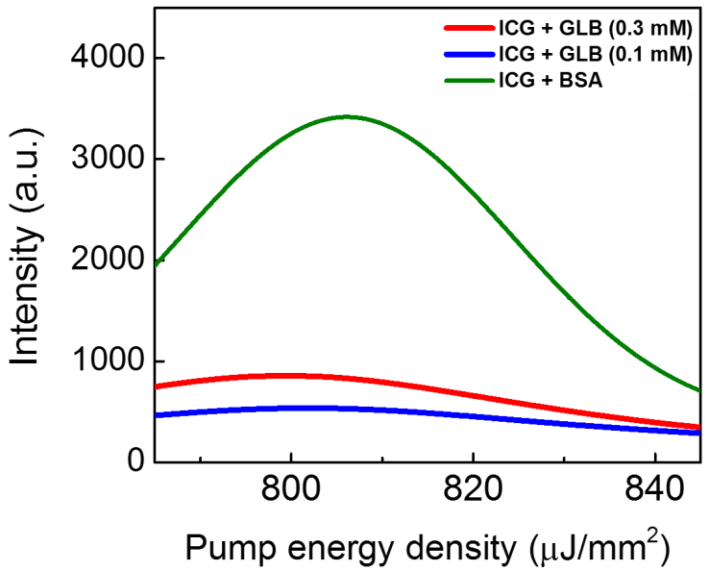

Figure 3.7. Fluorescence emission of ICG with globulins. Emission spectra of ICG with γ-globulins (0.1 mM) (blue curve) and ICG with γ-globulins (0.3 mM) (red curve), compared to ICG with BSA (0.6 mM) under the same pump energy density. The ICG concentration was fixed at 0.2 mM for all experiments. Excitation wavelength=660 nm.

Lipoproteins

Besides plasma proteins, lipoproteins are another major serological component. Lipoproteins are complex particles that carry lipids such as triglycerides and cholesterol through the bloodstream. They are simply classified into high-density (HDL) and low-density (LDL) lipoproteins, in which LDL level is regarded as a critical criterion for *cardiovascular* diseases. To determine whether ICG binds to lipoproteins and generates lasing emission, we investigated LDL in PBS with a concentration matching that in human blood (~0.01 mM). The ICG concentration was fixed at 0.2 mM. In Fig. 3.8(a) we present the lasing emission spectra for LDL pumped under various pump energy densities. Compared to ICG lasing for albumins (center around 920 nm), lasing peaks for LDL emerged at longer wavelengths (around 930 nm) due to the red-shift of the ICG-LDL fluorescence (hence the gain) profile (see Fig. 3.9). Further pump energy density dependent experiments in Fig. 3.8(b) show a remarkably low threshold of only 0.17 $\mu J/mm^2$, which is over 10X lower than the corresponding ICG-BSA lasing (threshold = 2.3 $\mu J/mm^2$ given in Fig. 3.3(g)) and ICG-HSA lasing (threshold = 1.68 $\mu J/mm^2$ given in Fig. 3.5) that have the same ICG concentration (0.2 mM). Such a low threshold can be accounted for by the higher gain (proportional to the quantum yield, which is 12.8 % for ICG-LDL) of ICG-LDL than that of ICG-BSA and ICG- HSA.

The above result becomes even more significant when we consider that the LDL concentration (0.01 mM) used was 60 times lower than BSA and HSA (0.6 mM). Previously it was thought that albumins are responsible for enhanced fluorescence in blood [77,98,101]. However, recent studies revealed that ICG might bind mainly to lipoproteins [71,77,97,102,103]. Indeed, our fluorescence measurement shows that lipoproteins bind more ICG and produce approximately 3 times stronger emission than albumins (Fig. 3.9), despite 60 times of difference in lipoprotein and

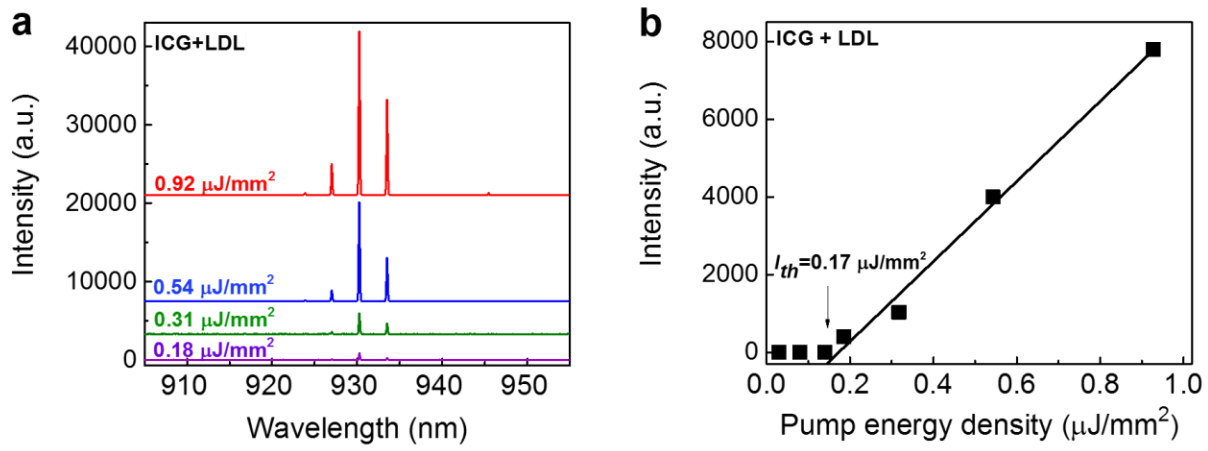

Figure 3.8. ICG lasing with lipoproteins. (a) Lasing spectra of ICG bound to low-density lipoprotein (LDL) under various pump energy densities. The respective concentration of ICG and LDL was 0.2 mM and 0.01 mM, respectively. Curves are vertically shifted for clarity. **(b)** Spectrally integrated (920 nm – 940 nm) laser output as a function of pump energy density extracted from the lasing spectra. The threshold obtained from the linear fit is approximately 0.17 μJ/mm².

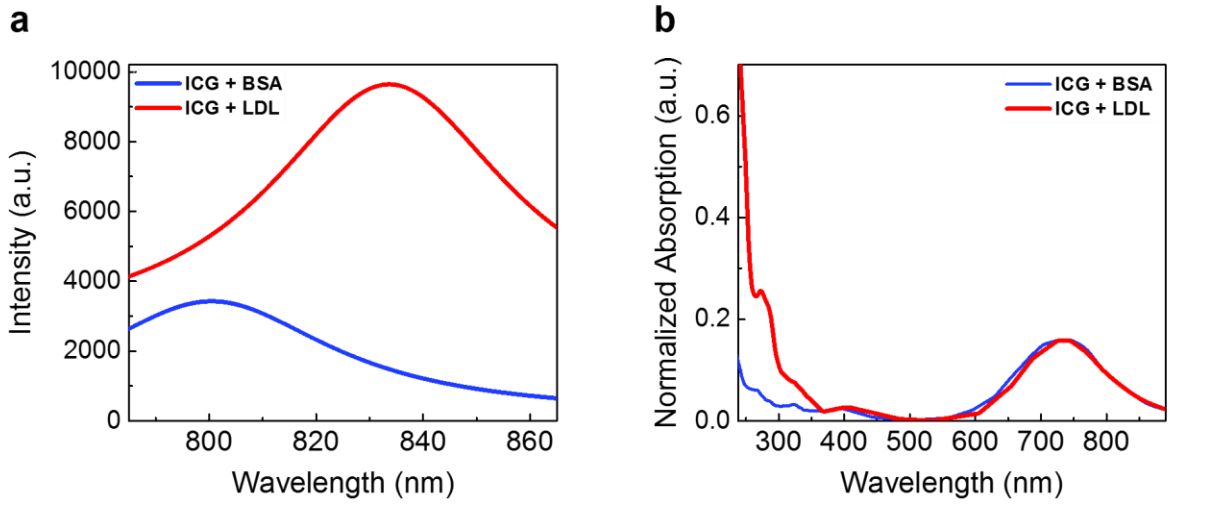

Figure 3.9. Absorption and emission spectra of ICG with lipoproteins. (a) Comparison of the emission spectra of ICG with LDL (0.01 mM) and ICG with BSA (0.6 mM) shows that the QY for ICG with LDL is approximately 12.8%. **(b)** Normalized absorption spectra of ICG with LDL (0.01 mM) and ICG with BSA (0.6 mM). The absorption peak at 750 nm is due to ICG molecules, whereas the strong absorption at UV wavelengths is due to the intrinsic absorption of proteins and lipoproteins. The ICG concentration was fixed at 0.2 mM. Excitation wavelength=660 nm.

albumin concentrations. Our lasing experiment offers another evidence to support the above finding. Furthermore, this suggests that we can obtain the ICG lasing for lipoproteins well before for albumins, thus providing a unique means to sensitively monitor lipid levels in blood. In fact, due to the threshold behavior, the signal difference between ICG-lipoprotein (lasing emission) and ICG-albumin (fluorescence) can be as high as 100-1000 times [27,87,89], orders of magnitude larger than the 3 times difference in the conventional fluorescence measurement.

Serum

Moving a step forward, we explored the ICG lasing possibility in human serum, which contains abundance of plasma proteins, lipoproteins, antibodies, hormones and antigens. As a control experiment (Fig. 3.10(a)), no lasing emission was observed from serum itself. In contrast, as we added ICG (0.2 mM) into serum, lasing emission could easily be observed (Fig. 3.11(a)). The lasing threshold is 0.45 μJ/mm^2 (Fig. 3.11(b)), falling between that of HSA and LDL, as ICG molecules bind to both plasma proteins and lipoproteins. We also measured serum by using ICG with a concentration as low as 0.04 mM, lasing was obtained with a threshold of 3.4 μJ/mm^2.

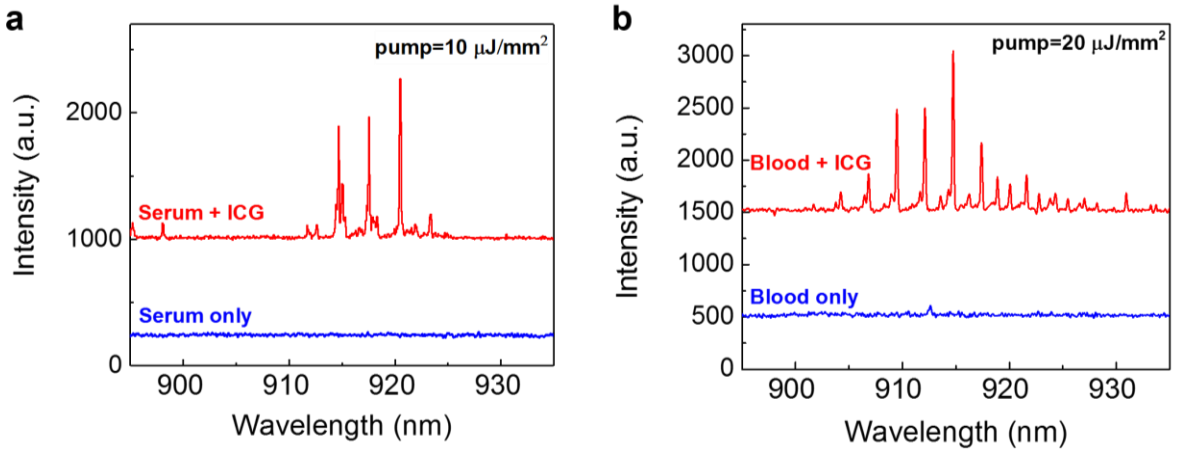

Figure 3.10. Control experiment of lasing with serum and blood. (a) Comparison of the lasing spectra of serum alone and serum mixed with ICG (0.04 mM) under pump of 10 μJ/mm^2. **(b)** Comparison of the lasing spectra of human whole blood alone and whole blood mixed with ICG (0.04 mM) under pump of 20 μJ/mm^2. Excitation wavelength=660 nm.

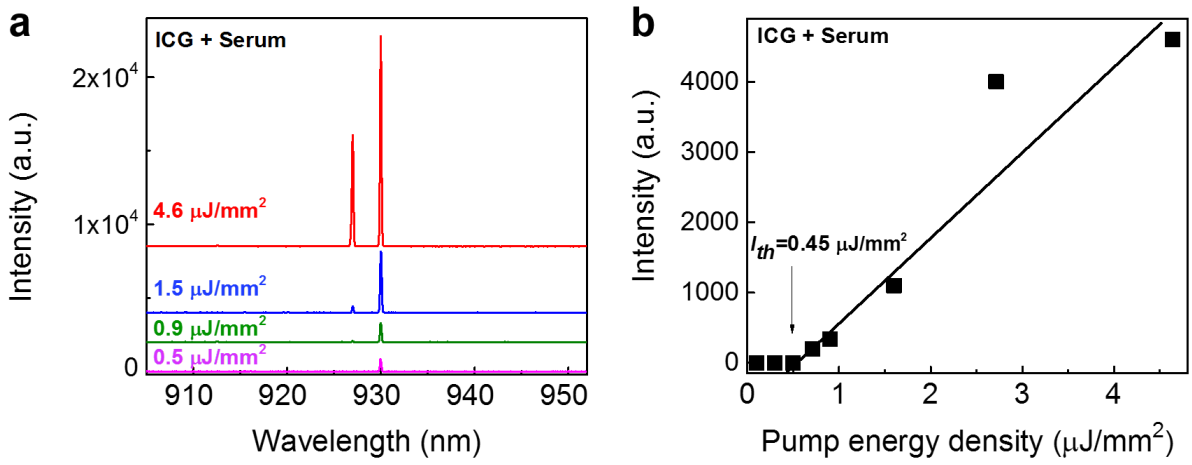

Figure 3.11. ICG lasing with human serum. (a) Lasing spectra of ICG bound to human serum under various pump energy densities. The concentration of ICG was 0.2 mM. Curves are vertically shifted for clarity. **(b)** Spectrally integrated (920 nm – 940 nm) laser output as a function of pump energy density extracted from a. The threshold obtained from the linear fit is approximately 0.45 μJ/mm^2.

3.3.3. Lasing in whole blood

Our work culminated in achieving direct lasing from "whole blood". As a control experiment, we first flowed human whole blood (2X diluted in PBS to avoid clogging) through the OFRR as illustrated in Fig. 3.12(a). Upon excitation, no lasing emission was observed even at a high excitation of 25 μJ/mm^2 (Fig. 3.10(b)). In contrast, when ICG (0.04 mM) mixed with human whole blood (2X diluted in PBS to avoid clogging), the lasing band emerged at 915 nm (Fig. 3.12(b)). The spectrally integrated laser emission versus pump energy density for blood with ICG is presented in Fig. 3.12(c), in which the lasing threshold is derived to be approximately 10 μJ/mm^2. The relatively high lasing threshold results from the relatively low concentration of plasma proteins and lipoproteins in whole blood as compared to that in the serum in our previous studies. Moreover, blood cells and other serological components cause disturbance in the gain media,

which could significantly degrade the OFRR Q-factor. Nevertheless, this lasing threshold is still >20X lower than the current standard for clinical surgery [95], which is considered to be bio-safe and noninvasive.

Fig. 3.12(d) presents the ICG concentration dependent study of the "blood lasing" under the same pump intensity of 20 μJ/mm^2. The ICG concentration ranged from 0.01 mM to 0.06 mM, which is within the normal ICG clinical dosage allowed in the circulation system of a human body. Again the blood sample was 2X diluted. As shown in the black curve of Fig. 3.12(d), only featureless emission was observed for 0.01 mM ICG. The most prominent blood lasing was achieved when the ICG concentration was around 0.035 mM to 0.04 mM. However, the laser intensity began to drop dramatically when ICG was higher than 0.06 mM and no laser emission was observed beyond.

Our concentration dependent laser emission results are consistent with the previous studies on fluorescence, which show that strong fluorescence is observed when the ICG concentration is 0.04 mM to 0.08 mM [104]. The maximum intensity around 0.065 mM indicates a critical point at which nearly all binding sites in whole blood are occupied by ICG molecules. As such, the fluorescence begins to decrease as the ICG concentration increases beyond 0.065 mM, which can be attributable to two possible factors, *i.e.*, the increased absorption from excessive unbound ICG molecules and the self-quenching effect of ICG molecules [105]. Note that the two times difference in the optimal ICG concentration between lasing (0.035-0.04 mM) and regular fluorescence (0.065 mM) is due to the 2X dilution in blood samples used in our experiment.

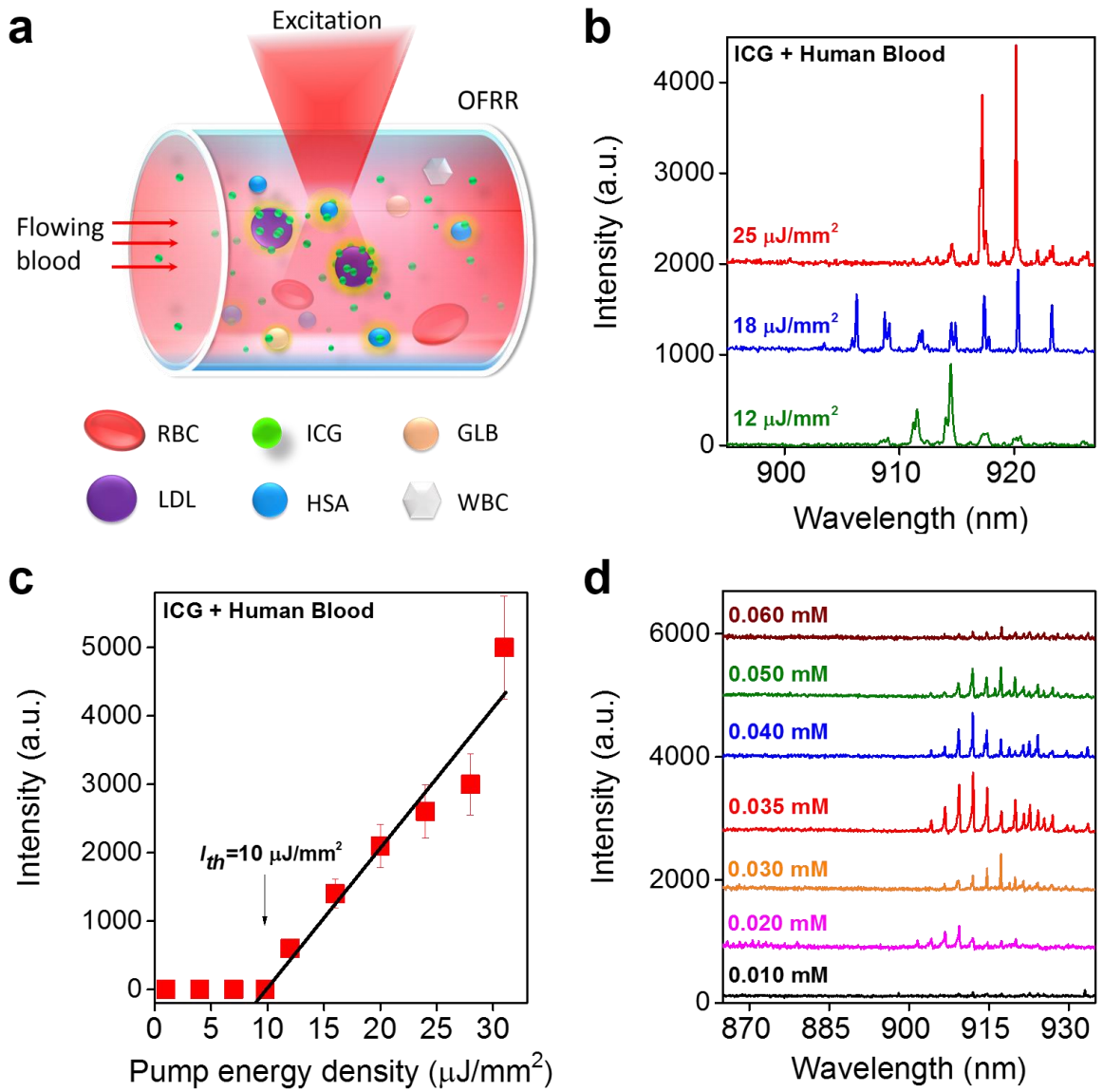

Figure 3.12. ICG lasing with human whole blood. (a) Schematic showing the excitation process of human whole blood flowing through an OFRR. RBC: red blood cell; WBC, white blood cell (leukocytes). **(b)** "Blood" lasing spectra under various pump energy densities when ICG (0.04 mM) were injected into the OFRR along with real human whole blood (2x diluted with PBS buffer to avoid clogging). Curves are vertically shifted for clarity. **(c)** Spectrally integrated (900 – 930 nm laser output as a function of pump energy density extracted from the lasing spectra. **(d)** Concentration dependent study of the "blood" lasing with various ICG concentrations (0.01 mM – 0.06 mM) in human whole blood (2X dilution with PBS buffer to avoid clogging). A red shift is observed as the pump increases. No lasing emission was observed when the ICG concentration was above 0.06 mM. The pump energy density was fixed at 20 μJ/mm^2. Curves are vertically shifted for clarity.

3.4. Conclusion

In this work, we demonstrated the first "blood laser" using the only FDA approved near infrared dye, ICG, in human whole blood with the dye concentration within the clinically acceptable range. In addition, we also investigated the ICG lasing behavior in three major serological components (albumins, globulins, and lipoproteins) using the ICG concentration lower than the typical concentration used in *in-vitro* studies on cells and excised tumor tissues. In all studies, the pump intensity is orders of magnitude lower than the exposure level that may cause damage to cells or tissues. Furthermore, we found that it is albumins and lipoproteins that are responsible for ICG lasing and that lipoproteins are far more effective than albumins in achieving ICG lasing.

Our work opens a door to a broad range of clinical and biomedical applications *in-vivo* and *in-vitro* that provide superior sensitivity and imaging quality than fluorescence counterparts, such as *in-vitro* examination of excised tumor tissues, *in-vitro* diagnostics in whole blood (cancer cell detection and monitoring of lipid in blood), *in-vivo* tumor margin determination during surgery, preclinical research applications, and single cellular bioanalysis, just to name a few. Together with the recent advancement in optofluidic cellular lasers [6,20,35,36], lasing in whole blood (which is tissue and generally considered to be closer to actual complex biological samples than cells) represents a critical step towards eventual clinical applications of optofluidic lasers.

As an outlook, below we present a few clinical, preclinical, and biomedical scenarios where the ICG laser may be implemented, and discuss the challenges it faces. (1) Image guided surgery and screening. In this scenario, the ICG is first administered to patients, and then the suspected tumor is removed and examined under a fluorescence microscope. As discussed previously, ICG

lasing may help improve differentiation and identification of vital structures in tissues. To implement, a high-Q Fabry-Perot cavity (the Q-factor is as high as $6x10^5$ [106], close to that of the OFRR used in the current work) can be employed for in-vitro biological imaging and spectroscopy due to its planar format. (2) *In-vivo* characterization and differentiation of tissues. In this scenario, macroscopic laser cavities such as Fabry-Perot cavities and ring resonators discussed above may not be applicable. In contrast, the random laser [42,107] and plasmonic laser [108] offer a possible tool to realize lasing at the microscopic and nanoscopic scales. However, it should be noted that those types of laser cavities usually have much lower Q-factors, which may require higher ICG concentrations and pump intensities. Therefore, more work needs to be carried out in the future to develop cavities that are compatible with *in-vivo* tissues and have relatively high Q-factors. Meanwhile, new methods that can deliver higher concentration of ICG, which helps lower the pump intensities required for lasing, while maintaining clinical safety, should also be investigated. One example in this regard is high concentrations of ICG encapsulated in clinically compatible nanoparticles applications recently demonstrated [109,110]. (3) Hyperspectral imaging. It has shown the great potential by combining laser spectroscopy with imaging, thereby providing both higher spectral/spatial information and image contrast [84,85,111]. The ICG lasing presented in this chapter will also lead to the development of novel hyperspectral imaging technologies that complement conventional fluorescence techniques.

Chapter 4

Versatile Tissue Lasers for Multiplexed Detection

Besides lasing with liquid biopsy (Chapter 3), here in Chapter 4 we developed a highly versatile tissue laser platform, in which tissue biopsy stained with fluorophores are sandwiched in a high-Q Fabry-Pérot microcavity. Distinct lasing emissions from muscle and adipose tissues stained respectively with fluorescein isothiocyanate (FITC) and boron-dipyrromethene (BODIPY), and hybrid muscle/adipose tissue with dual-staining were achieved with a threshold of only ~10 $\mu J/mm^2$. It is further found that, despite large fluorescence spectral overlap between FITC and BODIPY in tissues, their lasing emissions could be clearly distinguished and controlled due to their narrow lasing bands and lasing thresholds, thus enabling highly multiplexed detection.

4.1. Introduction

4.1.1. Tissue-based lasers

Biological lasers[6] is an emerging field that studies lasing emission from biological and biochemical materials such as proteins[17-19], vitamins[15], luciferins[14], DNAs[23,33,89,112], and cells[17,35-38,113], when they are labelled with external fluorophores or they themselves can produce the gain media (such as in the case of fluorescent proteins)[6,14,35,37,52,114]. Advances in biolasers have demonstrated great potential in biosensing, biomedical research, and diagnosis[17,38,42,52,115,116] due to their capability to amplify subtle changes in the gain media caused by underlying biological processes, which, in combination of threshold behavior, narrow linewidth, strong lasing emission,

and lasing mode spatial distribution, may lead to significant increase in detection sensitivity, multiplexibility, and imaging contrast[27,30,50,89]. Over the past few years, biolasers have been focused mainly on the molecular level and cellular level for detecting biomolecules and their structural changes[9,18,23,32,87,88]. Moving beyond the molecular and cellular level, tissues, which consist of a collection of cells embedded in extracellular matrix, are generally considered to be more practical, since they mimic the actual complex biological environment in a living body. Consequently, lasing in tissue (tissue laser) may lead to a broad range of applications in biological research, medical diagnosis, and tissue engineering.

In the past, tissue lasers have been demonstrated in the form of random lasers with a single type of fluorophore[41,42,116-118], showing capabilities to differentiate and sensitively analyze subtle inhomogeneities at the submicron scale[116]. Additionally, lasing from fat tissues based on whispering-gallery modes (WGM) of natural lipid droplets in adipocytes has been succeeded lately[36]. However, random lasers rely on strong scatters (*i.e.*, tissue inhomogeneities) to provide optical feedback for lasing and do not have a fixed cavity. Therefore, they are unable to provide predicable and trackable laser emission signals with precise locations on the tissue. In addition, the lasing characteristics (*e.g.*, intensity and threshold) vary drastically from one tissue sample to another or from one spot to another on the same tissue due to the nature of random lasers. WGM lasers, on the other hand, require the internal spherical structures of an adipocyte and thus can only be used for fat tissues. In both the random laser and the lipid droplet laser, the strong background emission from fluorophores and tissues themselves that do not participate in laser action can be coupled into the detection system (such as a spectrometer or photodetector) along with the actual lasing signal, thus considerably compromising the signal-to-background ratio (SBR) and hence the

detection sensitivity and imaging contrast. Those drawbacks significantly limit practicality and applicability of the tissue lasers.

4.1.2. Multiplexed detection

Furthermore, detection and differentiation of specific targets (*e.g.*, cancer antibodies) in biological tissues have become a critical issue recently[119-121]. However, the biomedical community has come to recognize that no single target analyte is likely to provide sufficient information needed to characterize a specific disease in tissues. The ability to detect multiple targets simultaneously with a higher sensitivity is therefore highly desirable[122]. A number of approaches have been demonstrated to achieve multiplexed detection and imaging based on fluorescence[123], photoluminescence[124], and Raman spectroscopy[125]. However, huge spectral emission overlap among fluorophores and weak signals (*i.e.*, low SBR) of Raman scattering still restrict their applications. In contrast, lasing emission can potentially provide an extremely high SBR and a narrow emission band. Unfortunately, the random tissue laser in its current form is unable to detect biochemical/biological reactions from specific targets, as the underlying lasing mechanism is mainly based on physical properties of tissues (such as inhomogeneities), whereas the lipid droplet laser can only react with and detect lipid droplet inside a cell.

Those challenges motivated us to develop a new versatile tissue laser platform, in which tissues stained with various fluorophores are sandwiched in a high-Q Fabry-Pérot (FP) microcavity, as illustrated in Fig. 4.1(a). The fluorophores serve as the laser gain medium. Upon external excitation, the tissue laser is achieved locally around the focal spot of the pump light. In this chapter, we demonstrated for the first time this FP tissue laser. Distinct lasing emissions from muscle tissue stained with fluorescein isothiocyanate (FITC), adipose tissue stained with boron-dipyrromethene (BODIPY), and hybrid muscle/adipose tissue dual-stained with FITC and

BODIPY were achieved with a lasing threshold on the order of 10 μJ/mm^2 using the same pumping wavelength. We further systematically investigated the lasing characteristics of the tissue laser for various tissue structures/geometries, tissue thicknesses, and staining dye concentrations. Finally, we achieved lasing from FITC conjugated with phalloidin that target specifically F-actin in muscle tissues.

Our studies reveal the advantages of the FP tissue laser over conventional fluorescence. Despite the large fluorescence spectral overlap (~100 nm) between the two fluorophores, FITC and BODIPY, lasing bands from muscle and adipose tissues can be clearly distinguished by their well separated lasing bands and different lasing threshold, thus enabling highly multiplexed spectral detection. In addition, the lasing emission has two orders of magnitude improvement in SBR over fluorescence, significantly enhancing imaging contrast. Our tissue laser platform can be readily and broadly applicable to nearly any types of tissues/diseases, and outperforms previous random tissue lasers and WGM lipid droplet lasers with a low lasing threshold, high sample-to-sample and location-to-location repeatability, high SBR, multiplexed detection capability, and the capability to target specific biomarkers in a tissue. It will open a door to a wide range of applications in medical diagnostics and screening of tissues, as well as identification and monitoring of biological transformations in tissue engineering.

4.2. Experimental setup

Optical system setup

A typical confocal setup was used to excite the sample and collect emission light from the FP cavity (Fig. 4.1(a)). In this work, a pulsed OPO laser (pulse width: 5 ns, repetition rate: 20 Hz) with 465 nm was used as the excitation source to excite the stained tissues with a laser beam size

of 25 μm in diameter. The pump intensity was adjusted by a continuously variable neutral density filter, while the lasing emissions were collected through a top CCD and spectrometer.

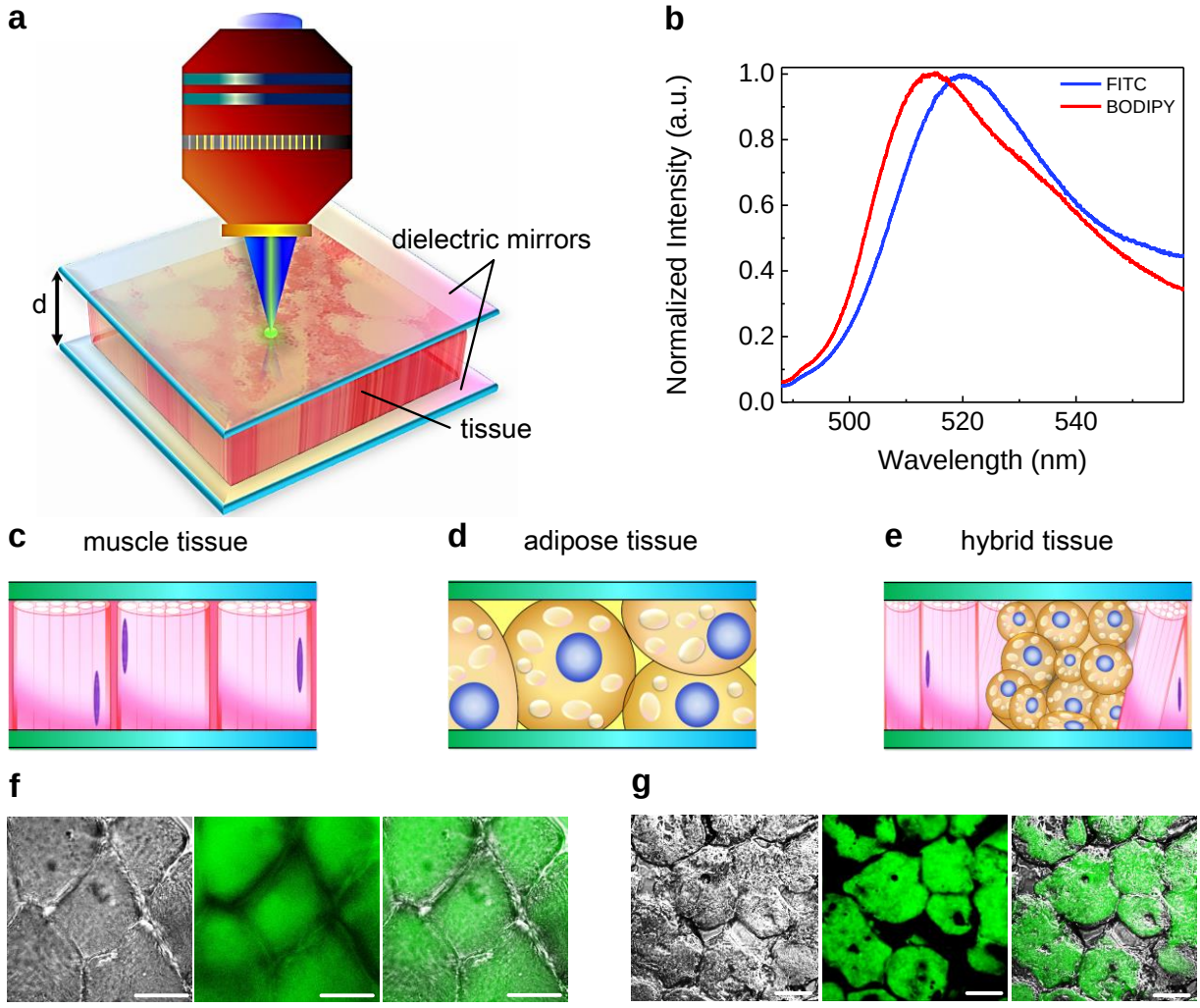

Figure 4.1. Schematic showing the concept of a tissue laser. (**a**) Illustration of the tissue lasing when a tissue is sandwiched within a high-Q Fabry-Pérot (FP) cavity. The thickness of tissue (*i.e.*, the cavity spacing) is denoted as *d*. The typical values for the cavity spacings (*d*) are around 10-50μm. During the experiment, the sample was excited by a pulsed optical parametric oscillator (OPO) (pulse width=5 ns; wavelength=465 nm). (**b**) Normalized fluorescence emission spectra of FITC in water (blue curve) and BODIPY in ethanol (red curve). **c-e**, Different types of tissues investigated in this work, including muscle tissue (**c**), adipose tissue (**d**), and hybrid tissue (**e**). **f**, Microscopic images of myocytes stained with FITC (from left to right): differential interference contrast (DIC) image, confocal microscopy image, and overlap image. (**g**)Microscope images of adipocytes stained with BODIPY (from left to right): DIC image, confocal microscopy image, and overlap image. Scale bars, 20 μm.

Optical imaging techniques

The differential interference contrast (DIC) and confocal fluorescence microscopic images were taken by using Nikon A1 Spectral Confocal Microscope with an excitation of 488 nm laser source. The bright field images of tissue lasing were captured by using a CCD (Thorlabs #DCU223C) integrated directly on top of the objective in our laser experimental setup in Fig. 1(a).

FP cavities

The FP cavity was formed by two customized dielectric mirrors (Fig. 4.2). The top mirror (made by Qingdao NovelBeam Technology Co. Ltd, China) had a high reflectivity in the spectral range of 500-555 nm to provide optical feedback and high transmission around 465 nm for the pump light to pass through, whereas the bottom mirror (made by Evaporated Coating INC, USA) had a slightly wider reflection band. Most part of the top mirror was flat, thus forming a plano-plano (p-p) FP cavity with the flat bottom mirror. The top mirror also had an array of concave structures, made by the computer-controlled CO_2 laser ablation (before dielectric coating), thus forming a plano-concave (p-c) FP cavity that have better cavity stability and higher Q-factors. The Q-factor for the p-p and p-c FP cavity was on the order of 10^4 and 10^5, respectively, at a cavity length of 30 μm (in the absence of tissues). Details of the fabrication and characterization of the p-p and p-c FP cavities are described in the reference[106].

4.3. Materials and methods

Tissue and device preparation

All the fresh pig tissues were obtained from the local slaughterhouse. In this work, the muscle and fat tissues were selected from pig ribs without any processing or fixing. Fresh tissues were frozen immediately and embedded into OCT (Optimal Cutting Temperature) compound to

form an OCT tissue block under -20 °C. Tissue sections were then sliced into thin sections (20 μm, 30 μm, and 40 μm in thickness) by using a cryostat (Leica 3000). Selected sections were picked up and placed on the top of a poly-L–lysine (Sigma-Aldrich #P8920) coated dielectric mirror (see Fig. 4.2 for details of the mirrors), which were first cleaned and rinsed with Lysine for better tissue adhesion. Tissues were then rinsed with PBS (phosphate buffered solution, R&D Systems #841380, #896009) and air dried before staining. After staining (see details about staining in the next section) and appropriate rinsing again, the tissue was mounted with PBS and covered by the top dielectric mirror. For confocal microscopy, the tissues were first deposited on the top of a glass slide (Thermo-fisher #3021-002), followed by the same staining process, and then mounted with Fluoromount (Sigma-Aldrich #4680) and covered with a coverslip before scanning.

Staining and materials

For muscle tissues, FITC powder (Sigma-Aldrich #F6377) was dissolved in de-ionized (DI) water at a concentration of 3 mM, then diluted to lower concentrations. FITC solution was then applied to the muscle tissue for 10 minutes and rinsed with PBS solution 3 times before measurement. For adipose tissues, BODIPY (Life-Tech #D3922) was dissolved in pure ethanol at a concentration of 3 mM, then diluted to lower concentrations with ethanol. BODIPY solution was then applied to the adipose tissue for 20 minutes and rinsed with PBS solution 3 times before measurements. For dual staining of the hybrid tissue, we first applied 2 mM FITC solution to the tissue for 10 minutes and rinsed with PBS for 3 times and then 1 mM BODIPY solution for 20 minutes and rinsed with PBS solution 3 times. For specific staining using FITC-phalloidin (Thermo Fisher #F432), the bulk solution was diluted with methanol to form a 10 μM solution and applied to the muscle tissue sections for 20 minutes as suggested. Then the tissue was rinsed with PBS for 3 times before measurement.

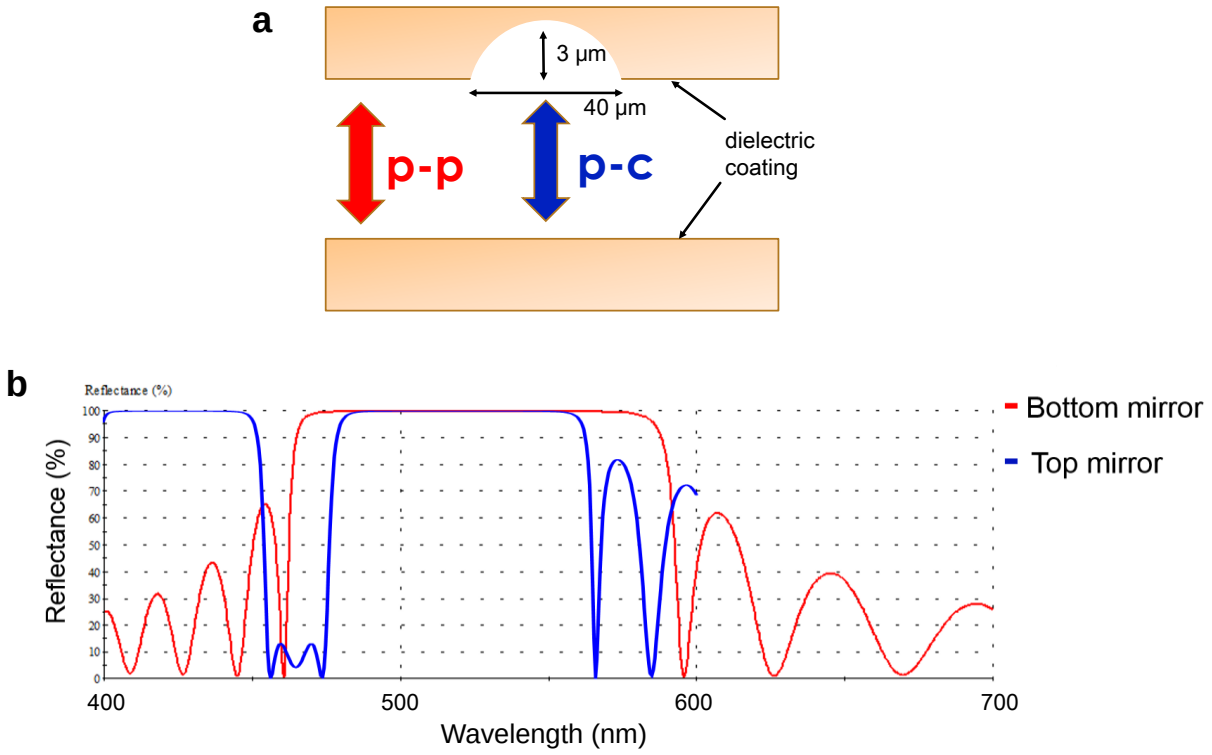

Figure 4.2. Properties of FP cavity. (a) Schematic of the structure of the FP cavity, showing both the plano-plano (p-p) and the plano-concave (p-c) configuration. The concave well array on the top mirror was created using CO_2 laser ablation before dielectric coating. The two adjacent concave wells were 3 mm apart. The rest area on the mirror was flat. (**b)** The reflectance spectra of the top mirror (blue curve) and the bottom mirror (red curve).

4.4. Results and discussion

4.4.1. Lasing in muscle tissues

Figure 4.1(a) illustrates the concept of the FP tissue laser. The detailed description of the experimental setup is presented in Experimental section. The FP cavity was formed by two dielectric mirrors. The details of the mirror fabrication and characterization, as well as FP cavity assembly, can be found in Experimental and Fig. 4.2. We used FITC and BODIPY, the two commonly used dyes in tissue staining[126-128], as the exemplary gain media. Their fluorescence emission spectra are given in Fig. 4.1(b), showing strong spectral overlap over 100 nm. Further,

we chose three major types of tissues as the model system, *i.e*., muscle tissue, adipose tissue, and hybrid tissue, as illustrated in Figs. 4.1(c-e). FITC and BODIPY were used to stain muscle tissue (*myocytes*) and adipose tissue (*brown adipocytes*), respectively. Fig. 4.1(f) shows the DIC and confocal fluorescence microscopy images of a muscle tissue stained with FITC. Since FITC is a non-specific dye, physical absorption of dyes throughout the whole tissue takes place as the main staining mechanism. Nevertheless, it can still be clearly observed that the inner part of each myocyte was stained by more FITC due to its slight binding ability to primary amine groups of proteins[129,130]. The DIC and confocal images of adipose tissue stained with BODIPY are given in Fig. 4.1(g). Obviously, since BODIPY is a lipophilic stain, it labels all the lipid droplets randomly distributed throughout the whole brown adipocyte.

We first investigated the feasibility and characteristics of the tissue laser under various muscle tissue thicknesses and FITC concentrations in Fig. 4.3. All the muscle tissue sections were prepared so that muscle fibers (myofibrils) were in the longitudinal direction (*i.e*., the myofibrils were aligned perpendicularly to the mirror surface and in parallel to the laser emission). The lasing spectra of a 30 μm thick muscle tissue stained with 2 mM FITC under various pump intensities are shown in Fig. 4.3(a). Sharp and periodic lasing peaks start to emerge around 553 nm with an overall lasing band of only ~10 nm (545 nm – 555 nm), much narrower than the corresponding fluorescence band (>50 nm in Fig. 1b), which is typical for lasing emission[25,45,131]. The spectral linewidth of each lasing peak is 0.2 nm[45], limited by the spectrometer resolution. It should be noted that, in comparison with the lasing wavelength of pure FITC in the absence of muscle tissue (centered around 525 nm – see Fig. 4.4), a 30 nm red-shift in the FITC stained tissue laser was observed, which is due to myoglobin in muscle tissue that has a lower extinction coefficient at 555 nm than 525 nm[132]. The spectrally integrated laser emission versus pump energy density extracted

from Fig. 4.3(a) is presented in Fig. 4.3(b), from which the lasing threshold is derived to be approximately 9.2 μJ/mm^2, similar to our theoretical analysis and simulation in the next section.

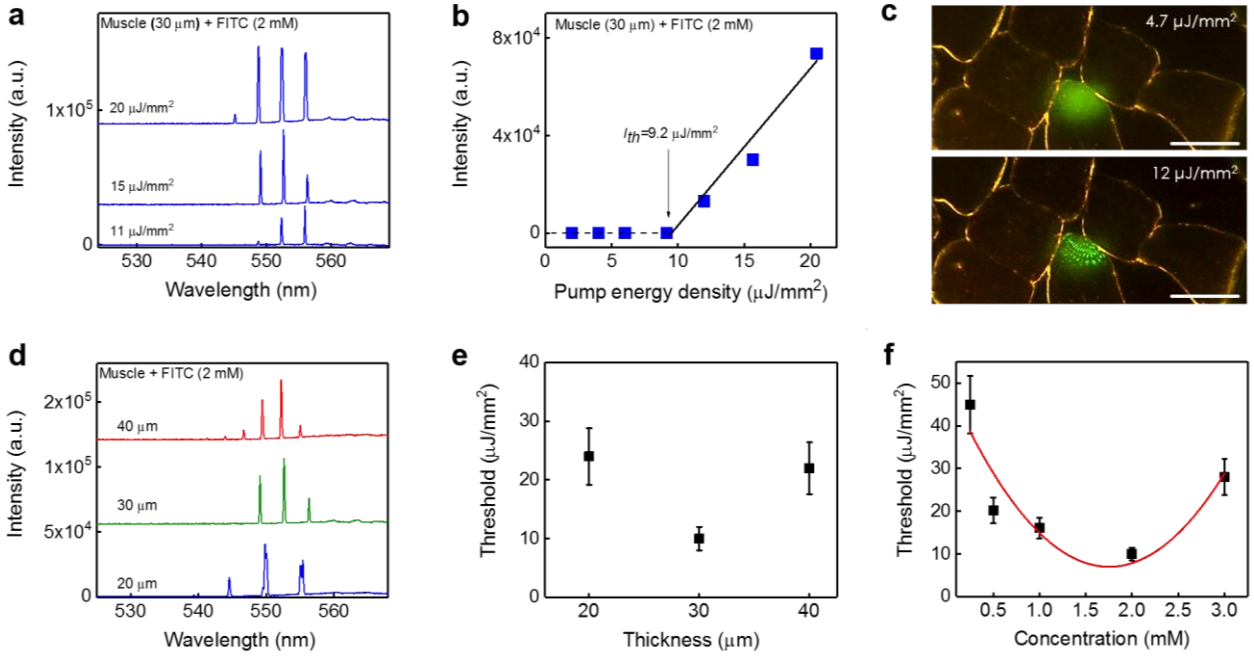

Figure 4.3. Lasing in muscle tissue - longitudinal myofibrils. (a) Examples of lasing spectra of muscle tissue (30 μm) stained with FITC (2 mM) under various pump energy densities. Curves are vertically shifted for clarity. **(b)** Spectrally integrated (545 nm – 560 nm) laser output as a function of pump energy density extracted from the spectra in **a**. The solid lines are the linear fit above the lasing threshold, which is 9.2 μJ/mm^2. **(c)** CCD images of the muscle tissue laser output below (4.7 μJ/mm^2) and above (12 μJ/mm^2) the lasing threshold. The image shows clearly several myocytes. The laser beam was, however, focused on only one of the myocytes. Scale bars, 20 μm. **(d)** Lasing spectra of muscle tissue with different section (cavity) thicknesses (*d*) at 35 μJ/mm^2 (all of which were above the lasing threshold). Curves are vertically shifted for clarity. **(e)** Laser threshold for different tissue thicknesses. The concentration of FITC used to stain the tissue was 2.0 mM. Error bars were based on three individual measurements at different sites. **(f)** Laser threshold with different concentrations of FITC used to stain the tissue at the fixed tissue thickness (and hence the cavity length) of 30 μm. The solid curve is a quadratic fit to guide an eye. Error bars were based on three individual measurements at different sites.

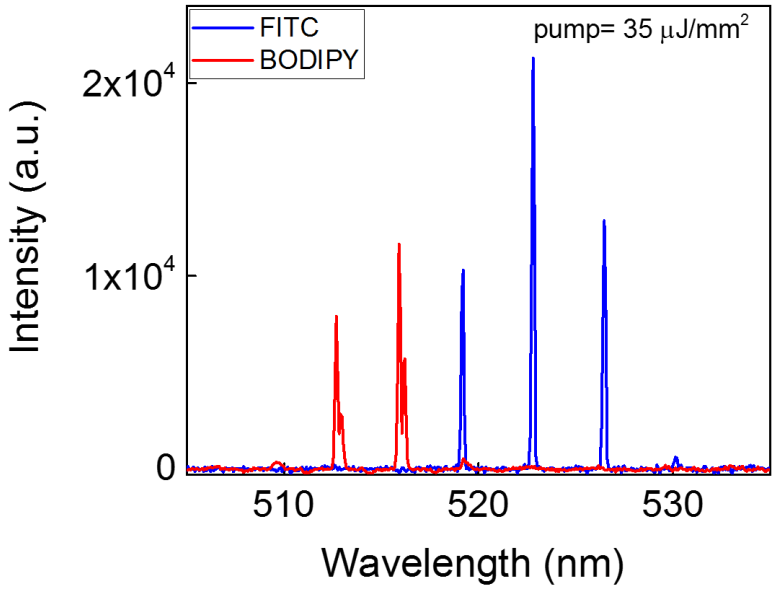

Figure 4.4. Lasing spectra of FITC and BODIPY. Laser emission spectra of FITC in water (blue curve), BODIPY in ethanol (red curve). Excitation wavelength=465 nm. Pump intensity=35 μJ/mm^2. [FITC]=2.0 mM. [BODIPY]=1.0 mM. Cavity length=30 μm. The lasing emission of FITC was within the range of 520 nm – 530 nm, whereas the lasing emission of BODIPY was within the range of 512 nm – 520 nm. The center of the lasing emission band for FITC is about 10 nm red-shifted with respect to that of BODIPY due to the slightly red-shift gain profile of FITC (see Fig. 1b). Note that the lasing emission band of both FITC and BODIY is much narrower than their respective fluorescence band. Consequently, the lasing emission can be distinguished between FITC and BODIPY, even though their fluorescence cannot be.

Distinct changes in output emission below and above threshold can be better visualized by the CCD images in Fig. 4.3(c). Below the lasing threshold, the emission was spatially featureless throughout the focal spot on the tissue. Above the lasing threshold, the laser output is generally described by Ince–Gaussian modes[133,134]. Due to the quasi-circular symmetry of the myofibrils inside the cavity, the laser emission in Fig. 4.3(c) looks more like the Laguerre-Gaussian modes.

We further investigated how tissue thickness and the concentration of staining FITC affect the lasing characteristics, which is important for future practical use of tissue lasers in biology and biomedicine. Fig. 4.3(d) shows the lasing spectra by varying the muscle tissue thickness with the fixed concentration of FITC used to stain the tissue (2 mM). The respective free spectral range

(FSR) for the cavity length of 20 μm, 30 μm, and 40 μm is 5.3 nm, 3.5 nm, and 2.7 nm, respectively, which give an average effective muscle tissue refractive index of 1.43, close to the reported value of 1.41[135]. Although the number of the lasing modes increases with the increased tissue thickness due to the multimode nature of the FP cavity at current lengths (20 μm – 40 μm), the lasing band still remains around 10 nm. Note that the slight increase in background around 560 nm is caused by the reduced reflectivity of the dielectric mirror of the FP cavity (Fig. 4.2(b)). Fig. 4.3(e) plots the lasing threshold of the tissue laser of various tissue thicknesses, showing the optimal muscle tissue thickness is around 30 μm.

Furthermore, we investigated in Fig. 4.3(f) the dependence of the lasing threshold on the FITC concentration at the fixed tissue thickness (30 μm). The lasing threshold decreased monotonically when the FITC concentration used to stain the tissue increased from 0.25 mM to 2 mM. The overall agreement between the experimental results with the simulation in section 4.4.2 suggests that the concentration of FITC inside the muscle tissue follows the concentration of the FITC in solution outside the tissue at an approximately 1:1 ratio during staining. This appears to be reasonable, as FITC molecules simply migrate into and are subsequently trapped by the tissue matrix non-specifically during staining. However, when the FITC concentration exceeds 2 mM, the threshold begins to rise again, which is due probably to the self-quenching effect of the dye at high concentrations. In fact, the FP laser with pure FITC (in the absence of the muscle tissue) shows the similar threshold decrease when the FITC increases from 0.5 mM to 2 mM and the similar threshold increase when the FITC concentration increases from 2 mM to 3 mM. Details of the lasing spectra and threshold plots of all data points in Figs. 4.3(e) and (f) can be found in Figs. 4.5 and 4.6, respectively.

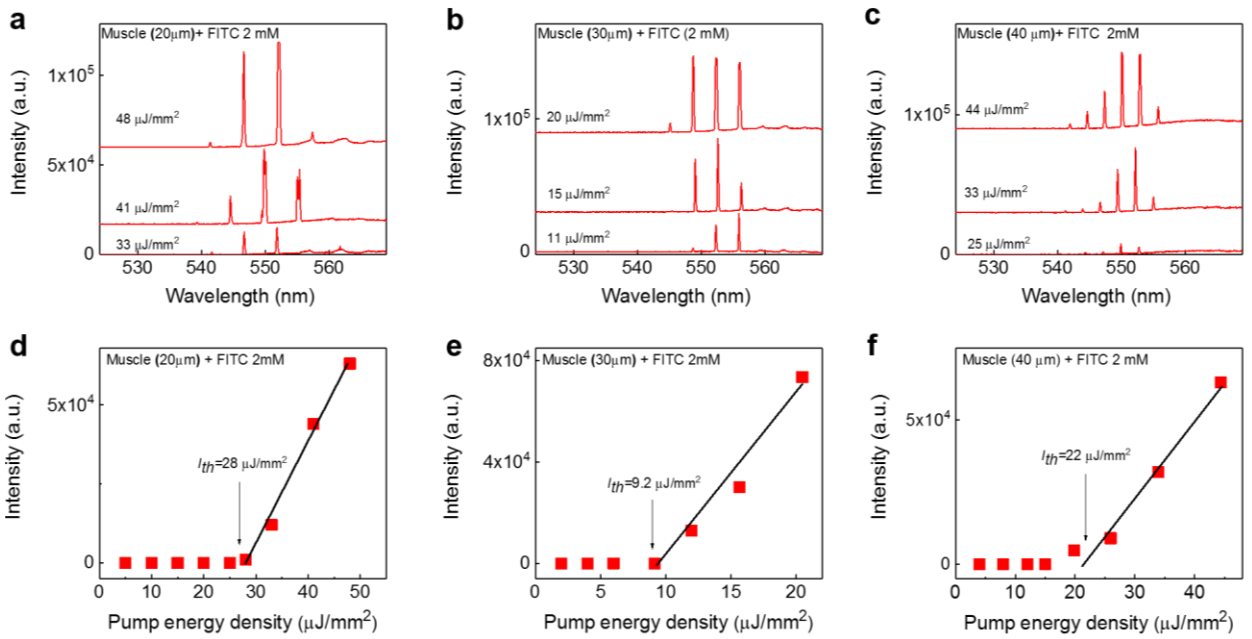

Figure 4.5. Lasing spectra of muscle tissue with different cavity length. (a-c) Lasing spectra of muscle tissue doped with FITC (2 mM) under various pump energy densities by with the cavity length of (**a**) 20 μm, (**b**) 30 μm, and (**c**) 40 μm. All curves are vertically shifted for clarity. (**d-f)** Spectrally integrated (540 nm – 560 nm) laser output as a function of pump energy density extracted from (a), (b), and (c), respectively. Solid lines show the linear fit above the threshold.

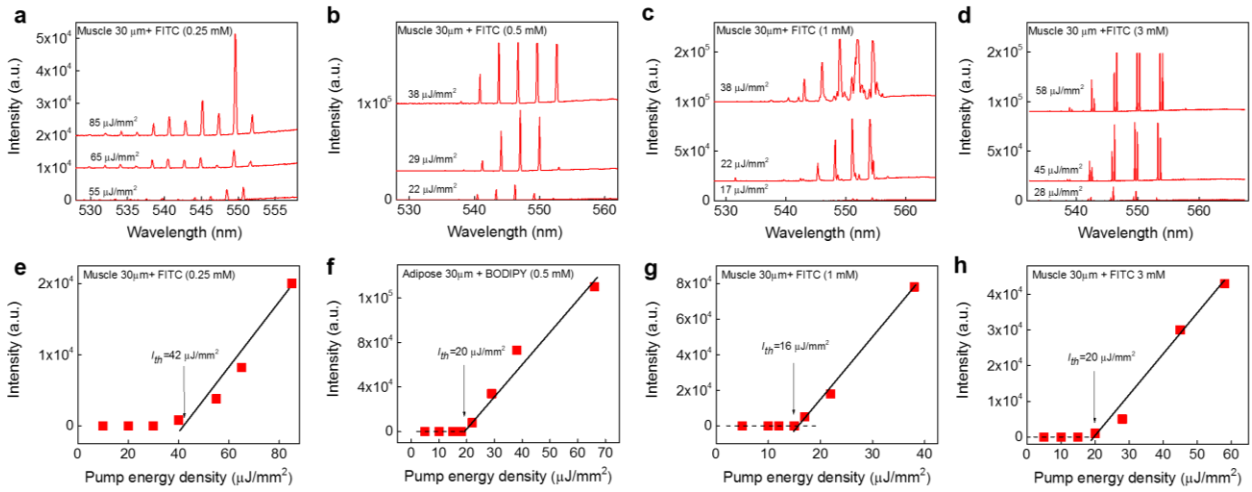

Figure 4.6. Lasing spectra of muscle tissue with different FITC concentration. (a-d) Lasing spectra of muscle tissue doped with FITC (cavity length fixed at 30 μm) under various pump energy densities with FITC concentration of (**a**) 0.25 mM, (**b**) 0.5 mM, (**c**) 1.0 mM, and (**d**) 3.0 mM. All curves are vertically shifted for clarity. (**e-h)** Spectrally integrated (540 nm – 560 nm) laser output as a function of pump energy density extracted from (a), (b), (c), and (d), respectively. Solid lines show the linear fit above the threshold.

In order to comprehensively understand how the tissue geometric structures affect the lasing properties and thresholds, we compared the lasing from the muscle tissue with the myofibrils in the transverse and longitudinal direction (Fig. 4.7(a)). The DIC and confocal fluorescence images of transverse myofibrils stained with FITC are given in Fig. 4.7(b). The tissue sections (30 μm) were cut from the same piece of tissue as in Fig. 4.3 but with different cutting directions and

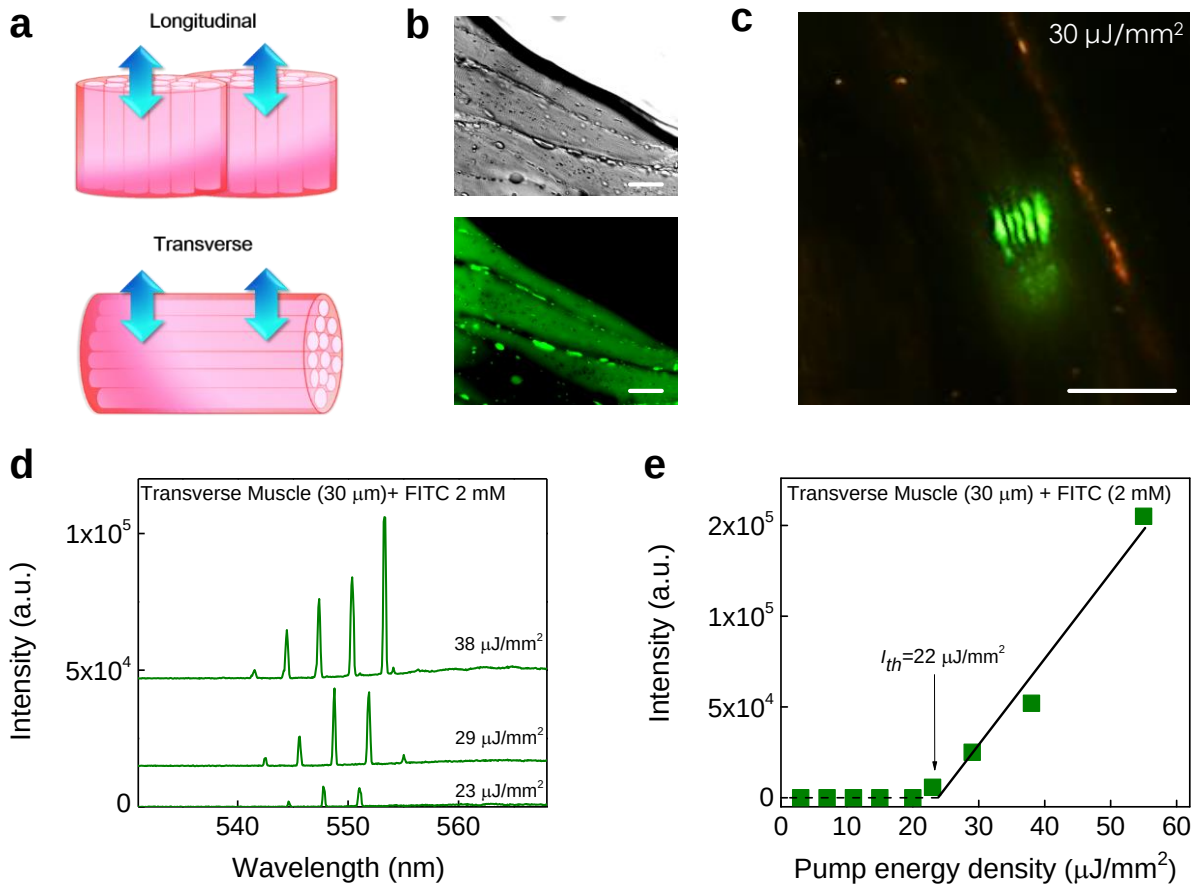

Figure 4.7. Lasing in muscle tissue - transverse myofibrils. (a) Schematic showing the two arrangements of myofibrils (muscle fibers), longitudinal and transverse. Arrows indicate the lasing emission direction. The FP cavity is not shown. (**b)** DIC (upper) and confocal fluorescence microscopic (lower) images of transverse myofibrils stained width FITC. (**c)** CCD images of tissue lasing in transverse myofibrils. (**d)** Examples of lasing spectra of transverse muscle tissue stained with FITC under various pump energy densities. Curves are vertically shifted for clarity. **(e)** Spectrally integrated (540 nm – 560 nm) laser output as a function of pump energy density extracted from (d). Solid line is the linear fit above the threshold, showing a lasing threshold of approximately 22 μJ/mm^2. Tissue thickness=30 μm. [FITC]=2.0 mM. All scale bars, 20 μm.

sandwiched in the same FP cavity. The lasing characteristics of transverse muscles exhibit a remarkable difference from those of longitudinal muscles. First, the spatial pattern of lasing emission (Fig. 4.7(c)) resembles linear Hermite-Gaussian modes due to the myofibril arrangement. Second, the lasing threshold for the transverse muscle is about 22 μJ/mm^2 (Figs. 4.7(d) and (e)), approximately 2-3 times larger than for the longitudinal muscle. The lower lasing threshold in the longitudinal muscle is due to the light-guiding (light confinement) mechanism along the myofribils myofibrils[136,137] (see Fig. 4.8 to visualize the light-guiding effect) and fewer interfaces (myobribril/sarcolemma) that the light encounters when it travels between the two mirrors.

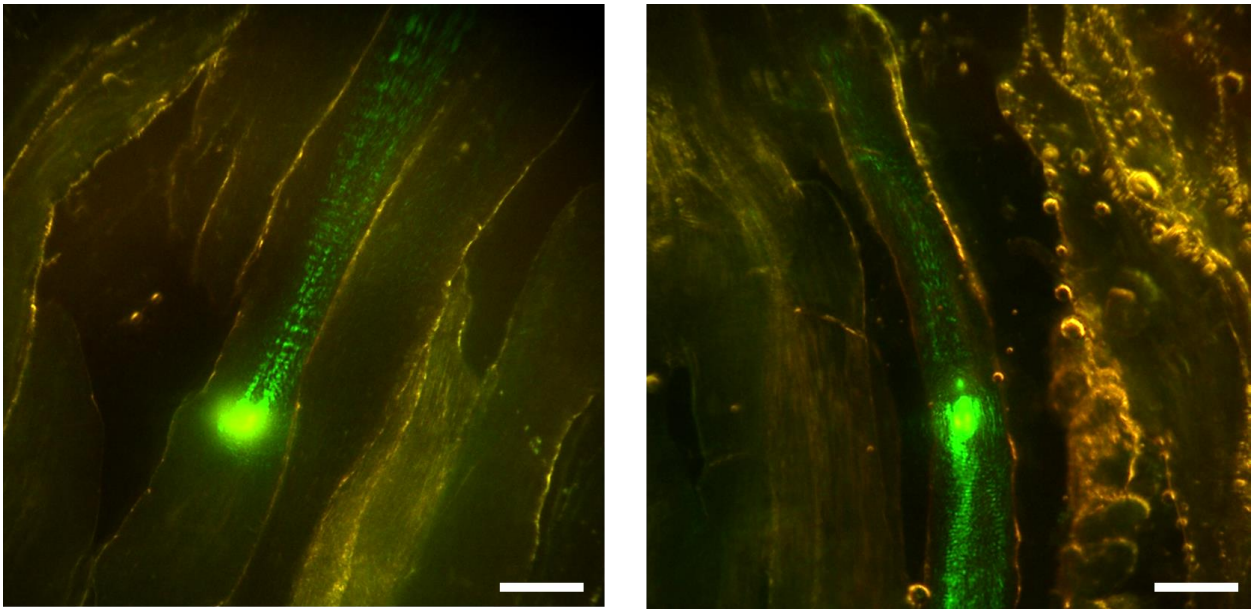

Figure 4.8. Light guiding in myofibrils. Strong light-guiding effect along the myofibrils can be clearly observed under a high pump intensity (72 μJ/mm^2), which shows that that propagation loss is smaller along myofibrils than across myofibrils. Tissue thickness=30 μm. [FITC]=2.0 mM. Excitation wavelength=465 nm. Scale bars, 40 μm.

4.4.2. Simulation analysis

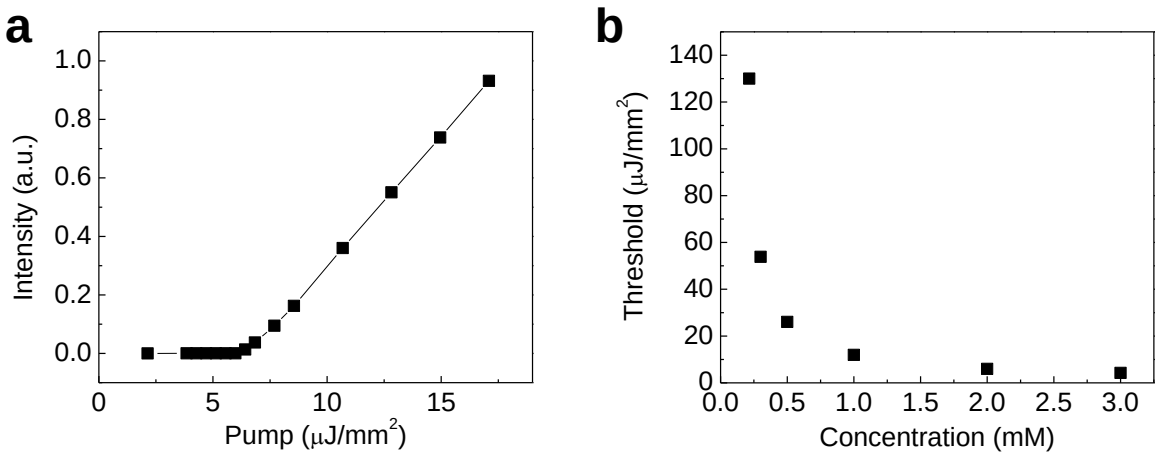

Figure 4.9. Simulation of lasing threshold in muscle. (a) Lasing threshold simulation for the muscle tissue in the longitudinal direction shows a threshold of ~7 μJ/mm^2. FITC= 2 mM. Cavity length=30 μm. Tissue extinction coefficient=10 cm^{-1}. (**b)** Lasing threshold vs. FITC concentration inside the muscle tissue. Other parameters are the same as in (a).

The FITC laser is described by:

$$\frac{d\mathrm{n}(t)}{dt} = I_p(t)\sigma_{a,p}[N_0 - \mathrm{n}(t)] - \frac{\sigma_{e,l}c}{\varepsilon}\mathrm{n}(t)q(t) + \frac{\sigma_{a,l}c}{\varepsilon}[N_0 - \mathrm{n}(t)]q(t) - \frac{n(t)}{\tau_0} \quad (1)$$

$$\frac{dq(t)}{dt} = \frac{Fc}{\varepsilon V}\sigma_{e,l}n(t) + \frac{Fc}{\varepsilon}\sigma_{e,l}n(t)q(t) - \frac{Fc}{\varepsilon}\sigma_{a,l}[N_0 - n(t)]q(t) - \frac{q(t)}{\tau_q} \quad (2)$$

In these equations, n is the concentration of the excited FITC molecules and q is the photon density of a lasing mode at FITC emission band. I_p is the photon fluence at the excitation wavelength (465 nm). $\sigma_{a,p}$ is the absorption cross section of FITC at the excitation wavelength. N_0 is the total concentration of FITC. $\sigma_{a,l}/\sigma_{e,l}$ is the absorption/emission cross section of FITC at the lasing wavelength. c is the speed of light in vacuum. ε is the refractive index of the tissue. τ_f is the fluorescence lifetimes of FITC. τ_q denotes the lifetime of the photon in the lasing mode and is determined by $\tau_q = (\frac{1}{\tau_0} + \frac{1}{\tau_s})^{-1}$, where $\tau_0 = \frac{\lambda Q_0}{2\pi c}$ results from the loss of mirrors (Q_0, empty cavity quality factor; λ, lasing wavelength) and $\tau_s = \frac{\varepsilon}{c\alpha}$ results from the attenuation of light by the

presence of tissue (α, tissue extinction coefficient). With the round trip loss limited by the transmission of the bottom mirror (0.5%), Q_0 of an FP cavity with a cavity length of 30 μm is 1.9e5. The extinction coefficient of tissue, $\alpha = \alpha_s + \alpha_a$, where α_s is scattering loss and α_a is the absorption of myoglobin. Here we only consider the forward scattering since the thickness of the muscle tissue is far less than 1mm. Therefore we can simply use the reduced scattering coefficient of muscle in longitudinal orientation for simulation (scattering loss approximately is 9 cm^{-1} [138,139]). The myoglobin absorption coefficient is 1 cm^{-1}. V is the mode volume and F is the fraction of the mode volume occupied by the tissue. To simulate the pulse excitation condition, we assume the excitation photon fluence I_p to be Gaussian with a full width at half maximum (FWHM) of 5 ns. Pump intensity is determined by temporal integral of I_p from time zero to infinity. The coupled rate equations are numerically solved in Matlab for different conditions. Output intensity is determined by temporal integral of q(t) assuming a constant out-coupled rate. Parameters used in the simulation are summarized in Table 1 below.

Table 1. Simulation parameters

Symbols	Description	Numeric values
$\sigma_{a,p}$	Absorption cross section at excitation wavelength	1.25e-16 cm^2
$\sigma_{a,l}$	Absorption cross section at lasing wavelength	<1e-19 cm^2
$\sigma_{e,l}$	Emission cross section at lasing wavelength	1.19e-16 cm^2
c	Speed of light in vacuum	30 cm/ns
ε	Refractive index of tissue	1.40
τ_f	Fluorescence lifetime of FITC	4.1 ns
V	Volume of the electromagnetic mode	2.7e-8 cm^3
F	Fraction of mode volume occupied by the dye molecules	1
Q_0	Empty cavity quality factor (cavity length=30 μm)	1.9e5
λ	Lasing wavelength	550 nm
α	Tissue extinction coefficient	$\alpha_s + \alpha_a$
α_s	Tissue scattering loss	Longitudinal, 9 cm^{-1}
α_a	Myoglobin absorption loss	1 cm^{-1}

4.4.3. Lasing in adipose tissues

To demonstrate the versatility of our tissue laser platform, in Fig. 4.10 we further studied the lasing properties of brown adipose tissue stained with BODIPY. The lasing spectra of a 30 μm brown adipose tissue stained with 1 mM BODIPY under various pump energy densities is shown in Fig. 4.10(a). Periodic lasing peaks start to emerge around 528 nm and the overall lasing band is approximately 15 nm (520 nm - 535 nm), still much narrower than the corresponding fluorescence band. Due to the absence of myoglobin the lasing band of the adipose tissue is red-shifted only 10 nm with respect to that from pure BODIPY lasing (see Fig. 4.4), much smaller than the 30 nm red-shift observed for the muscle laser discussed previously. The spectrally integrated laser emission versus pump energy density presented in Fig. 4.10(b) shows the lasing threshold of approximately 20 $\mu J/mm^2$. Prominent changes in output emission below and above threshold were obtained through the CCD images in Fig. 4.10(c). Below the lasing threshold (15 $\mu J/mm^2$), the emissions was spatially featureless throughout the focal spot on the tissue. Above the lasing threshold (31 $\mu J/mm^2$), the spatial output exhibits more irregular patterns than that for the muscle tissues arranged longitudinally or transversely, because of various sizes of lipid droplets randomly distributed within the focal point of the pump light.

The effect of tissue thickness and BODIPY concentration on the lasing characteristics were also studied. Fig. 4.10(d) shows the lasing spectra of various tissue thicknesses with the fixed BODIPY concentration at 1 mM. The measured FSR for the cavity length of 20 μm, 30 μm, and 40 μm is 4.5 nm, 2.9 nm, and 2.2 nm, respectively, which result in an average effective tissue refractive index of 1.55, close to the reported value of 1.48[135,140]. The lasing threshold for various tissue thicknesses is shown in Fig. 4.10(e), showing the optimal tissue thickness of about 30 μm, similar to that for the muscle tissue. Fig. 4.10(f) shows the dependence of the lasing threshold on

the BODIPY concentration at a fixed adipose tissue thickness. The lasing threshold decreased gradually between 0.5 mM to 2 mM. However, due to the self-quenching effect of BODIPY, the lasing threshold rises when the concentration exceeds 2 mM, which is also similar to what we observed for the muscle tissue with FITC. Details of the lasing spectra and threshold plots of all data points in Figs. 4.10(e) and (f) can be found in Figs. 4.11 and 4.12, respectively.

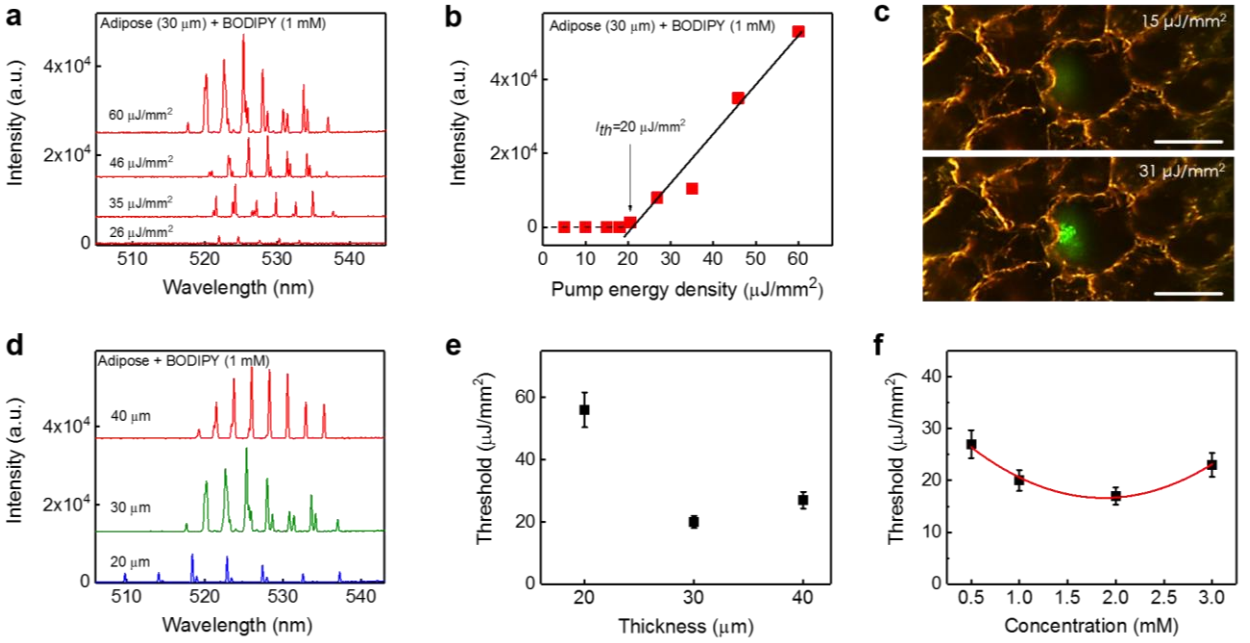

Figure 4.10. Lasing in adipose tissue. (a) Examples of lasing spectra of adipose tissue (30 μm) stained with BODIPY (1.0 mM) under various pump energy densities. Curves are vertically shifted for clarity. **(b)** Spectrally integrated (520 nm – 535 nm) laser output as a function of pump energy density extracted from the spectra in **a**. The solid lines are the linear fit above the lasing threshold, which is approximately 20.0 μJ/mm^2. **(c)** CCD images of the muscle tissue laser output below (15 μJ/mm^2) and above (31 μJ/mm^2) the lasing threshold. The image shows clear boundaries of several adipocytes, in which the laser beam is focused on only one of the fat cells. Scale bars, 20 μm. **(d)** Lasing spectra of adipose tissues of different thicknesses above the lasing threshold. **(e)** Laser threshold for different tissue thicknesses. The concentration of BODIPY used to stain the tissue was 1.0 mM. Error bars were based on three individual measurements at different sites. **(f)** Laser threshold with different concentrations of BODIPY used to stain the tissue at the fixed tissue thickness (and hence the cavity length) of 30 μm. The solid curve is a quadratic fit to guide an eye. Error bars were based on three individual measurements at different sites.

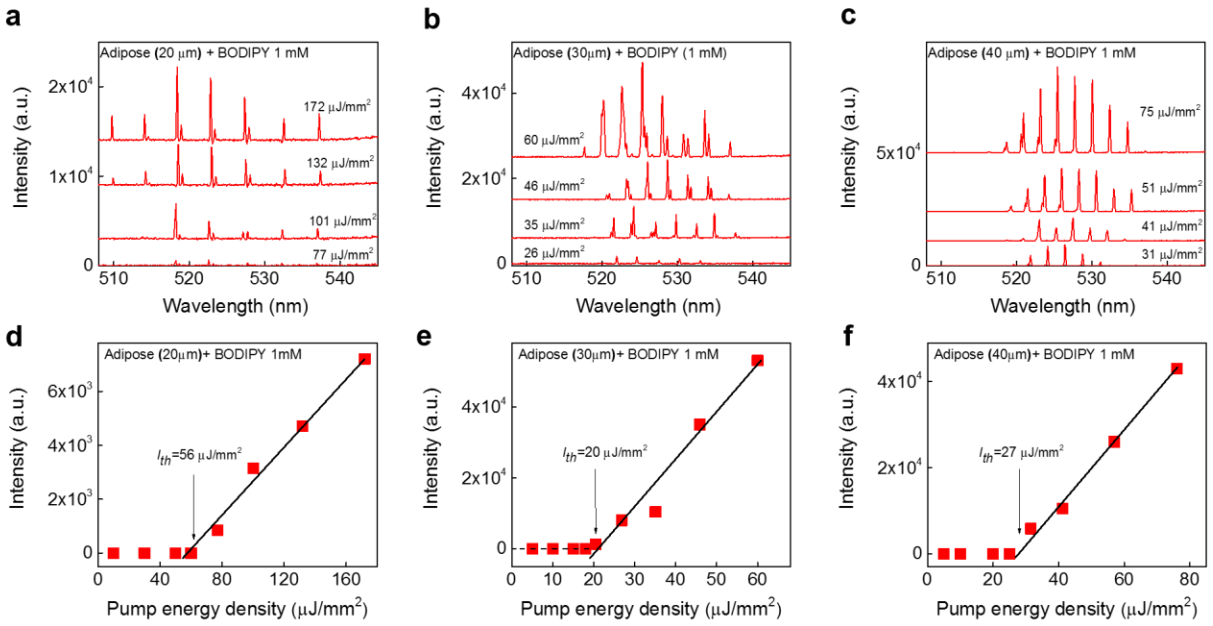

Figure 4.11. Lasing spectra of adipose tissue with different cavity length. (**a-c)** Lasing spectra of adipose tissue doped with BODIPY (1.0 mM) under various pump energy densities with the cavity length of (**a**) 20 μm, (**b**) 30 μm, and (**c**) 40 μm. All curves are vertically shifted for clarity. (**d-f**) Spectrally integrated (515 nm – 535 nm) laser output as a function of pump energy density extracted from (a), (b), and (c), respectively. Solid lines show the linear fit above the threshold.

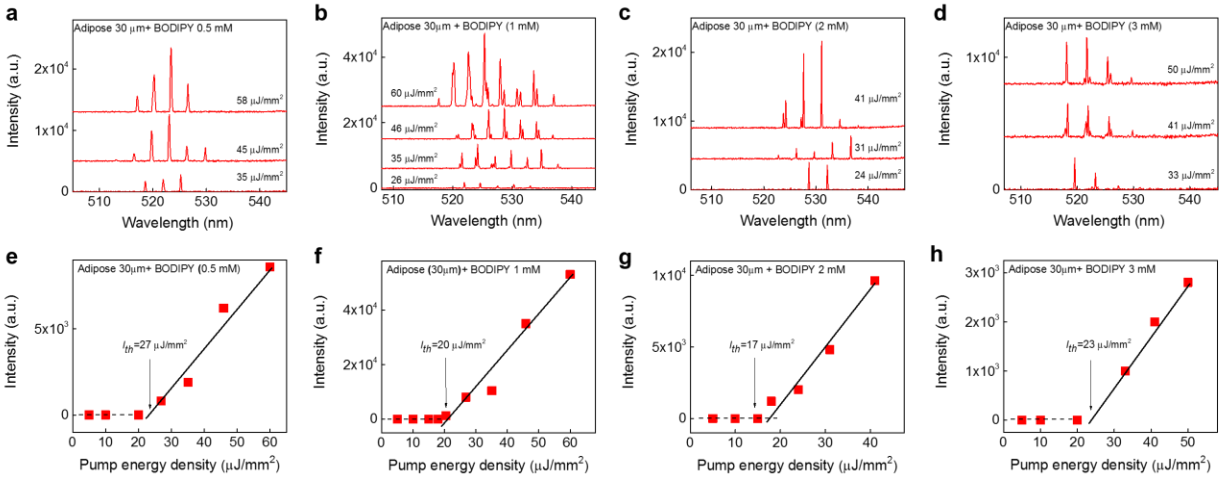

Figure 4.12. Lasing spectra of adipose tissue with different BODIPY concentration. (**a-d)** Lasing spectra of adipose tissue doped with BODIPY (cavity fixed at 30 μm) under various pump energy densities with BODIPY concentration of (**a**) 0.5 mM, (**b**) 1.0 mM, (**c**) 2.0 mM, and (**d**) 3.0 mM. All curves are vertically shifted for clarity. (**e-h)** Spectrally integrated (515 nm – 535 nm) laser output as a function of pump energy density extracted from (a), (b), (c), and (d), respectively. Solid lines show the linear fit above the threshold.

4.4.4. Multiplexed lasing in tissues

After studying individual dyes with individual types of tissues, we further achieved selective and multiplexed lasing from a hybrid tissue (Fig. 4.13(a)), which allows us to generate lasing signals from myocytes and adipocytes on the same piece of tissue. The tissue was dual-stained, *i.e*., FITC was used to bind mostly proteins (myocytes) and BODIPY to lipids (adipocytes). DIC and confocal microscopic images were used to confirm the dual staining process in tissue (Figs. 4.13(b) and (c)). By tuning the pump light focal position, we were able to achieve lasing emission by scanning along the tissue in one direction, as shown in the dotted lines in Figs. 4.13(b) and (c). Here we chose 3 sites to represent two different tissues: site 1 (muscle tissue with 2 mM FITC), site 2 (adipose tissue with 1 mM BODIPY), and site 3 (muscle tissue with 2 mM FITC). Fig. 4.13(d) shows the conventional fluorescence spectra measured at site 1, 2, and 3 (in the absence of the FP cavity by removing the top mirror). Apparently, we would not be able to distinguish the tissue type among these three sites by their fluorescence, thanks to the huge spectral overlap between FITC and BODIPY. In contrast, by placing the same tissue in the FP cavity (by putting the top mirror back), lasing signals (and hence the tissue type) of these three sites can be distinguished in Figs. 4.13(e) and (f). Fig. 4.13(e) shows the selective lasing emission from only one type of tissue (and dye). In this case, the pump energy density (20 $\mu J/mm^2$) was set between the threshold for FITC and BODIPY. Only lasing signals from FITC (site 1 and site 3) were generated. No laser signals could be detected from BODIPY (site 2). Since the mirror blocks significant amount of fluorescence background and allows only the laser emission to pass, an extremely high contrast ratio ($\sim 10^3$) between site 1 and 2 can be achieved. For comparison, the contrast of fluorescence between site 1 and site 2 is nearly unity (see Fig. 4.13(d)). Fig. 4.13(f) demonstrates the multiplexed lasing emission from multiple dyes. In this case, a higher pump

energy density (60 μJ/mm^2) was used to obtain the lasing emission from both FITC and BODIPY. Despite strong spectral overlap in fluorescence, the lasing spectra from FITC and BODIPY are vastly different spectrally, thus allowing for clear differentiation between muscular and adipose

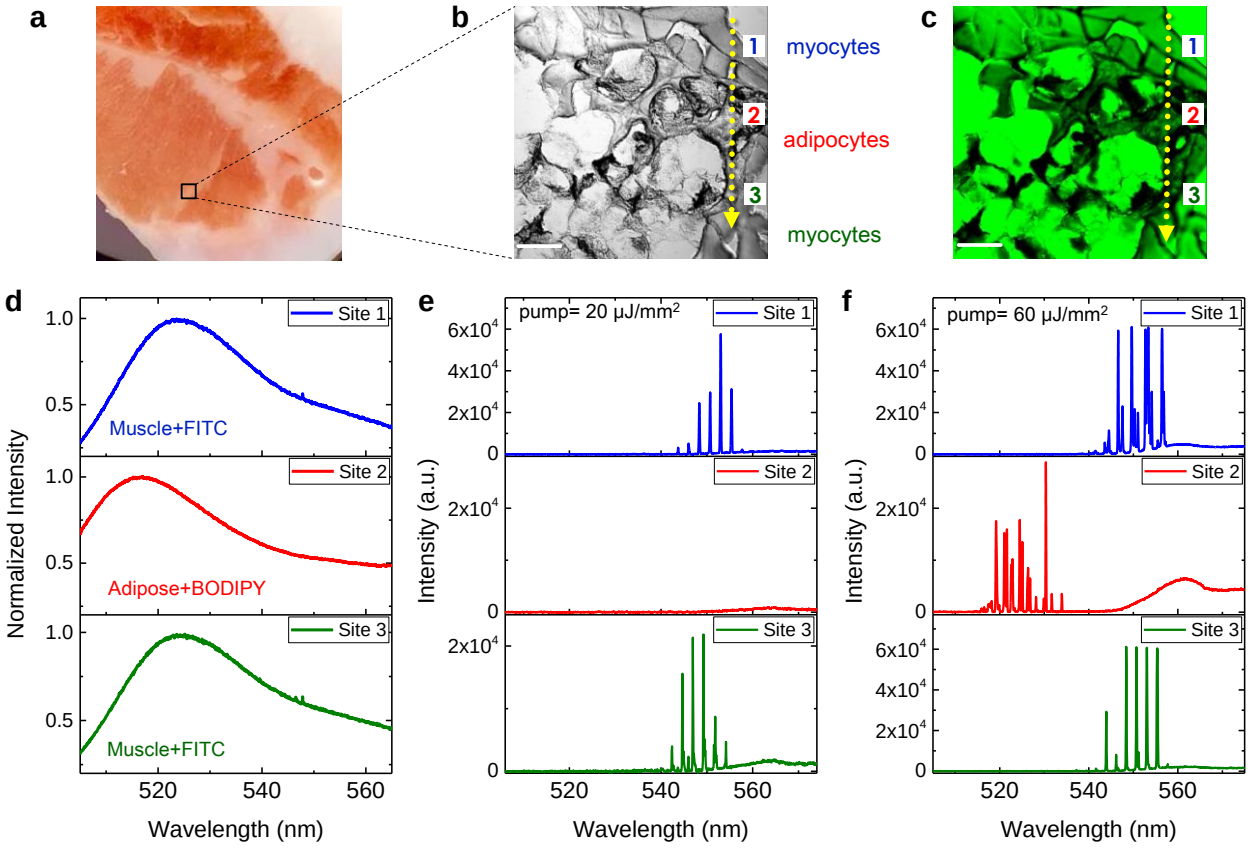

Figure 4.13. Multiplexed lasing in hybrid tissue. (a) A photo of the piece of hybrid tissue used in this experiment. The labeled black squared is the region of interest where muscle tissues and adipose tissues are unable to distinguish directly by its appearance. **(b)** DIC image of the hybrid tissue labeled in (a) containing an irregular mixture of adipose tissues and muscle tissues. Three representative sites were taken on (site 1) muscle tissue, (site 2) adipose tissue, and (site 3) muscle tissue, respectively, as the pump laser beam scanned through one direction (see the dashed arrows). **(c)** Confocal image of the hybrid tissue dual-stained with FITC and BODIPY. **(d)** Fluorescence spectra of muscle tissue with FITC (site 1), adipose tissue with BODIPY (site 2), and muscle tissue with FITC (site 3). **(e)** Lasing spectra taken at site 1, 2, and 3, respectively, when the pump energy density was set between the threshold for muscle tissue and for adipose tissue (20 μJ/mm^2). **(f)** Lasing spectra taken at site 1, 2, and 3, respectively, when the pump energy density was above the threshold for both muscle tissue and adipose tissue (60 μJ/mm^2). Note that the increase in the background emission spectra around 560 nm in (e) and (f) is due to the fluorescence leaking out of the FP cavity caused by the reduced reflectivity of the dielectric mirror. Scale bars in (b) and (c), 40 μm.

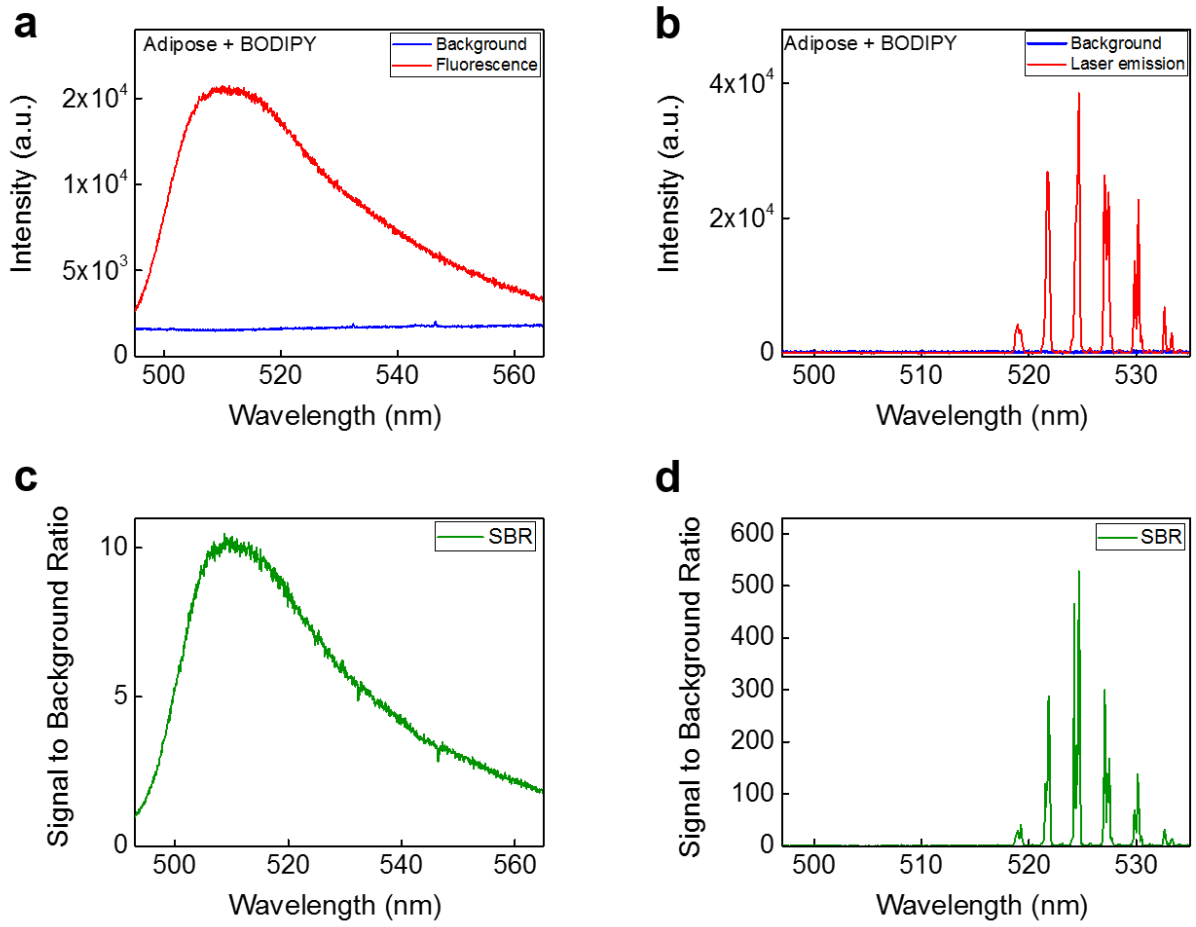

Figure 4.14. Signal to background ratio of fluorescence and laser emission in tissue. Comparison of the signal to background ratio (SBR) between fluorescence and lasing emission. (**a)** Fluorescence spectrum of adipose tissue stained with BODIPY (red) and its background (blue). (**b)** Lasing spectrum of adipose tissue stained with BODIPY and its background (blue). (**c)** SBR extracted from (a) showing the maximal value of about 10. (**d)** SBR extracted from (b) showing the maximal value of about 500. All the background signals were measured using the tissue sites without staining under the same configuration. [BODIPY]=1.0 mM. Pump energy density=60 μJ/mm^2. Excitation wavelength=465 nm. Fluorescence was measured by removing the top mirror.

tissues. The above two examples attest to the ability of the tissue laser to control and distinguish lasing signals in the presence of multiple dyes. Such ability arises from the sensitive dependence of the laser characteristics (such as lasing wavelength and threshold, as well as output intensity and polarization) on the emission/absorption properties of dyes and their biochemical and physical environment (such as tissue scattering/absorption and binding affinity of dyes to particular markers

on tissue, *etc*.), which enables highly multiplexed analysis of tissues using various fluorophores. In addition to spectrally resolving two very similar dyes, the tissue laser provides another benefit, *i.e*., high SBR. As exemplified in Fig. 4.14, the SBR in the tissue laser is 500, about 50-fold improvement over conventional fluorescence based detection. Note that since the random laser does not have a mirror[41,42,116-118], strong fluorescence or scattering background will still be detected without being blocked, thus significantly reducing the SBR.

4.4.5. Lasing with specific conjugates and mirrors

In many applications, fluorophores are conjugated to biochemical molecules in order to specifically bind to the target in a tissue. To demonstrate that the tissue lasing technique can be applied to fluorophore-conjugates, in Fig. 4.15 we employed FITC-phalloidin as a model system, which has high affinity for F-actin in muscle tissues[141]. In this experiment, lasing could be achieved by using only 10 μM FITC-phalliodin to stain the muscle tissue (Fig. 4.15(a)). In comparison with non-specific binding of FITC (Fig. 4.1(f)), the specific binding of FITC-phalloidin to F-actin resulted in localized fluorescence near cell membranes under confocal microscopy (Fig. 4.15(c)) and made the FITC concentration in the muscle tissue much higher than the original staining FITC-phalloidin concentration (10 μM). Consequently, lasing from FITC could be achieved with a threshold about 130 μJ/mm^2 (Fig. 4.15(b)), while no lasing was observed with non-specific FITC in muscle tissue even at 300 μJ/mm^2 under the same conditions and using the same staining FITC concentration (10 μM). Based on our simulation in Fig. 4.9(b), the effective FITC-phalloidin concentration inside the tissue is estimated to be ~200 μM. In Fig. 4.15(d), the spatial distribution of the laser profiles suggests that the lasing is a generalized higher order Ince-Gaussian mode.

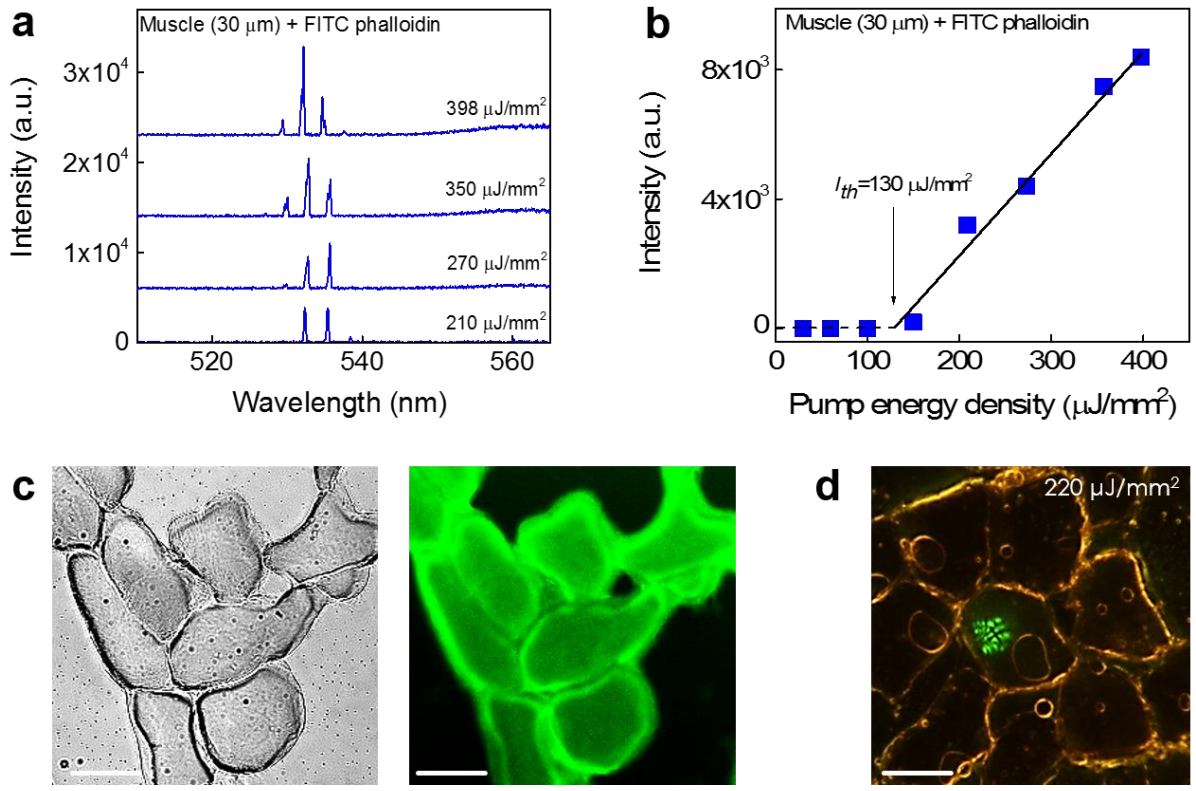

Figure 4.15. Lasing in muscle tissue with FITC conjugates. (a) Examples of lasing spectra of the muscle tissue stained with FITC-phalloidin under various pump energy densities. The lasing is centered around 535 nm. This blue shift with respect to the lasing emission around 550 nm for 1 mM FITC is typical for a laser when the gain medium concentration decreases[52,67]. **(b)** Spectrally integrated (530 nm – 545 nm) laser output as a function of pump energy density extracted from (a). Solid line is the linear fit above the threshold, which is approximately 130 μJ/mm^2. **(c)** Confocal fluorescence image of the muscle tissue stained with FITC-phalloidin. The muscle was arranged longitudinally. **(d)** CCD images of lasing emission above the lasing threshold. All scale bars, 20 μm. Tissue thickness=30 μm. [FITC-phalloidin]=10 μM. Excitation wavelength=465 nm.

In all the experiments presented so far, we used the plano-plano (p-p) FP cavity, which is well known to be unstable and susceptible to Q-factor degradation even with slight misalignment[106,142], and might also have contributed to the variations in the lasing threshold for different tissue thicknesses in Fig. 4.3(e). Such Q-factor degradation is less significant in the case of single-cell lasers due to the lensing effect of the cell[37]. Unfortunately, this lensing effect may not exist for tissue lasers when cells are embedded in the extracellular matrix. In contrast, plano-

concave (p-c) FP cavities are highly stable and the high Q-factor can be maintained even with misalignment during assembly of the FP tissue laser. As a proof of concept, we created an array of micron-sized concave mirrors (3 mm apart between two adjacent concave mirrors) using CO_2 laser ablation on the same top mirror[106] (see Fig. 4.2) and tested with the same FITC stained muscle tissue. The Q-factor of those p-c FP cavities exceeded 10^5, according to our previous work[106]. As shown in Fig. 4.16, a lasing threshold of approximately 2 μJ/mm^2 was achieved, ~10 times lower than the corresponding p-p FP cavity in Fig. 4.3 and about 100 times lower than the random tissue laser (90-380 μJ/mm^2)[41,42,115]. Currently, our top mirror design does not allow us to scan the concave mirror. In the future, a high-Q scanning concave mirror can be created on the tip of an optical fiber[143,144] to examine the entire tissue.

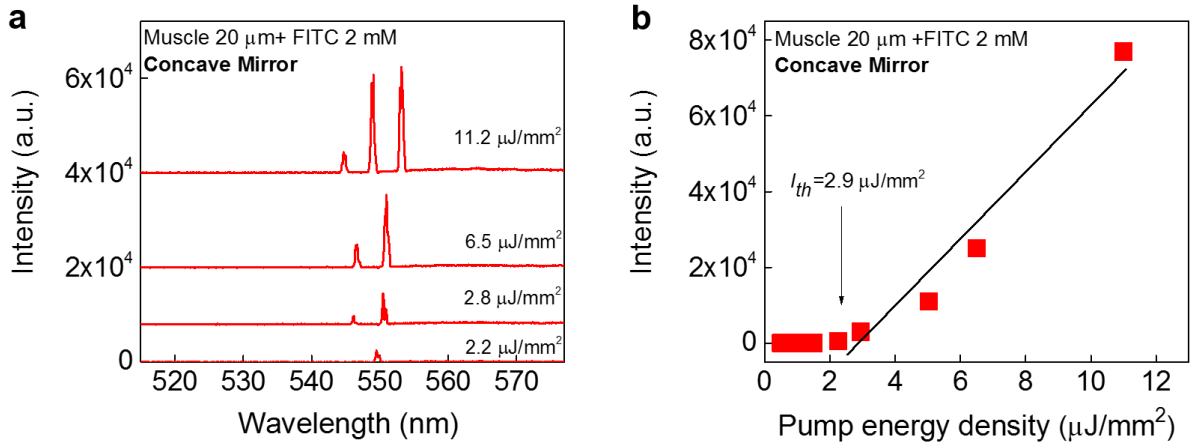

Figure 4.16. Lasing in tissue with concave FP cavity. (**a)** Examples of lasing spectra of muscle tissue stained with FITC using a concave top mirror under various pump energy densities. (**b)** Spectrally integrated (540 nm – 560 nm) laser output as a function of pump energy density extracted from (a). Solid line is the linear fit above the threshold, showing a lasing threshold of approximately 2 μJ/mm^2. Tissue thickness=20 μm. [FITC]=2.0 mM. Excitation wavelength=465 nm.

4.5. Conclusion

In this work, we have studied and developed a highly versatile tissue laser platform based on a high-Q FP cavity. Although only two dyes and two types of tissues were demonstrated in the current studies, there is no doubt that the tissue laser platform can readily be translated to other fluorophores (such as quantum dots[145] and fluorescent proteins) and other types of tissues. Such a tissue laser offers narrow spectral bandwidth, strong emission intensity, and large background rejection, which, coupled with the positive feedback provided by the laser cavity, can significantly improve the sensitivity, specificity, multiplexibility, and imaging contrast in tissue characterization. Besides emission intensity, the laser output from tissues consist of a number of unconventional parameters that can be monitored and serve as the sensing signal, such as lasing threshold, lasing efficiency, and lasing mode spatial distribution. Collectively, the multi-parameter analysis would enable better understanding of intratissue/intertissue biological activities and structures.

In the near future, a few research directions will be explored towards eventual practical use of the tissue laser. First, integration with an imaging spectrometer will be implemented for advanced tissue mapping with higher spectral and spatial information. Secondly, fluorophores conjugated with antibodies can be used to target multiple biomarkers in tissues. We envision that our tissue laser will provide a novel spectroscopic tool for a plethora of applications ranging from medical diagnostics and preclinical drug testing to monitoring and identification of biological transformations in tissue engineering.

Chapter 5

Mapping Nuclear Biomarkers with Laser Emissions for Cancer Diagnostics

Based on the development of "versatile tissue lasers" in Chapter 4, here in Chapter 5 we aim to translate such concept into clinical applications. Besides lasing with common non-site-specific dyes, the ability to detect biomarkers with lasing method will be particularly significant. In particular, nuclear biomarkers such as nucleic acids and nuclear proteins is critical for early-stage cancer diagnosis and prognosis. Conventional methods relying on morphological assessment of cell nuclei in histopathology slides may be subjective, whereas colorimetric immunohistochemical and fluorescence-based imaging are limited by strong light absorption, broad-emission bands and low contrast. Here, we describe the development and use of a scanning laser-emission-based microscope that maps lasing emissions from nuclear biomarkers in human tissues. 41 tissue samples from 35 patients labelled with site-specific and biomarker-specific antibody-conjugated dyes were sandwiched in a Fabry-Pérot microcavity while an excitation laser beam built a laser-emission image. We observed multiple sub-cellular lasing emissions from cancer cell nuclei, with a threshold of tens of $\mu J/mm^2$, sub-micron resolution, and a lasing band in the few-nanometre range. Different lasing thresholds of nuclei in cancer and normal tissues enabled the identification and multiplexed detection of nuclear proteomic biomarkers, with a high sensitivity for early-stage cancer diagnosis.

5.1. Introduction

Nucleus lies in the heart of every cell and carries abundance of nuclear proteins and the majority of cell's genetic materials. Molecular changes in the levels of nucleic acids and chromatin and altered expression patterns of nuclear-matrix proteins are highly relevant to malignant progression[146]. Recent studies have found that a higher level of nucleic acids (aggregates of chromatins) are present in various cancers[146-149], indicating the potential use of nucleic acids for cancer screening and monitoring. In addition, overexpression of specific protein biomarkers, such as epidermal growth factor receptor (EGFR)[150-152], cellular tumor antigen p53[153], cell regulator protein Bcl-2[154], and cell division cycle protein CDK-1[155], in cell nuclei, is of particular prognostic significance[156], as they are highly correlated with patients' survival rate and their response to chemotherapy and radiotherapy in many types of cancers (e.g., lung cancer[151], triple-negative breast cancer[157], colorectal cancer[158], ameloblastoma[159], ovarian cancer[160], gastric cancer and colorectal cancers[154,161]). Detection and evaluation of those nuclear biomarkers (nucleic acids, genetics, and proteins) in human tissues will not only help scientists better understand the signaling pathway in cancers, but more importantly, provide critical information for early stage cancer diagnosis, prognosis, malignant transformation, and the efficacy of anticancer therapies[124,162-165].

To date, evaluation of microscopic histopathology slides by pathologists still remains as the golden standard for cancer diagnosis, which is based mainly on the morphological assessment of cell nuclei in tissues using the Hematoxylin and Eosin (H&E) staining[166,167]. However, due to the lack of quantitative analysis capability, this method is highly subjective and even the best-characterized histopathological features receive only modest agreement among experienced pathologists, which may result in misdiagnosis and poor treatment management[168]. This issue becomes particularly serious and challenging when we deal with very early stage cancers[169].

Meanwhile, for cancer prognosis and guided therapy, immunohistochemistry (IHC) is widely used to analyze specific antigens, especially those prognostic and predicative biomarkers[170,171]. IHC relies on colorimetric detection to identify the location of a given proteomic biomarker within a tissue. While simple, IHC performs poorly in distinguishing biomarkers in nuclei from their surrounding background due to the nonlinear optical effect and low dynamic range[165] (example given in Fig. 5.1). Consequently, the cells having overexpressed nuclear proteomic biomarkers may be misdiagnosed. This problem exacerbates when multiple targets in a nucleus are to be analyzed. Compared to colorimetric detection, immunofluorescence (IF) uses different fluorescent labels to tag different biomarkers, thus resulting in improved contrast and multiplexing capability over IHC[123,124]. However, despite elevated biomarker concentrations in the nuclei for the cancers at an advanced stage, the fluorescence signals from the nuclear biomarkers are oftentimes embedded in a large patch of background fluorescence from cytoplasm that may also have the expression of the same biomarkers (Fig. 5.1). In addition, IF suffers significantly from the broad emission spectra of fluorophores, which poses yet another hurdle to distinguish the biomarkers from nearby features with similar emission wavelengths. Therefore, it becomes challenging to accurately identify the nuclei having biomarker expression and further precisely pinpoint the exact biomarker locations inside the nuclei, which may cause significant distortion in and subsequent misinterpretation of the cancer tissue characterization[172].

In comparison with fluorescence-based detection, laser emission has narrow linewidth, threshold behavior, high intensity, and high sensitivity to biomolecular/cellular changes [6,15,27,30,35-39,52,87,113,115,173,174]. Therefore, biolasers may provide a new bioanalytical tool that complements traditional fluorescence techniques. In one of the biolaser embodiments, bio-species (such as biomolecules, cells, and tissues) are placed inside a Fabry-Pérot (FP) cavity and the laser

characteristics such as lasing wavelength, threshold and intensity are modulated passively (i.e., bio-species are not labeled and the gain media are outside those bio-species)[38,39,173] or actively (i.e., bio-species are labeled with fluorophores that serve as the laser gain media)[29,35,114]. However, to date, no studies have been carried out to use biolasers to identify and detect specific biomarkers within cells/tissues, in particular, using actual patients' samples. Whether biolasers can truly provide new bioanalytical capability remains a question that has yet to answer.

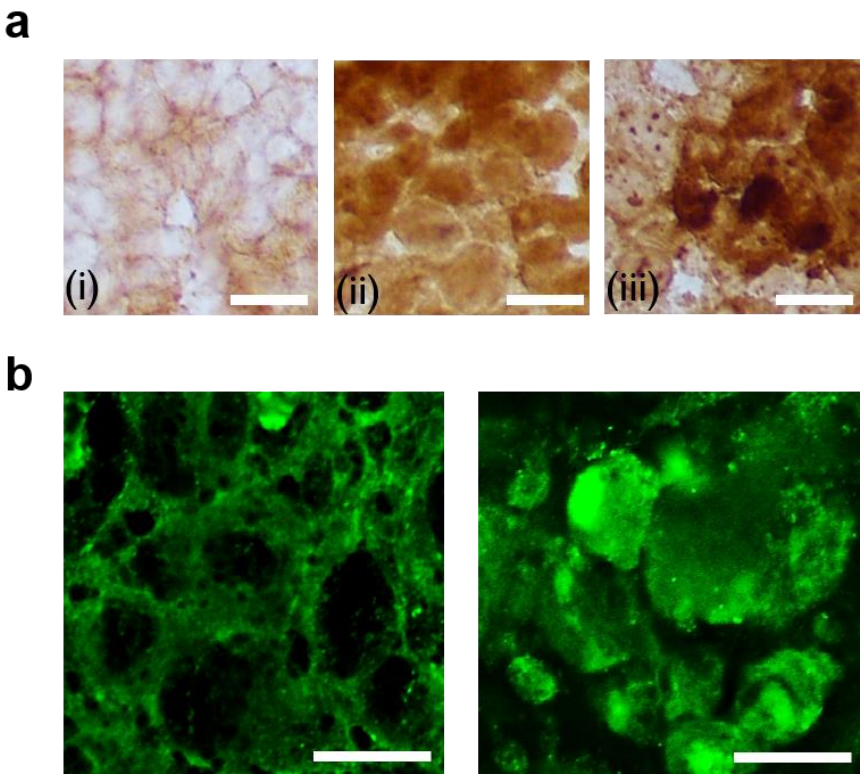

Figure 5.1. IHC and IF images of nuclear EGFR. (a) IHC images of human lung adenocarcinoma tissues having different levels of n-EGFR expression. (i) Tissue without n-EGFR; (ii) Tissue with moderate n-EGFR expression; (iii) Tissue with severe n-EGFR expression. Both the cells with n-EGFR in (ii) and (iii) appear darkish and thus becomes difficult to distinguish between the EGFR expression within the nuclei and in the cytoplasm. **(b)** Confocal immunofluorescence (IF) microscopic images of human lung adenocarcinoma tissues with (right image) and without (left image) n-EGFR expression. In the right image, although the contrast against EGFR in the surrounding cytoplasm is enhanced, the details inside each nucleus still cannot be well characterized. All tissues were first stained with anti-human EGFR antibody, followed by HRP-conjugated anti-Rb IgG antibody with DAB substrate for (a) and FITC-conjugated anti-Rb IgG antibody for (b) (see Methods for details). All scale bars, 20 μm.

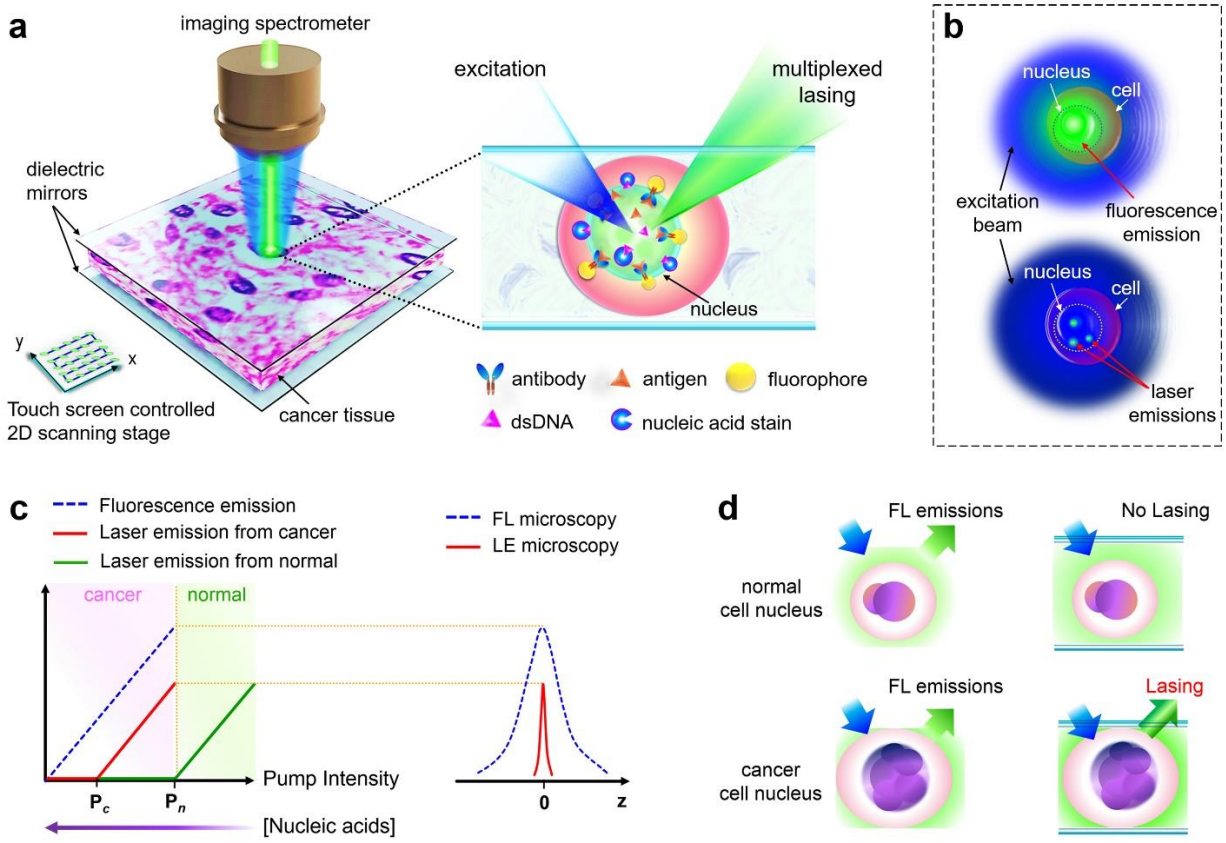

Figure 5.2. Conceptual illustration of the laser-emission based microscope. **(a)** Illustration of the laser-emission based microscope (LEM) configuration when a human cancer tissue is sandwiched within a high-Q Fabry-Pérot cavity and integrated with a 2D raster scanning stage. The laser emission from fluorophores is achieved upon external excitation. The inset shows the details of using nucleic acid staining dyes and antibody-conjugated dyes to achieve multiplexed laser emissions from a tissue. Laser emissions are achieved only when probes are bound to the nucleus or targeted nuclear biomarker within the tissue. Here only one antibody is plotted for example; however, multiple targeted antibodies/fluorophores can be used. **(b)** Comparison between the traditional fluorescence emission (top) and "star-like" laser emission (bottom) from a single nucleus. **(c)** (Left) Output intensity of laser emission as a function of pump intensity. $\mathbf{P}_c$, lasing threshold of cancer cell lasing; $\mathbf{P}_n$, lasing threshold of normal cell lasing. A higher/lower nucleic acid concentration leads to a lower/higher lasing threshold. (Right) Laser emission (red solid line) has a much narrower emission profile than traditional fluorescence (blue dashed line) **(d)** Fluorescence emission is detected in both normal and cancer cell nuclei, whereas laser emission can be detected only in cancer cell nuclei when pump energy density is set between $\mathbf{P}_c$ and $\mathbf{P}_n$.

In this chapter we proposed a scanning "laser-emission-based microscope" (LEM) for improved tumor tissue characterization based on the earlier devolvement of the tissue laser platform[29]. Successful mapping of the lasing emissions from nuclear biomarkers (such as nucleic acids and/or specific antigens) were achieved in human tissues with a sub-cellular and sub-micron resolution (<700 nm) and a lasing threshold on the order of tens of $\mu J/mm^2$. Fig. 5.2(a) illustrates the concept of the LEM, in which a tissue labeled with site specific fluorophores (e.g., nucleic acid probes) and/or antibody-conjugated fluorophores is sandwiched inside an FP microcavity formed by two mirrors. The fluorophores serve as the laser gain medium, which are designed to respond to intracellular binding and intratissue activities, thus generating the sensing signal in the form of laser emission. A 2D scanning stage was integrated to map the tissue and construct images by scanning the pump beam across the whole tissue. As illustrated in Fig. 5.2(b), while fluorescence (top illustration) from a nucleus usually provides "spatially-blurred" signal, which covers a large area with a low spatial resolution and a low contrast between the sites with high and low biomarker expressions, laser emission (bottom illustration) offers distinct advantages due to its high intensity/sensitivity[6,27,36,113], high fluorescence background suppression (for high contrast imaging)[29,30], high spatial resolution[6,28], high spectral resolution (for highly multiplexed detection), and unique threshold behavior (to selectively switch on/off specific laser emission signals (Figs. 5.2(c) and 5.2(d))[18].

In particular, lasing with lung and colon cancer tissues was demonstrated with a total of 41 samples from 35 patients' biopsies (N=41 and >100 tissue sections) involved. Nucleic acid dye, YO-PRO-1 Iodide (YOPRO), and several antibodies (*e.g.*, anti-EGFR, mutant-p53, and Bcl-2) conjugated with fluorescein isothiocyanate (FITC) were used to analyze nucleic acids and the proteomic biomarkers within the nuclei, respectively. We demonstrated that the LEM is able to

not only clearly distinguish between cancer and normal tissues, but diagnose early stage lung cancer tissues with a high sensitivity of 97.5%. Tumor tissues with and without nuclear proteomic biomarkers can be quantified due to vastly different lasing thresholds resulting from different nuclear expressions of biomarkers. Furthermore, we showed the wavelength-multiplexed immuno-lasing capability of the LEM. Dual lasing emissions were achieved to signify the co-localization of nucleic acid and nuclear proteomic biomarkers. We envision that this study will provide an imaging tool complementary to H&E, IHC and IF for better cancer diagnosis and prognosis, as well as to improve the basic understanding of fundamental cell biology.

5.2. Experimental setup of laser-emission microscope

Fabry-Pérot microcavity

The FP microcavity was formed by two customized dielectric mirrors (Fig. 5.3). The top mirror (made by Qingdao Novel Beam Technology Co. Ltd, China) had a high reflectivity in the spectral range of 520 nm - 555 nm to provide optical feedback and high transmission around 465 nm for the pump light to pass through, whereas the bottom mirror (made by Evaporated Coating INC, USA) had a slightly wider reflection band. The respective reflectivity for the top mirror and bottom mirror at the lasing wavelength (535-555 nm) is approximately 99.8% and 99.9%, while the transmission of the top mirror at pump wavelength (465 nm) is ~ 90.2%. The Q-factor for the FP cavity was on the order of 10^4, at a cavity length of 15 μm (without tissues). Details of the fabrication and characterization of the FP cavities are described in the reference[8].

Laser emission microscope (LEM) system

The bright field IHC images were taken with a Nikon-E800 Wide field Microscope. The confocal fluorescence microscopic images were taken by using a Nikon A1 Spectral IF Confocal

Microscope with an excitation of 488 nm laser source. The bright field images of the laser emissions ("lasing stars") in tissues were captured by using a CCD (Thorlabs #DCU223C) integrated directly on top of the objective in our experimental setup (see Fig. 5.3(a)).

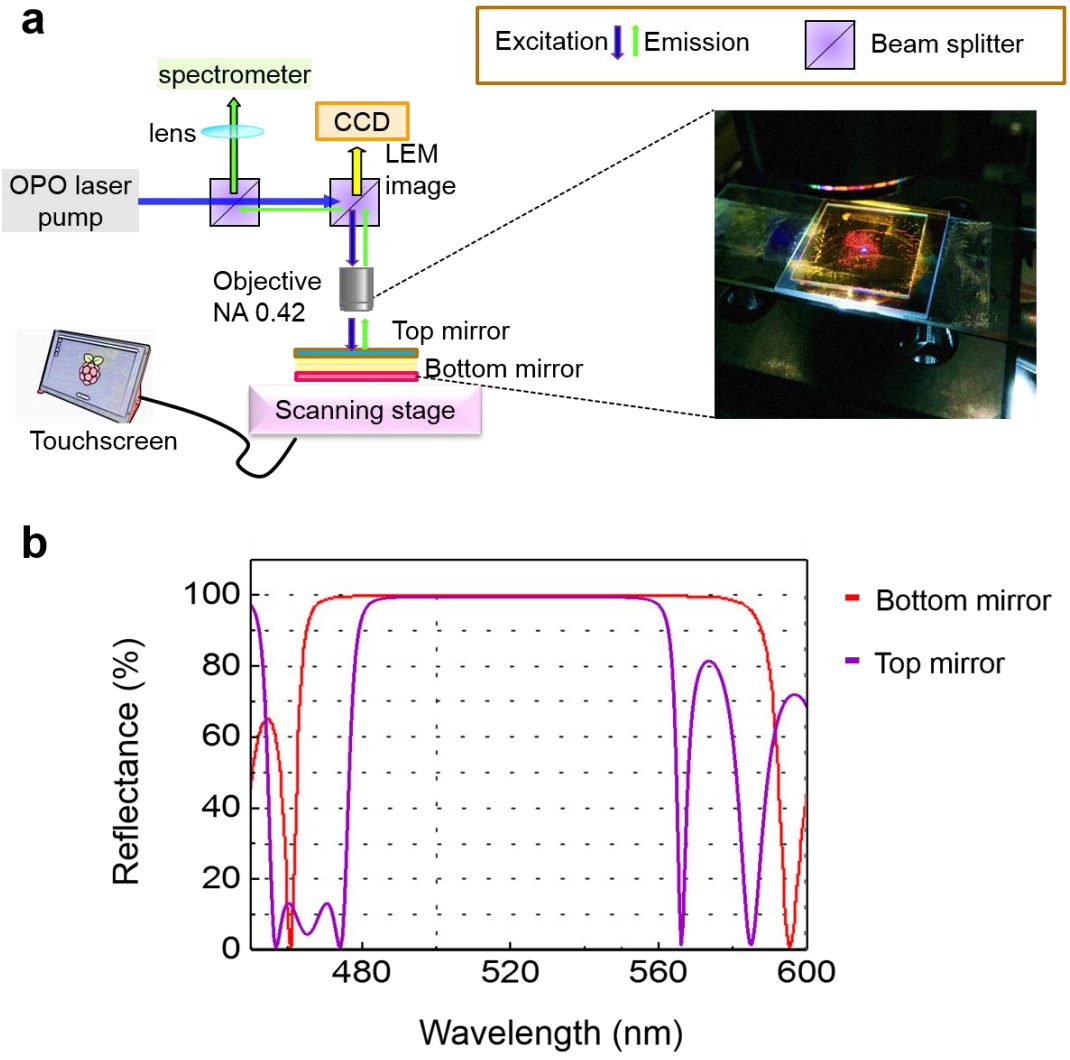

Figure 5.3. LEM setup and mirror profile. (a) Schematic of the experimental setup of the laser-emission based microscope (LEM) and structure of the FP cavity. The focal beam size (spatial sampling area of the spectrum) is 30 μm in diameter. The enlarged figure on the right shows the picture of a lung tissue section sandwiched between the two mirrors while pumped by a 465 nm excitation source. **(b)** The reflectance spectra of the top mirror (purple curve) and the bottom mirror (red curve). The reflectivity of the mirrors around the lasing emission wavelength (535-555 nm) is measured to be 99.98 % for bottom mirror and 99.80 % for the top mirror.

A typical confocal setup was used to excite the sample and collect emission light from the FP cavity (see the optical setup in Fig. 5.3(a)). A pulsed OPO laser (pulse width: 5 ns, repetition rate: 20 Hz) at 465 nm was used to excite the stained tissues. The FWHM of the focused laser beam size was ~ 30 μm in diameter, in which the spatial sampling area is slightly larger than the focal beam size. The emission light was collected through the same objective then separated by a beam splitter to the spectrometer and CCD for spectral and image analysis.

The laser-emission scanned images were collected through the same optical setup, in which the images were taken by the CCD (10 fps, Thorlabs #DCU223C) mounted on top of the objective (NA 0.42, 20X). The raster scanning stage was home-built using two linear actuators with electric controllers (Newport #CONEX TRA25CC) and integrated with a raspberry PI/ touchscreen (Digikey #8997466) for operation. The LEM images shown in Figs. 5.12-5.15 (FOV of 150 μm x 150 μm per frame in this work) was formed by mapping and integration of 25 individual CCD images (30 μm x 30 μm). However, larger mapping area up to 1mm x 1mm is achievable with the aid of algorithms. Currently the accuracy of the stage is limited by 3 μm during each displacement.

5.3. Materials and methods

Tissue materials and device preparation

In this study, a total of 41 tissue samples (N=41) from 35 patients' tissue were used, including human lung tissues (N=38, labeled as P1-P32) and human colon tissues (N=3, P33-P35). In particular, P18-P20 are identified as early stage lung cancer samples. All the human lung and colon tissues were purchased from OriGene Technologies in the form of OCT (Optimal Cutting Temperature) frozen tissue blocks. Both male and female patients diagnosed with stage I/II cancer, aging from 46-78 were examined. All human subjects are fully informed and are explicitly asked

for their consent to future research use of their samples. Samples are collected from a diverse set of medical institutions throughout the United States in order to maximize patient diversity. Those tissues were verified at the Company by pathologists with full pathological evaluation data, clinical annotation (including patient age, gender, and minimum stage grouping), abstracted pathology reports to ensure the accuracy of the sample level diagnosis (i.e., a normal adjacent sample collected from a cancer patient) and detail the sample's cellularity (% normal cells, % lesion cells, % tumor cells, % stroma and % necrosis). For the exemplary tissues demonstrated used in Fig. 8, both tissues were examined by pathologists and verified with lung adenocarcinoma and EGFR.

Upon receiving, all OCT tissue blocks were sliced into 15 μm thick sections by using a cryostat (Leica 3050S). The selected tissue section was picked up and placed on the top of a poly-L–lysine (Sigma-Aldrich #P8920) coated dielectric mirror, which was first cleaned and rinsed with lysine for better tissue adhesion. The tissue were then rinsed with PBS (phosphate buffered solution, ThermoFisher # 10010023) and air dried before staining/labeling (see staining/labeling details in the next section). Finally, the tissue was covered by the top dielectric mirror. For confocal IF microscopy, the tissue was first deposited on the top of a superfrost glass slide (ThermoFisher #3021-002), followed by the same staining process, and then mounted with Fluoromount (Sigma-Aldrich #4680) and covered with a coverslip before scanning.

For the optical laser experiments, all tissues were first examined with H&E histopathology slides to select the area that consists of all tumor cells or all normal cells. All of the tissues were sectioned into 4 slices and at least 5 cells within the tumor/normal region from each tissue section were randomly selected and measured. All cells were measured under various pump energy density to verify lasing emission for each single lasing star.

Staining and labeling methods

For IHC staining, the tissue was fixed on a superfrost glass slide (ThermoScientific #15-188-48) by immersing in pre-cooled acetone (-20 ℃) for 3 minutes and dried off at room temperature. The slide was then rinsed with PBS twice. Next, the tissue was first blocked with BSA buffer for 10 minutes to prevent non-specific binding and rinsed with PBS thoroughly. Then the tissue was incubated with 200 µl of diluted primary antibody (anti-human-EGFR antibody (abcam #52894) overnight at 4 ^{o}C. The primary antibody was prepared with 1:50 solution, with a final concentration of 0.005 mg/ml. After incubation of primary antibodies, the tissue was rinsed with PBS, followed by 30 minutes of staining with HRP conjugated anti-Rb IgG secondary antibody (abcam #6721) at room temperature with a dilution of 1:200 (final concentration=0.01 mg/ml). Then DAB substrate solution (abcam #64238) was applied to the tissue for 5 minutes to reveal the color of the antibody staining. After rinsing 5 times, the tissue was dehydrated through pure alcohol, then mounted with mounting medium (abcam #ab64230), and finally covered with a coverslip. The same procedure was applied to both lung and colon tissues. For colon tissues, two additional primary antibodies, anti-mutant p53 (abcam #32049) and anti-Bcl-2 (abcam #182858), were used.

For nucleic acid labeling, YOPRO solution (ThermoFisher #Y3603) was dissolved in PBS at a concentration of 0.5 mM, then diluted to lower concentrations with PBS. The prepared YOPRO solution was then applied to the tissue sections for 10 minutes and rinsed with PBS solution three times before measurements. The above process is the same for both IF and laser measurements.

For antibody-fluorophore labeling of lung tissues, the glass slide was first rinsed with PBS twice and blocked with BSA buffer for 10 minutes to prevent non-specific binding, then rinsed

again with PBS. Next, the tissue was incubated with 200 µl of diluted primary antibody (anti-human-EGFR antibody (abcam #52894)) overnight at 4 ^{o}C. The primary antibody was prepared with 1:50 solution, with a final concentration at 0.01 mg/ml. After incubation with primary antibodies, the tissue was rinsed with PBS thoroughly, followed by FITC conjugated anti-Rb IgG secondary antibody (stained for 2 hours at room temperature). The secondary antibody (ThermoFisher #65-6111) was prepared with 1:5 dilution to reach the final concentration of 0.2 mg/ml. Finally, the tissue was rinsed again with PBS before laser experiment. The same procedure was applied to colon tissues, in which the primary antibodies, (anti-EGFR antibody (abcam #52894), anti-mutant p53 antibody (abcam #32049) and anti-Bcl-2 antibody (abcam#182858), were used, followed by FITC conjugated anti-Rb IgG secondary antibody (stained for 2 hours at room temperature). The above process is the same for both IF and laser measurements.

For dual staining of anti-EGFR-FITC and YOPRO, we first applied anti-EGFR-FITC (the same procedure as described for primary and secondary antibody labeling) to the lung tissue sections, then 0.1 mM YOPRO solution was applied for 20 minutes to the same tissue and rinsed with PBS solution twice before measurement. For staining of SYTOX Blue (ThermoFisher #S11348) and BOBO-1 Iodide (ThermoFisher #B3582) in Fig. 5.26, SYTOX and BOBO-1 Iodide were dissolved in PBS at a concentration of 0.2 mM, following by the same staining procedures as for YOPRO.

5.4. Results and discussion

The detailed description of mirror fabrication/characterization, FP cavity assembly, and the laser emission-based microscope (LEM) setup can be found in Methods and Fig. 5.3. All the human tissue sections (cancerous and normal) were prepared under the same conditions with a

thickness of 15 μm, all of which were labeled with either YOPRO to target nucleic acids inside cells or FITC-conjugated antibodies that bind specifically to EGFR, mutant-p53, or Bcl-2, which can be expressed on the cell membranes, cytoplasmic organelles (endoplasmic reticulum, Golgi, and endosome), and nuclei. It should be noted that these antibodies are not only specific to the cell nuclei; however, clinical studies have identified the prescence of such biomarkers in the nuclei as a critical sign to determine the patients' survival rate and prognosis[158,163]. Details of sample preparation and staining procedures can be found in Methods.

5.4.1. Lasing in lung tissue with nucleic acids probe

We began with the lung tissues labeled with YOPRO. Figs. 5.4(a) and (b) show the lasing spectra of cancerous and normal lung tissues under various pump energy densities when 0.5 mM YOPRO solution was used to label the tissues (H&E images in Fig. 5.5). A sharp lasing peak emerges around 547 nm. As a control experiment (not shown), no lasing was observed with pure YOPRO solution (without any tissue) at 0.5 mM, which is expected, as YOPRO has virtually no emission in the absence of nucleic acids. The spectrally integrated laser emission versus pump energy density extracted from Figs. 5.4(a) and (b) are both presented in Fig. 5.4(c), from which the lasing threshold of cancer and normal tissue are derived to be 21 $\mu J/mm^2$ and 32 $\mu J/mm^2$, respectively. Furthermore, in Fig. 5.4(d) we investigated the dependence of the lasing threshold on the concentration of the YOPRO solution used to stain the tissues at a fixed resonator length (15 μm) for both cancer and normal tissues. When the YOPRO solution concentration decreases from 0.5 mM to 0.05 mM, the effective YOPRO concentration within a nucleus is expected to decrease accordingly, which leads to a drastic increase in the lasing threshold, especially for the YOPRO concentration below 0.25 mM. For all YOPRO concentrations, we find that the lasing thresholds for cancer tissues are consistently lower than those of normal tissues, which may attributed to the

higher amount of nuclear chromatin (and hence higher YOPRO concentrations) inside cancer cells (due to higher DNA replication activities)[146,175,176]. In addition, we notice that in Figs. 5.4(a) and (b) the lasing emissions remain single mode operation even at a pump energy density significantly higher than the respective lasing threshold. The full-width-at-half-maximum (FWHM) of the lasing emission is only 0.16 nm, limited by the spectrometer resolution. Such a single-mode lasing emission band is >100X narrower than that for the corresponding fluorescence, thus enabling highly wavelength-multiplexed detection. Although at an extremely high pump energy density (5X threshold) the YOPRO-stained tissue can support multi-mode lasing operation (see Fig. 5.6), the overall lasing band is still less than 10 nm wide, attesting to the intrinsic narrow gain profile for YOPRO, despite a wide fluorescence band.

Fig. 5.4(e) shows the confocal fluorescence microscopy image of a nucleus in a cancer cell from the lung cancer tissue. Due to the low contrast of the fluorescence emission within the nucleus, we are unable to extract the exact locations having high nucleic acid concentrations. However, as visualized by the CCD images in Figs. 5.4(f) and (g), multiple sharp laser emissions with distinct and strong output against the surrounding background emerge like bright stars in the dark sky (“lasing stars”) from the specific sites having the highest abundance of nucleic acids. With the increased pump energy density, more sites having slightly lower abundance of nucleic acids start to lase (see Movie 1). Note that there may be fluorescence background emitting from the places that have relatively low concentrations of nucleic acids and therefore are unable to generate laser emission. However, such fluorescence is completely blocked by the top mirror that has >99.8 % reflectivity. Similarly, in Figs. 5.4(h-j) we also carried out a series of parallel experiments using a normal lung tissue and observed the same phenomena as in Figs. 5.4(f-g), except that the lasing stars start to emerge at a higher pump energy density and, at a given pump energy density, fewer

lasing stars are observed, both of which reflect the lower abundance of nucleic acids in a normal tissue, as discussed previously in Fig. 5.4(d).

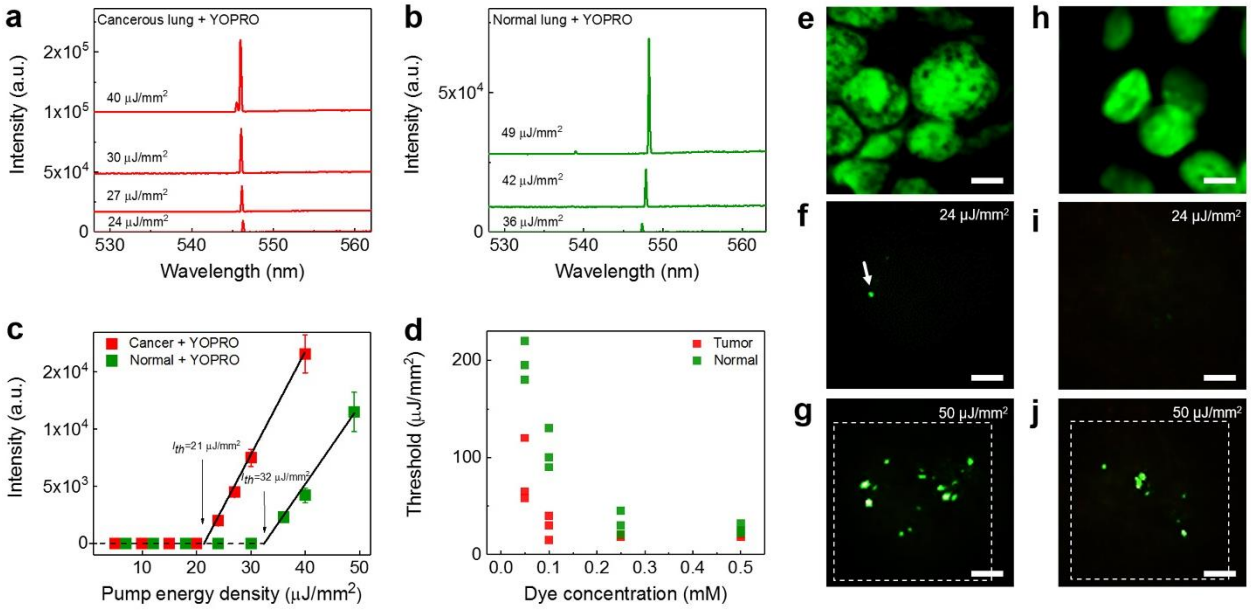

Figure 5.4. Lasing in lung tissue with nucleic acid staining dye. (a-b) Examples of lasing spectra of a human lung cancer tissue (**a**) and normal lung tissue (**b)**, stained with YOPRO under various pump energy densities. Curves are vertically shifted for clarity. **(c)** Comparison of spectrally integrated (540 nm – 550 nm) laser output as a function of pump energy density extracted from the spectra in (a) and (b). The solid lines are the linear fit above the lasing threshold, indicating a lasing threshold of 21 μJ/mm^2 for cancer tissue and 32 μJ/mm^2 for normal lung tissue. The error bars (s.d.) are defined by considering the pump energy density variation of OPO pulsed laser during the measurements. **(d)**, Lasing threshold with different concentrations of YOPRO used to stain the tissue. Three individual measurements were measured for each concentration at different sites, as presented individually in green and red squares. **e**, Confocal fluorescence image of a lung cancer nucleus (shown in green). (**f-g)** CCD images of the laser output from a nucleus in a lung cancer tissue (**f**) around (24 μJ/mm^2) and (**g**) far above (50 μJ/mm^2) the lasing threshold. The image shows clearly several sharp "lasing stars" within the nucleus, whereas the background fluorescence is significantly suppressed. **h**, Confocal image of a normal lung nucleus (in green). (**i-j)** CCD images of the laser output from a nucleus in a normal lung tissue (**i**) below (24 μJ/mm^2) and (**j**) above (50 μJ/mm^2) the lasing threshold. Note that e/h and g/j were taken from the same piece of tissue, but does not exactly represent the same cells. All the tissues in (a-j) were stained with YOPRO (0.5 mM in bulk staining solution) under the same preparation conditions. The dashed squares in (g) and (j) show the laser pump beam area in LEM. All scale bars, 5 μm. The corresponding H&E images of the cancer tissues and normal tissues are provided in Fig. 5.5.

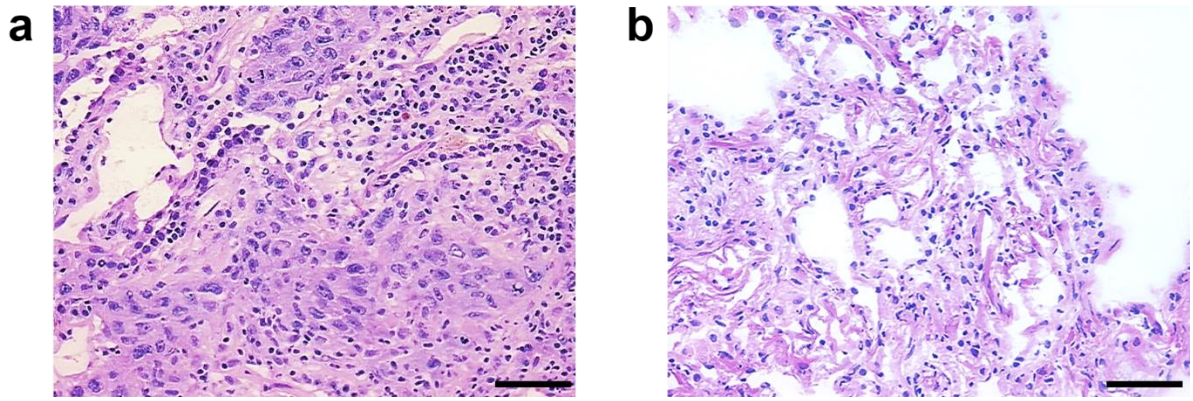

Figure 5.5. H&E images of lung tissue used in Fig. 5.4. H&E images of the **(a)** lung cancer tissue and **(b)** normal lung tissue. Both human lung tissues were examined and diagnosed by pathologists. Scale bars, 150 μm.

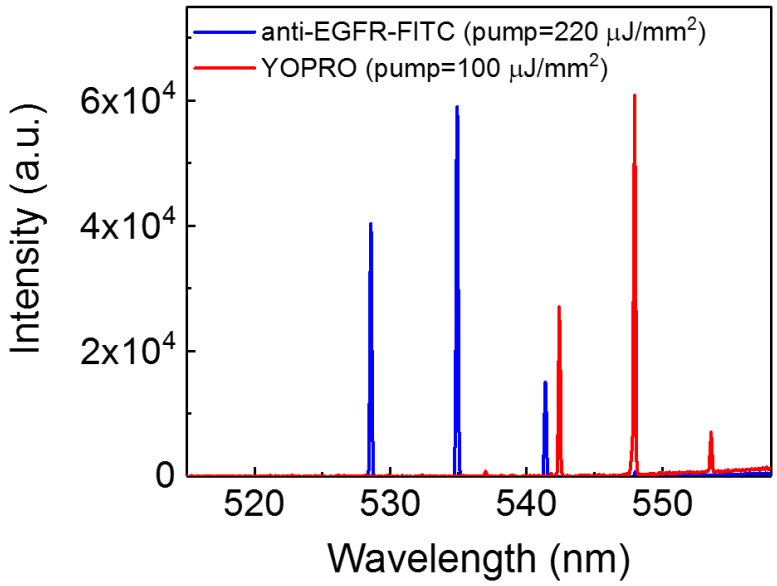

Figure 5.6. Lasing spectra of YOPRO and EGFR-FITC at high pump. Lasing spectra of a lung cancer tissue labeled with 0.5 mM YOPRO (red curve) and a lung cancer tissue labeled with anti-EGFR-FITC. Both samples were pumped at a relatively high pump energy density, showing the existence of multiple laser modes. Excitation wavelength=465 nm.

5.4.2. Characterization of LEM and lasing stars

To further characterize those "lasing stars", in Fig. 5.7(a) we plot the laser emission profile of a single lasing star from the lung cancer tissue captured on the CCD. The FWHM is measured to be approximately 678 nm, providing a sub-micron and sub-cellular optical resolution (defined by the FWHM). Fig. 5.7(b) illustrates that two adjacent lasing stars separated by only 1.3 μm can be well resolved. Comparison among bright field images, fluorescence images and laser-emission images using the identical cancer cells is given in Fig. 5.8, showing high spatial resolution and high contrast of the LEM, which is due mainly to the background suppression mechanism in the LEM (the background here is defined as the noise or low level signals *within* the cell nuclei).

The insets of Figs. 5.7(c-f) illustrate that the sub-cellular lasing stars emerge progressively from a single to multiple lasing stars within the same pumping beam spot when the pump energy density increases gradually. The spectral analysis in Figs. 5.7(c-f) suggests that those lasing stars are independent of each other. Each of them is in single lasing mode operation, but may have slightly different lasing wavelengths due possibly to different local environments (such as nucleus thickness, refractive index, and gain distribution, etc.). Furthermore, spatial analysis shows that those lasing stars are the lowest order (0,0) Ince-Gaussian mode[51,52]. As exemplified in Figs. 5.7(c-f), at a relatively low pump energy density, only those sites having the highest analyte concentration can lase. With the increased pump energy density, lasing from multiple sites can be observed. Conversely, multiple lasing sites can be "turned-off" down to a single lasing site by decreasing the pump energy density, signifying the repeatability and controllability of lasing stars.

Furthermore, spatial analysis shows that those lasing stars are the lowest order (0,0) Ince-Gaussian mode[51,52], which is due largely to the localization of nucleic acids (and hence the YOPRO). In order to validate this, we conducted a series of experiments by staining lung normal/ cancer tissues with FITC (non-specific dye) for comparison (Fig. 5.9). Despite the refractive index

differences, similar lasing modes (generally higher order Ince-Gaussian modes) were observed for both normal and cancer cells (Fig. 5.9 (d) and (e)), suggesting that FITC is equally distributed throughout the cell. In contrast, multiple independent lasing modes (lasing stars) can be observed in cells when labeled with YOPRO.

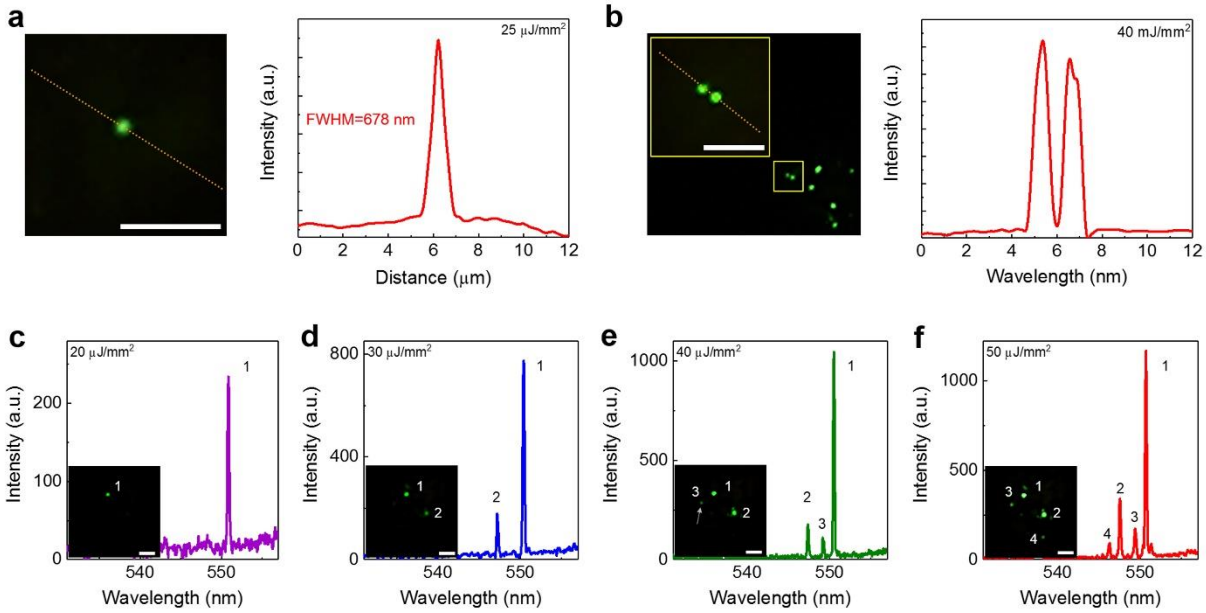

Figure 5.7. Optical resolution of sub-cellular lasers under LEM. (a) Enlarged CCD image (left) of a single laser emission star from a human lung tissue stained with YOPRO. The intensity profile along the yellow dotted line (right) shows the FWHM of 678 nm. (**b)** Enlarged CCD image (left) of two adjacent lasing stars. The yellow square identifies the location of two lasing stars within the tissue. The intensity profile along the yellow dotted line (right) shows two well-resolved peaks. The smallest resolvable distance between two laser emissions is estimated to be better than 1 μm. (**c-f)** Lasing spectra of independent sub-cellular lasers within the same focal beam spot by increasing the pump energy density from (**c**) 20 μJ/mm^2, (**d**) 30 μJ/mm^2, (**e**) 40 μJ/mm^2, to (**f**) 50 μJ/mm^2. The insets show the CCD images of corresponding laser emissions, in which (c) is an example of a single lasing star, (d) is an example of two independent lasing stars with different lasing thresholds, € is an example of three independent lasing stars with different lasing thresholds, and (f) is an example of multiple independent lasing stars emerging simultaneously at a high pump energy density. Note that the slight increase in the background emission beyond 560 nm in (c-e) is due to the fluorescence leaking out of the FP cavity caused by the reduced reflectivity of the dielectric mirror (see Fig. 5.3 for details). NA= 0.42. All scale bars, 5 μm.

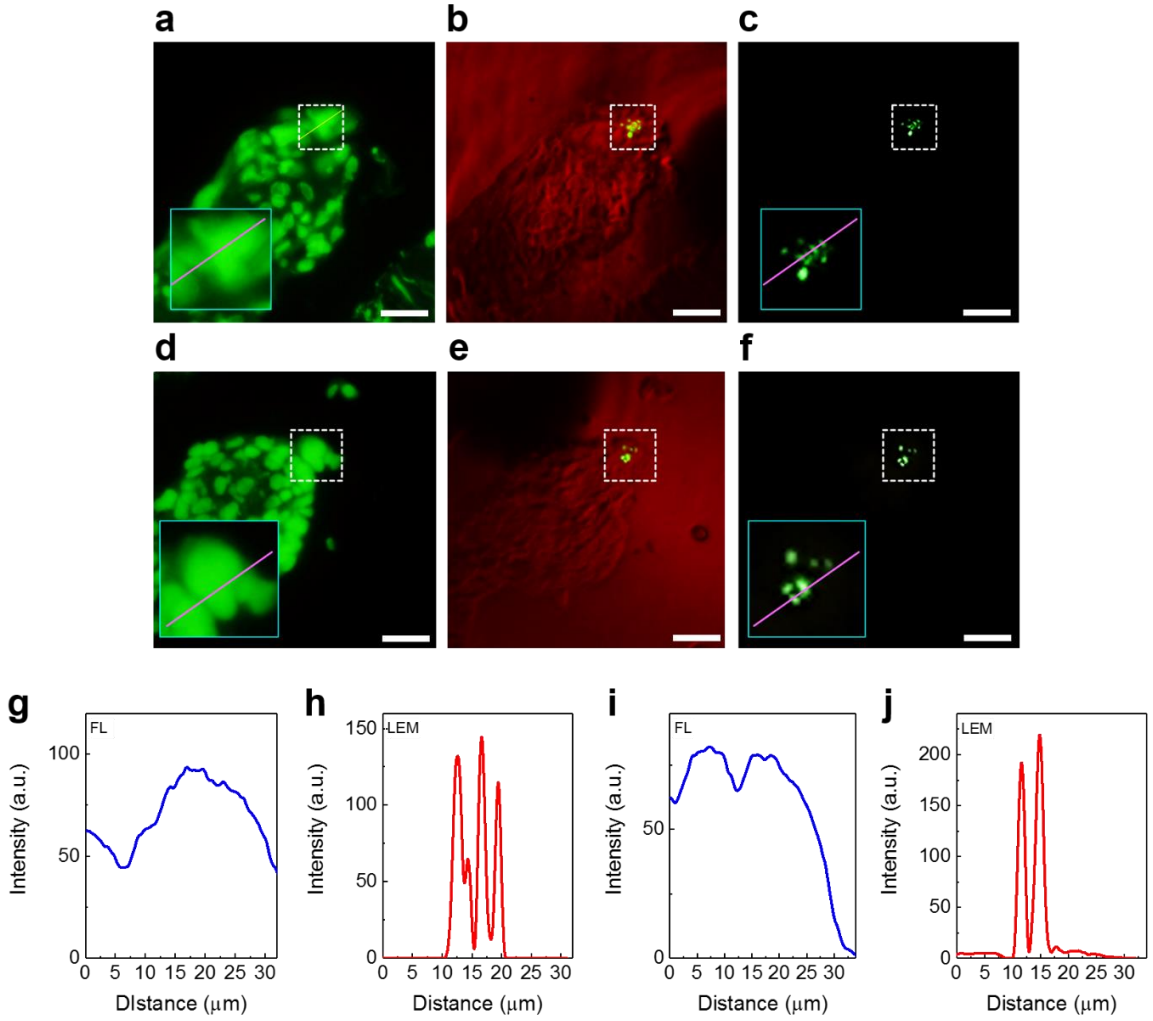

Figure 5.8. Comparison of LEM and FL microscopy. Comparison of fluorescence microscopic image (**a**, **d**), bright field CCD image (**b**, **e**), and lasing-emission CCD image (**c**, **f**) of the identical cells. Two sets of examples from different tissue sections/cells (obtained from Patient 18) are given here in (**a-c** and **d-f**, respectively). Laser was only pumped within the dashed boxed regions in b, c, e and f. The bottom-left boxes in a, c, d and f show the enlarged images of the dashed boxed region in the respective figures. The difference between the high resolution and high contrast "lasing stars" (**c**, **f**) and low resolution and low contrast "fluorescent clouds" (**a**, **d**) is obvious. For detailed comparison, (**g)** and (**h)** show the intensity profile along the pink lines in images (a) and (c) (example 1), respectively. (**i)** and (**j)** show the intensity profile along the pink lines in images (d) and (f), respectively (example 2). The cancer tissues were stained with 0.1 mM YOPRO. Scale bars, 30 μm. Here the fluorescence images in Fig. 5.8 were first captured with a wide-field fluorescence microscope (without the top mirror), then immediately the corresponding lasing measurements were performed by covering the tissue samples with the top mirror.

The significant difference between FITC and YOPRO in Fig. 5.9 supports the hypothesis that the lasing star is caused by the localization (concentration) effect of nucleic acids (and hence dyes). Consequently, the results in Fig. 5.7 provide an alternative method to quantify the analyte concentration in tissues (or cells) with a sub-micron spatial resolution by ramping the pump energy density. The image for each the pump energy density can be recorded so that the distribution of analyte relative concentration can be mapped and the histogram of the sites having different levels of analyte concentrations can be built, thus enabling more detailed characterization of tissues.

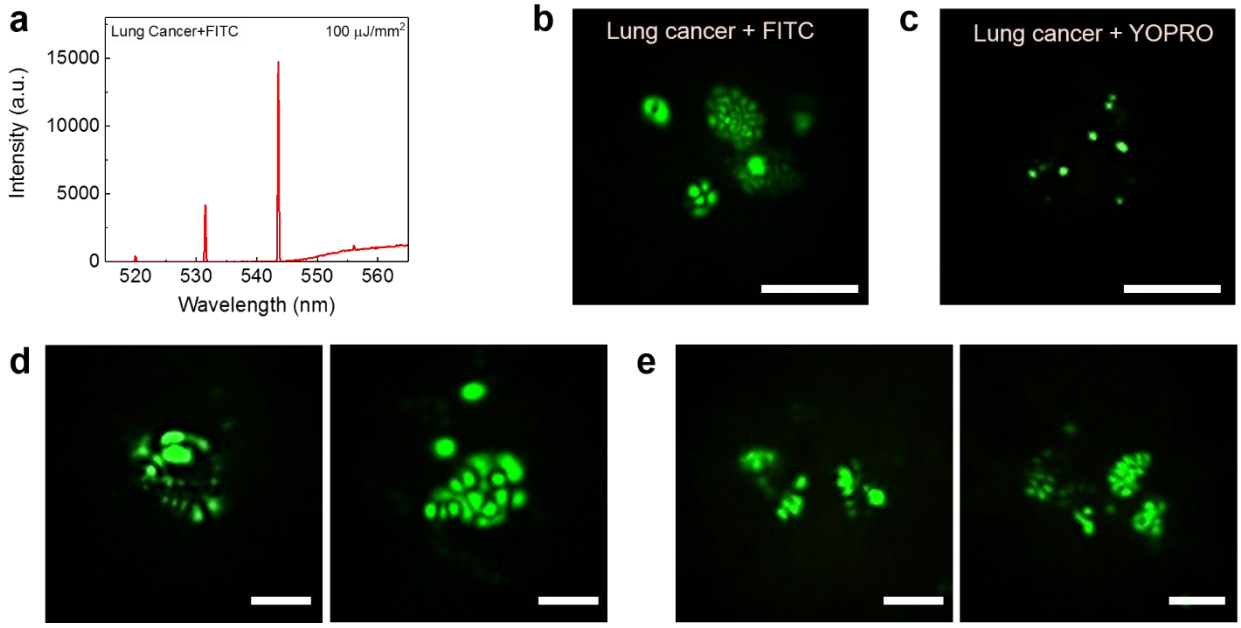

Figure 5.9. Lasing modes of lung tissue stained with non-specific dye. (**a)** Lasing spectrum of lung cancer tissue stained (soaked) with non-specifc dye, fluorescein isothiocyanate (FITC). (**b)** CCD image of the lasing emissions from lung cancer tissue stained non-specifically with FITC. Multiple cells with different lasing mode profiles are observed. Those lasing modes are usually higher order Ince-Gaussian modes. However, for each cell, only one lasing mode exists. (**c)** CCD image of the lasing emission (multiple spatially isolated lasing stars) from cancer cells/tissue labled with YOPRO. Those lasing stars are independent of each other and are the lowest order Ince-Gaussian mode. The tissues were stained with FITC or YOPRO with the same concentration (0.1 mM) and pumped under 50 μJ/mm^2. **(d)** Lasing modes observed from lung cancer cells/tissue non-specifically stained with FITC. **(e)** Lasing modes observed from normal lung cells/tissue non-specifically stained with FITC. Objective NA= 0.42. Scale bars, (b-c), 20 μm; (d-e), 10 μm.

5.4.3. Statistics of normal/cancer cell lasing thresholds

According to the results in Fig. 5.4(d), the lasing thresholds for the cancer cell nuclei are generally lower than those for the normal cell nuclei. In particular, Fig. 5.4(d) shows that the binding of YOPRO to nuclear acids starts to saturate beyond 0.1 mM in cancer tissues. Thus, the largest difference in lasing threshold is achieved at 0.1 mM, which can be explored to distinguish between the cancer and normal tissues. In Fig. 5.10 we systemically investigated the lasing thresholds of 14 patients' biopsies (including 10 sets of normal/cancer lung tissue, H&E images are given in Fig. 5.11), all of which were stained with 0.1 mM YOPRO. First, we present the statistics of lasing thresholds based on the 6 pairs of lung cancer tissues and normal lung tissues from the same patients (P1-P6) in Figs. 5.10(a) and (b), respectively. In particular, two types of non-small cell lung cancer, andenocarcinoma and squamous cell carcinoma (Fig. 5.10(c) for example), were investigated. At least 20 cells were randomly selected and measured within each tumor/normal tissue region for each patient. Interestingly, all cancer cells exhibit consistently a narrow lasing threshold range around 20 $\mu J/mm^2$. In contrast, the normal cells have a much wider threshold range, varying from 30 $\mu J/mm^2$ to 180 $\mu J/mm^2$. Next, we investigated the lasing thresholds based on 4 pairs of cancer and normal tissue from 8 different patients (4 normal: P7-P10 and 4 cancer: P11-P14) in order to examine the sample-to-sample variations. Similar statistic results of lasing thresholds were observed in Figs. 5.10(d) and (e). Both the p values of two sample t-Test between normal and tumor cells in both cases (same patient/ different patient) are < 0.005.

The histogram of the lasing thresholds (N=472 cells) in Fig. 5.10(f) extracted from Figs. 5.10 (a), (b), (d), and (e) shows clearly a cutoff threshold around 30 $\mu J/mm^2$ between the normal and cancer cells. As discussed previously, the stark difference in the lasing threshold is attributable to the different nucleic acid concentrations within cell nuclei[177]. As shown in the fluorescence

images in the inset of Fig. 5.10(f), normal cells undergo regular cell cycles/stages, whereas cancer cells are highly active abnormal cells that undergo endless divisions and DNA replication. The high proliferation of DNA (chromatins) in cancer cell nuclei will result in high nucleic acid concentrations, thus lower lasing thresholds.

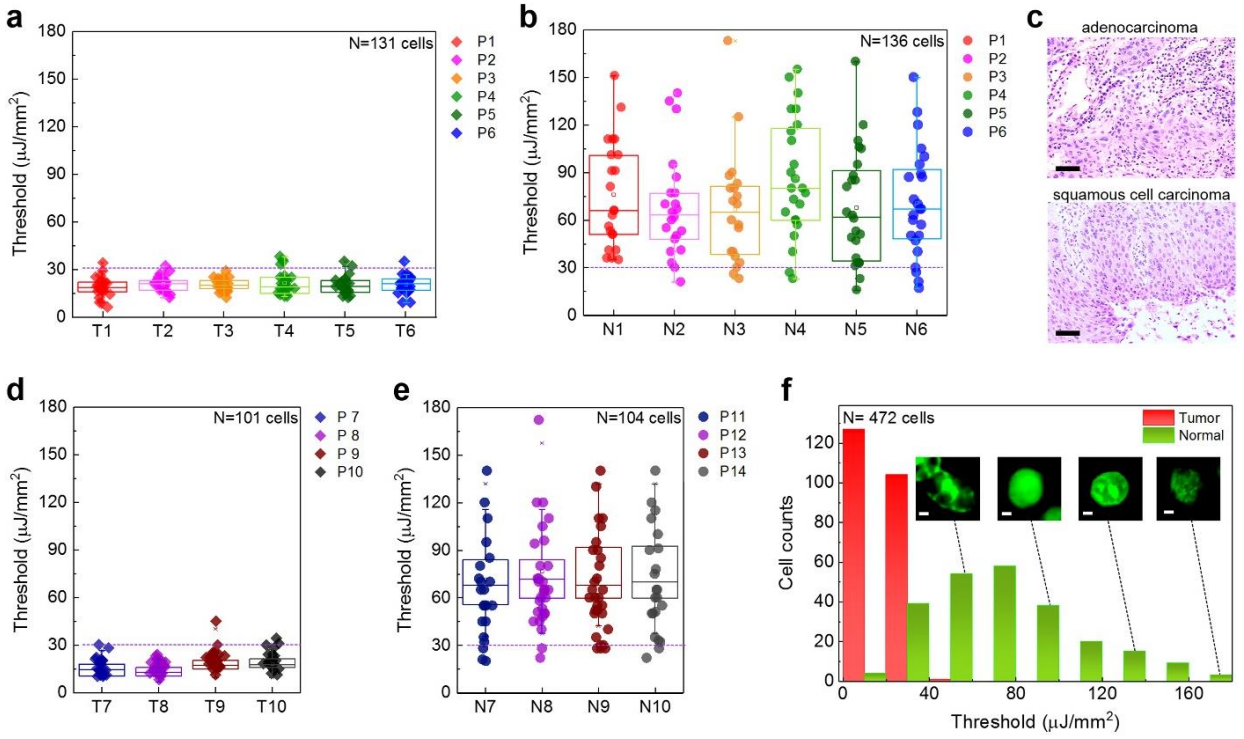

Figure 5.10. Statistics of cancer/normal cell lasing thresholds. (a) Statistics of tumor cell lasing thresholds from six individual lung cancer patients (P1, P2, P3, P4, P5, P6), labeled as Tumor tissue, T1-T6. For each patient, at least 20 cells were randomly selected and measured. (**b)** Statistics of normal cell lasing thresholds of normal lung tissues from the same six patients (P1-P6) in **a**, labeled as Normal tissue N1-N6. (**c)** Exemplary H&E microscopic images of the two major types of non-small lung cancers used in this work, including andenocarcinoma (top) for P1-P3 and squamous cell carcinoma (bottom) for P4-P6. Scale bars, 100 μm. (**d)** Statistics of tumor cell lasing thresholds from four different lung cancer patients (P7, P8, P9, P10), labeled as Tumor tissue, T7- T10. **(e)** Statistics of normal cell lasing thresholds of normal lung tissues from four different control patients (P11-P14), labeled as Normal tissue N7-N10. For each patient, at least 20 cells were randomly selected and measured. The error bars (s.d.) in **(**a, b, d and e) are definded by the laisng threshold variation of 20 cells measured from each patients, respectively.The statistical box plots are also shown in the same figure in (a, b, d and e**)**. The dashed purple lines in (a, b, d, and e) indicate the cutoff threshold of 30 μJ/mm^2. **(f)** Histogram of all cancer/normal cell lasing thresholds (N=472) extracted from (a, b, d, and e). The insets show the confocal fluorescence images of normal cells at different cell phases. Scale bars, 1 μm.

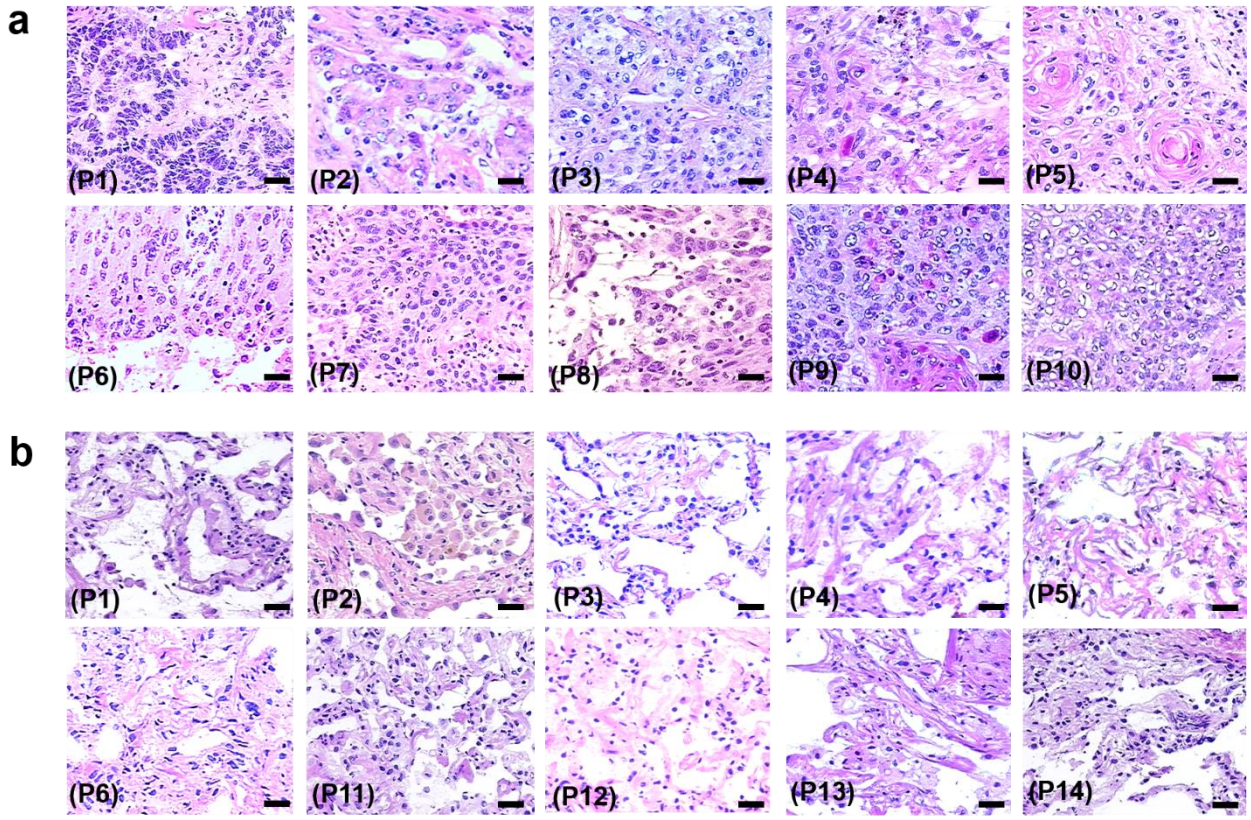

Figure 5.11. H&E images of lung cancer tissues used in Fig. 5.10. (**a)** H&E images labeled as Patient 1 (P1), Patient 2 (P2), Patient (P3), Patient 4 (P4), Patient 5 (P5), Patient 6 (P6), Patient 7 (P7), Patient 8 (P8), Patient 9 (P9), and Patient 10 (P10), all of which were evaluated and diagnosed as lung cancer (Stage I and Stage II) by pathologists. P1-P3: lung andenocarcinoma. P4-P6: squamous cell carcinoma. (**b)** H&E images of normal lung tissues used in Fig. 4, labled as Patient 1 (P1), Patient 2 (P2), Patient 3 (P3), Patient 4 (P4), Patient 5 (P5), Patient 6 (P6), Patient 11 (P11), Patient 12 (P12), Patient 13 (P13), and Patient 14 (P14). All scale bars, 50 μm.

5.4.4. Statistical comparison of LEM between normal/cancer tissues

Based on the statistic results in Fig. 5.10(f), in Fig. 5.12 we employed the LEM to distinguish the cancer and normal tissues by mapping the laser emissions from nuclei in both cancer and normal tissues from 3 individual patients (P15, P16, P17, see Fig. 13 for H&E images). For each patient, 5 tissue sections (for both cancer and normal tissues) were scanned with the LEM over a field-of-view of 150 μm x 150 μm under a fixed pump energy density of 30 μJ/mm^2, as

shown in Figs. 5.12(a-c), respectively. It is obvious that no or only a few lasing stars appeared in all normal tissue sections. In contrast, a large number of lasing stars were observed in cancer tissue sections, where isolated individual lasing stars and clusters of lasing stars were both present, since the pump energy density is above the lasing threshold for cancer cells.

Quantitative analyses of the number of lasing cells using the LEM results in Figs. 5.12(a-c) are plotted in Figs. 5.12(d-f) (note: a lasing cell is defined as the cell that has one or more lasing stars). Statistically significant differences between the cancer and normal tissues were achieved ($p < 0.005$ with two-sample t-Test), demonstrating the superior contrast and screening capability of the LEM. As comparison, in Fig. 5.14, we scanned the same tissues with confocal fluorescence microscopy. Figure 5.15 further analyzes the same confocal fluorescence images and shows that the fluorescence of the cancer and normal cells is very similar in intensity and spatial distribution. Those results in Figs. 5.14 and 15 suggest that confocal fluorescence microscopy is unable to distinguish/quantify cancer and normal tissues by nucleic acid expression by simply using fluorescence intensity distribution (Note that in Figs. 5.14 and 15, cancer and normal tissues can still be distinguished by the cell sizes/morphologies. However, for morphology based tissue evaluation, H&E (rather than fluorescence microscopy) is the golden standard. Later in Fig. 5.17 and Fig. 18, we tested the LEM with early stage cancer tissues, where cancer/normal tissues cannot be distinguished by the cell sizes/morphologies). In comparison with histopathology, which is based on morphological assessment of cells and tissues, the LEM method that maps the lasing emissions from nuclei may provide a simpler, more systematic, and quantitative tool to complement the traditional H&E method in tissue characterization.

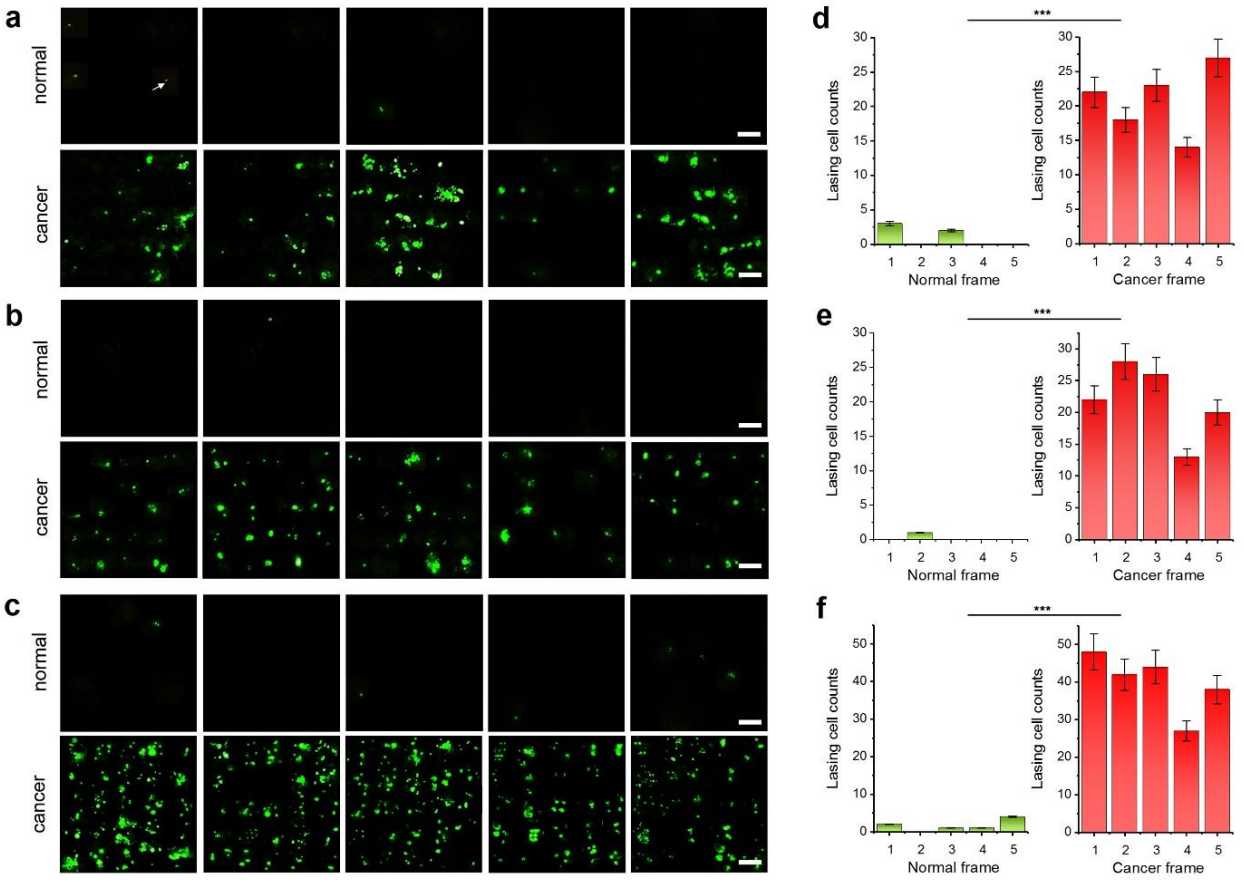

Figure 5.12. Comparison and statistics of laser-emission microscopic images of normal/ cancer tissues. (a-c) LEM images by mapping the nucleic acids in normal and lung cancer tissues of (**a**) Patient 15, (**b**) Patient 16, and (**c**) Patient 17. For each patient, five normal/cancer tissue sections (frames) were scanned under a fixed pump energy density of 30 μJ/mm^2. The white arrow in **a** points an example of a single lasing star in a normal tissue of Patient 1. NA= 0.42. All scale bars, 20 μm. Each frame is 150 μm x 150 μm. The corresponding H&E images of the cancer tissues and normal tissues of the three patients are provided in Fig. 5.13. All three patients' tissues were examined by pathologists and diagnosed as lung cancer. (P15: Stage II, P16: Stage I, P17: Stage I lung cancer). (**d-f)** Statistics of the number of cells per frame that have laser emission from their respective nuclei for (**d**) Patient 15, (**e**) Patient 16, and (**f**) Patient 17 extracted from the LEM images in (a-c). Green/red bars are for the normal/cancer tissues, respectively. The error bars (s.d.) are defined by the variations in lasing cell counts.

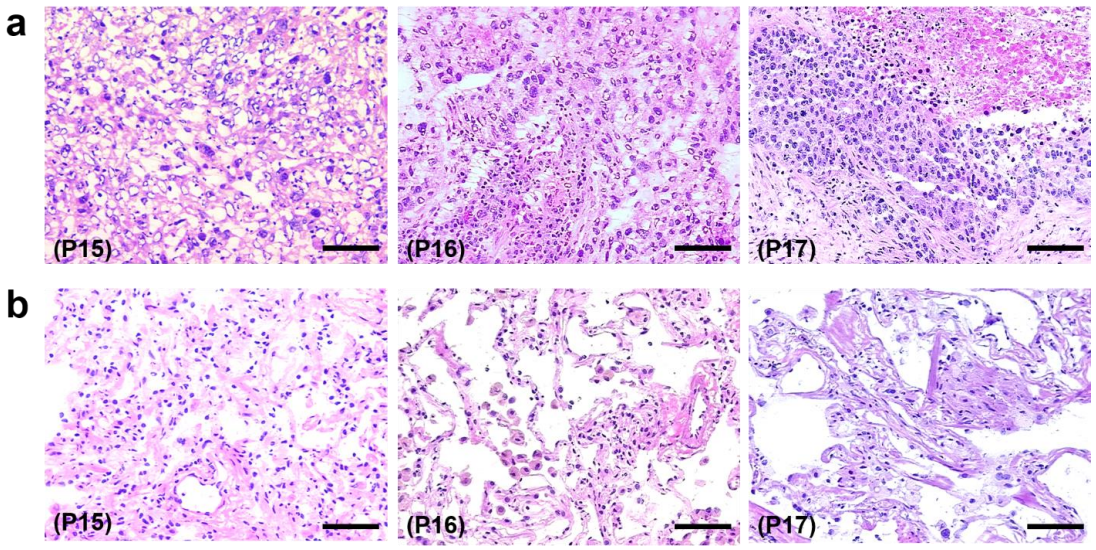

Figure 5.13. H&E images of lung cancer tissues used in Fig. 5.12. (**a)** H&E images labeled as Patient 15 (P15), Patient 16 (P16), Patient 17 (P17),all of which were evaluated and diagnosed as lung cancer (stage I and stage II) by pathologists. (**b)** H&E images of normal lung tissues used in Fig. 5 from the same patients in **a**. All scale bars, 200 μm.

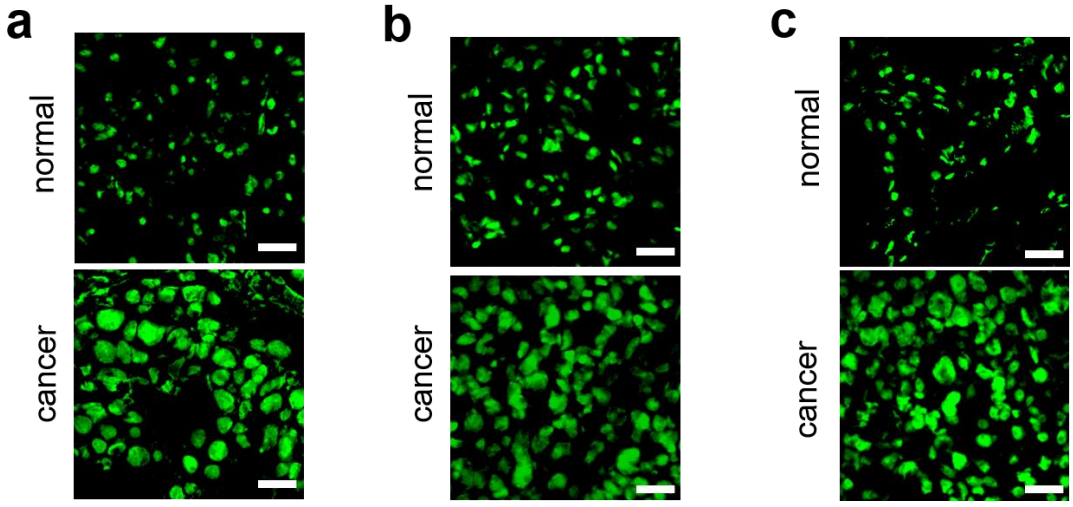

Figure 5.14. Confocal fluorescence microscopic images of normal and lung cancer tissues labeled with YOPRO. (**a**) Patient 15, (**b**) Patient 16, and (**c**) Patient 17. Each set of normal and lung cancer tissues were provided by the same patients as in Fig. 5.12. For confocal fluorescence imaging, only one tissue section from each patient is shown here for demonstration. Objective NA= 0.42. All scale bars, 20 μm. (YOPRO concentration =0.1 mM)

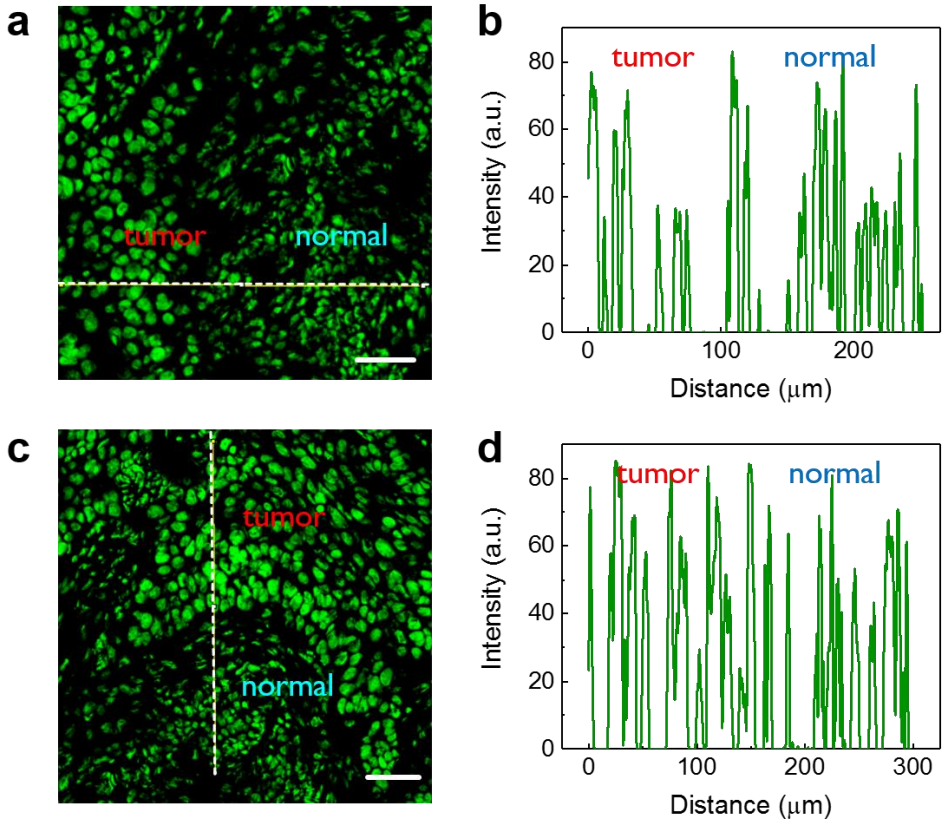

Figure 5.15. Intensity profile of normal/cancer cell under confocal images. (**a**, **c**) Confocal fluorescence images of tissue sections containing both cancer cells and normal cells within the same image for fair comparison. The samples were from the Patient 15 in Fig. 5, but different sections. Here we show only two images for example. (**b**, **d**) The intensity profile along the white dashed lines in image (a) and (c), respectively. Both (b) and (d) show that the fluorescence of the normal and cancer cells is very similar in intensity and spatial distribution, and therefore, cannot be used to characterize and classify tissues. All scale bars, 50 μm.

In order to to establish the sensitivity and specificity of the LEM technique, we randomly selected 8 cancer patients and performed the LEM on both of their normal and cancer tissues. By using the same experimental condition and quantification methods as in Fig. 5.12, five tissue sections (frames) were scanned for each patient for both cancer tissue and normal tissue (a total of 80 frames, N=80). The histogram of the number of the lasing cells per frame for normal tissues and cancer tissues are plotted in Figs. 5.16(a) and (b), respectively. Based on the number of lasing cells per frame, we generate the Receiver Operation Characteristic (ROC) curve in Fig. 5.16(c),

which has the area under the curve of 0.998. We found that the optimal threshold to identify a cancer tissue is "5 lasing cells per frame", which corresponds to a sensitivity of 97.5%. Practically, the threshold can be adjusted for higher sensitivity or higher specificity.

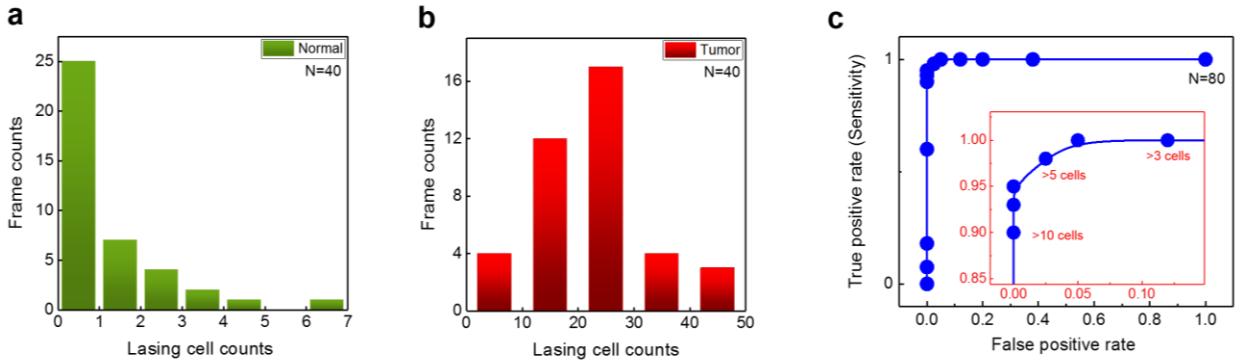

Figure 5.16. ROC calculation of LEM. (a) Histogram of frame counts based on the number of the lasing cells per frame in normal tissues from 8 different patients (P1, P3, P5, P6, P10, P15, P16, P17). For each patient, five frames (150 μm x 150 μm) were scanned under a fixed pump energy density of 30 μJ/mm^2. **(b)**, Histogram of frame counts based on the number of the lasing cells per frame in cancer tissues from 8 different patients (P1, P3, P5, P6, P10, P15, P16, P17). For each patient, five frames (150 μm x 150 μm) were scanned under a fixed pump energy density of 30 μJ/mm^2. **(c)**, Receiver Operating Characteristics (ROC) curve based on the 80 frames (40 normal tissue sections, 40 tumor tissue sections) in (a) and (b). The ROC curve is plotted by using the different lasing cell counts per frame. The area under the curve is 0.998. The inset shows the enlarged part of the ROC curve, in which the sensitivity of 97.5% is obtained based on the criterion of >5 lasing cells per LEM frame.

5.4.5. Early stage lung cancer screening with LEM

Using the threshold established above, we further demonstrated an important application of the LEM by examining early stage lung cancer tissues, which is regarded as the most critical yet challenging task in clinical histopathology. For this study, we used three samples from three patients, who were diagnosed as early stage lung cancer (in-progress lung cancer, see Figs. 5.17a-c for the H&E images). The confocal fluorescence images are provided in the Fig. 5.18. It is obvious that the normal cells, in-progress cancer cells, and cancer cells are completely mixed within the whole tissue, making it very difficult to identify/differentiate according to cell

morphology and/or fluorescence intensity. In contrast, by using the LEM, cancer cells can be unambiguously identified within the tissue with a high contrast. For each patient, 5 sections were scanned with the LEM under a fixed pump energy density of 30 μJ/mm^2, as shown in Figs. 5.17(d-f). Quantitative analyses of the number of lasing cells using the LEM are also plotted in Figs. 5.17(g-i). All three tissues are identified as cancer since all frames have more than 5 lasing cells.

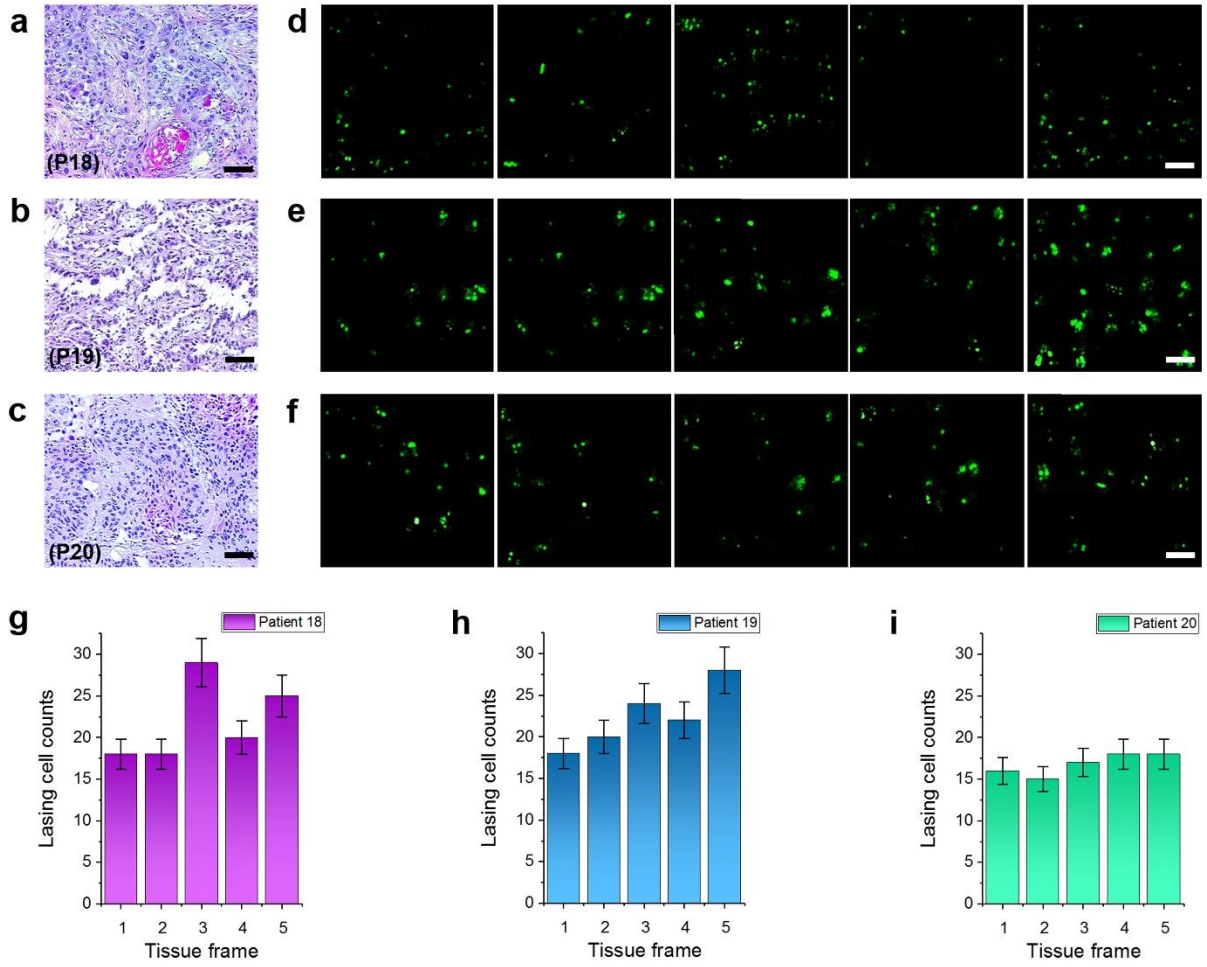

Figure 5.17. Laser-emission microscopic images of early stage lung cancer tissues. (a-c) H&E images of (**a**) Patient 18 (P18), (**b**) Patient 19 (P19), and (**c**) Patient 20 (P20), who are identified as in-progress or early stage lung cancer. (**d-f)** The corresponding LEM images by scanning the nucleic acids of the tissues from the same three patients. For each patient, five tissue sections (frames) were scanned under a fixed pump energy density of 30 μJ/mm^2. (**g-i)** Statistics of the number of cells having lasing emission from nuclei extracted from the LEM images. The error bars (s.d.) are defined by the variations in lasing cell counts. NA= 0.42. Scale bars for (**a-c)** 100 μm; (**d-f)** 20 μm.

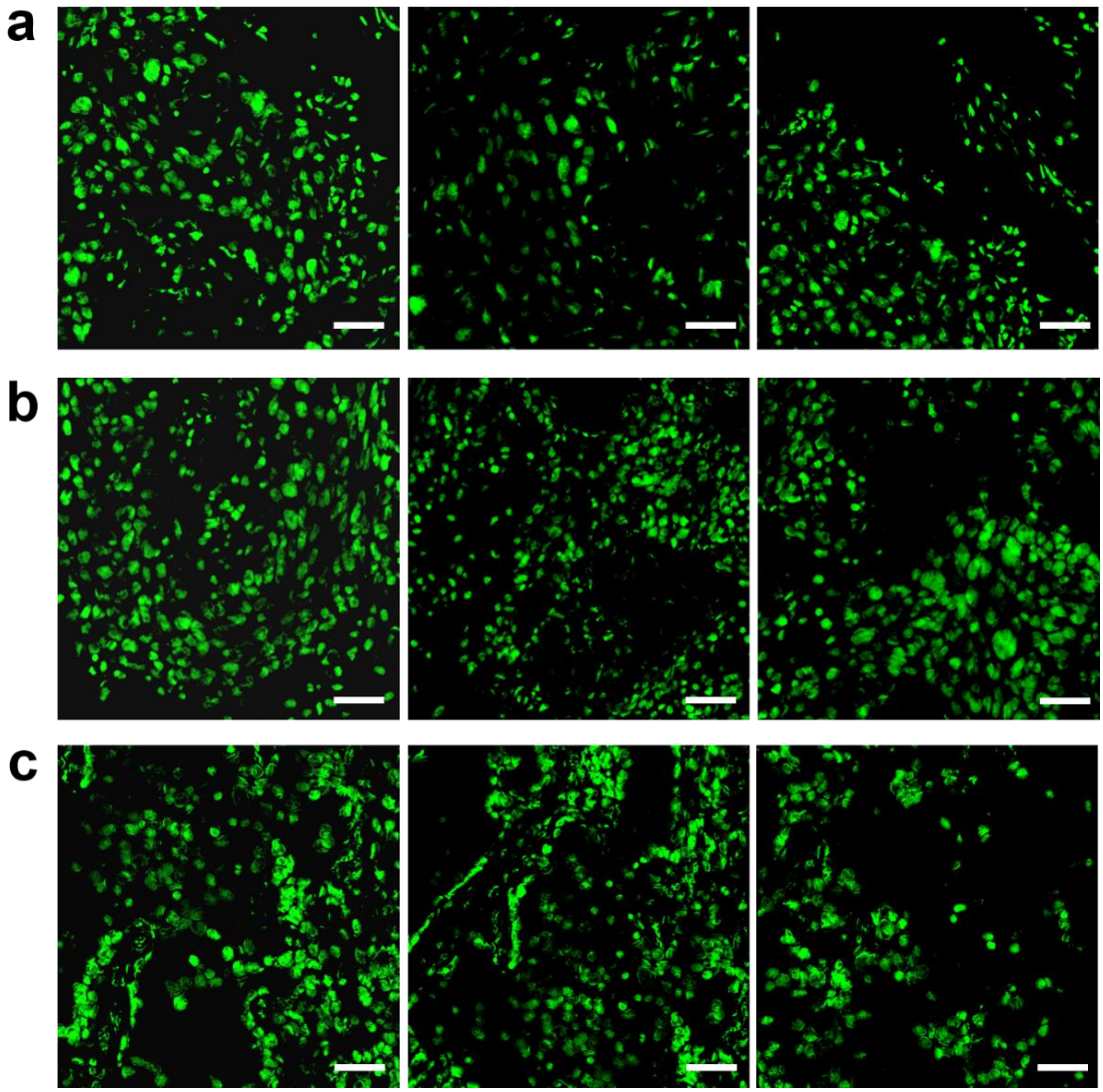

Figure 5.18. Confocal fluorescence microscopic images of early stage lung tumor tissues labeled with YOPRO. (**a**) Patient 18, (**b**) Patient 19, and (**c**) Patient 20. For confocal fluorescence imaging, three different sites/sections from each patient are shown here for demonstration. The tissues used here were from the same patients as in Fig. 5.17 (same tissues but different sections). Objective NA= 0.42. All scale bars, 50 μm.

5.4.6. Multiplexed immuno-lasing in lung cancer tissues

Moving a step forward, we aim to improve the prognostic prediction of cancer patients by demonstrating immunodiagnosis capability of the LEM. Here in Fig. 5.19 we studied the lasing emission using EGFR antibody conjugated with FITC (anti-EGFR-FITC) to target nuclear EGFR (n-EGFR) expressed in the same lung cancer tissue used in Fig. 2. Similar to the YOPRO case in Fig. 5.14(a), Fig. 5.19(a) shows single-mode lasing emission with an FWHM of about 0.16 nm when the pump energy density is slightly above the threshold. Although with the increased pump energy density the second mode emerges, the lasing band is only about 8 nm, much narrower than the corresponding fluorescence band (>60 nm.). The spectrally integrated laser emission versus pump energy density extracted from Fig. 5.19(a) is presented in Fig. 5.19(b), showing a lasing threshold of approximately 67 $\mu J/mm^2$. We further investigated 10 samples from 5 lung cancer patients with nuclear EGFR positive response (Patients: P21-P25. Details are given in Fig. 5.20). The measured lasing thresholds is plotted in Fig. 5.19(c). The variation in the lasing threshold is caused by the different degrees of EGFR expression (hence FITC concentration) in each cell nucleus. For comparison, it is difficult for conventional IF microscopy (Fig. 5.19(d)) to pinpoint the exact locations within the nucleus that have high EGFR concentrations. Similar to the YOPRO lasing case studied previously, with the laser emission significant improvement is achieved in the imaging contrast and the capability to locate the spots of high EGFR concentrations with a sub-micron resolution, as shown in Figs. 5.19(e) and (f).

With the sub-cellular lasing from n-EGFR achieved in Fig. 5.19, we now applied the LEM to distinguish the lung tissues with and without n-EGFR in Fig. 5.21. We prepared two types of lung cancer tissues, adenocarcinoma with n-EGFR (Tissue type #1) and adenocarcinoma without n-EGFR (Tissue type #2). All issues w well characterized and verified by pathologists (Fig. 5.20).

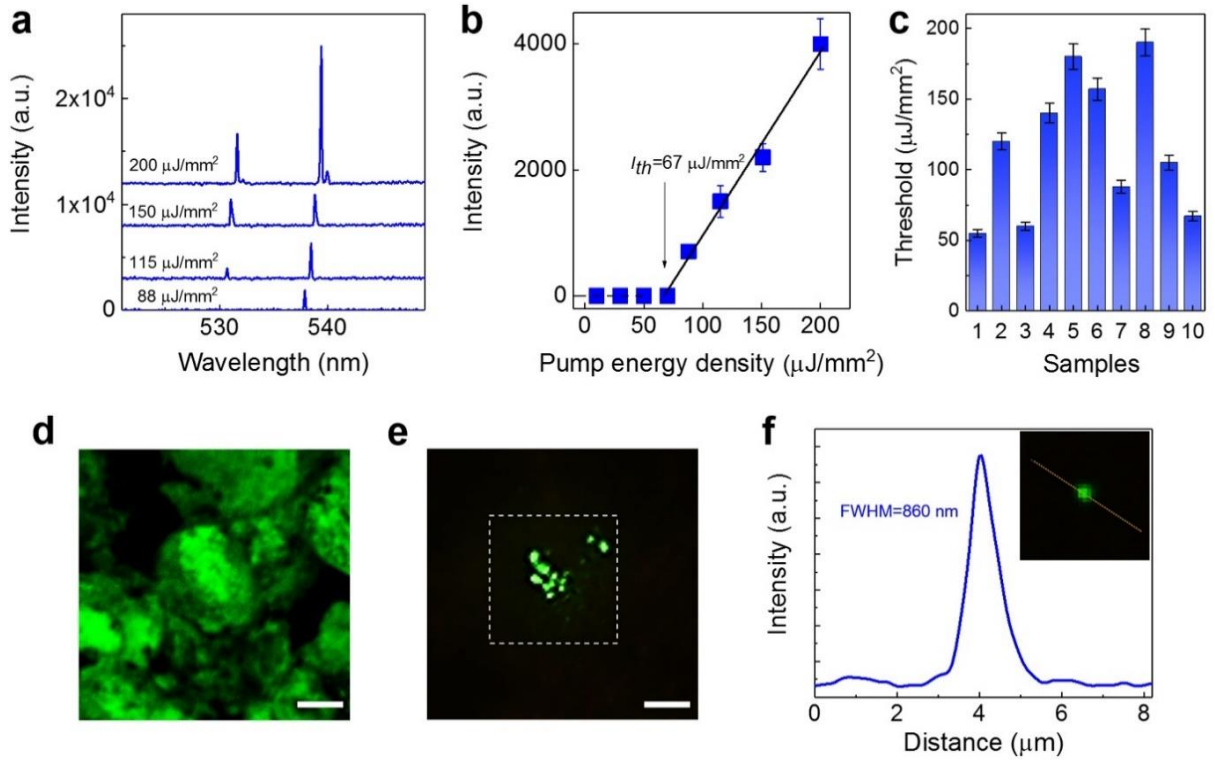

Figure 5.19. Lasing in lung cancer tissue with anti-EGFR-FITC. (a) Examples of lasing spectra of a human lung cancer tissue with n-EGFR expression stained with anti-EGFR-FITC under various pump energy densities. Curves are vertically shifted for clarity. (**b)** Spectrally integrated (530 nm – 540 nm) laser output as a function of pump energy density extracted from the spectra in (a). The solid lines are the linear fit above the lasing threshold, indicating a lasing threshold of 67 μJ/mm^2. **(c)** Histogram of n-EGFR-FITC lasing thresholds measured from 10 cells (samples) out of 5 lung cancer patients (patients P21-P25: including squamous cell carcinoma and andenocarcinoma tissues). The error bars (s.d.) in both (b) and (c) are defined by considering the pump energy density variation of OPO pulsed laser during the measurements. (**d)** Confocal microscopic image of a cell with n-EGFR expression in the lung cancer tissue. **(e)** CCD images of the laser output from the same lung cancer tissue above the lasing threshold (125 μJ/mm^2). The image shows clearly several "lasing stars" corresponding to the highest concentrated EGFR locations within the nuclei. The dashed square shows the laser pump beam area in LEM, which is focused on only one of the cells in the tissue. Note that (d) and (e) are not from the identical cells, but from the same piece of tissue. (**f)** The intensity profile along the yellow dotted line (inset) shows the FWHM is measured to be 860 nm. All the tissues were stained with anti-EGFR-FITC (0.5 mM in bulk staining solution) under the same preparation conditions. All scale bars, 10 μm.

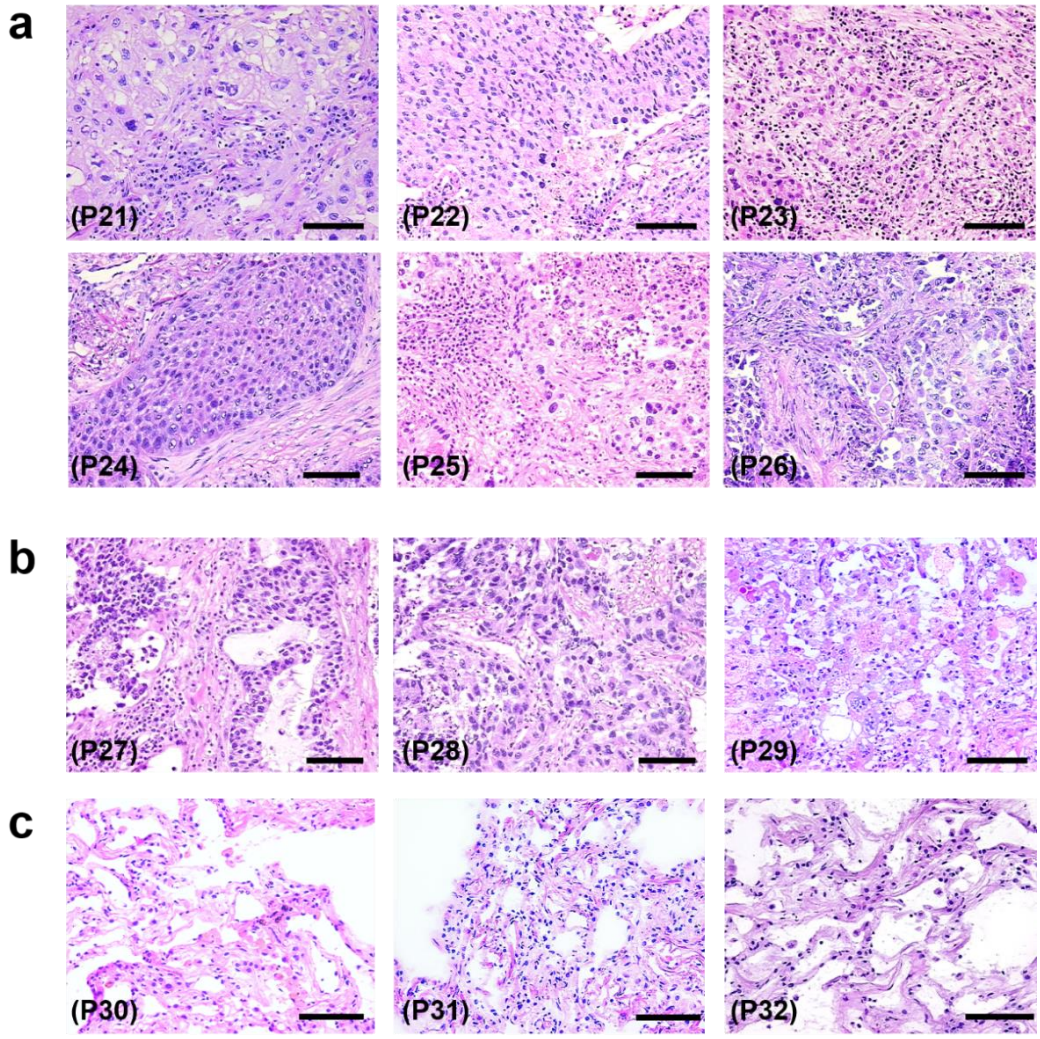

Figure 5.20. H&E images of the lung tissues used for immuno-laser experiment in Fig. 5.19. (**a**) Lung cancer patients diagnosed with nuclear-EGFR expression (P21-P23 stage I andenocarcinoma; P24-P25 stage I squamous cell carcinoma; P26: stage II andenocarcinoma). Only P26 show negative response for lasing, P21-P25 all have EGFR-FITC lasing. (**b**) Lung cancer patients diagnosed without nuclear-EGFR expression (P27-P29: stage I andenocarcinoma). (**c**) Normal lung tissues from healthy patients (P30-P32). All human lung tissue were examined and diagnosed by pathologists using IHC. All scale bars, 100 μm.

The exemplary lasing spectra of Type #1 (red curve) and Tissue #2 (blue curve) tissues when stained with anti-EGFR-FITC are shown in Fig. 5.21(a). As expected, laser emission at 537 nm is obtained in Tissue #1 with a pump energy density of 80 $\mu J/mm^2$; however, no lasing from Tissue #2 can be observed from the entire tissue when pumped with the same energy density. This result indicates that cells having EGFR expression only on the membranes or other cytoplasmic organelles are not capable to provide sufficient gain to lase due to relatively low abundance of EGFR (and hence FITC). To validate the above experiments, we examined a total of 12 human patients with 3 tissue sections from each patient, including 6 lung cancer patients with n-EGFR and 6 patients without n-EGFR (3 normal and 3 lung cancer diagnosed without n-EGFR). Details of the 12 patients are provided in Fig. 5.20, labeled as patient P21-P32. Among all the 6 patients with n-EGFR, 5 of them showed positive lasing emissions (P21-P25). For all normal patients (P30-P32) and those having lung cancer but without n-EGFR (P27-P29), none of them showed lasing emissions from anti-EGFR-FITC. The statistic results are plotted in 5.21(b). The corresponding IHC image of both types of tissues in 5.21(b) (right column) confirm that Type #1 tissue has a significant amount of EGFR within most cell nuclei, whereas Type #2 tissue does not have any EGFR expression within the cell nuclei (but does have EGFR expressed on the cell membrane).

In order to further confirm that FITC lasing is only from the expression of EGFR in the nucleus, co-localization of EGFR and nucleus lasing signals from sub-cellular locations is critical, which not only verifies the presence of n-EGFR in a nucleus but also makes it easier for computer-aided imaging processing in the future. To demonstrate co-localization, both Type #1 and Type #2 tissues were dual-stained with YOPRO and anti-EGFR-FITC (see Methods). It is apparent that we are unable to clearly determine the sub-cellular locations by their fluorescence, or distinguish the

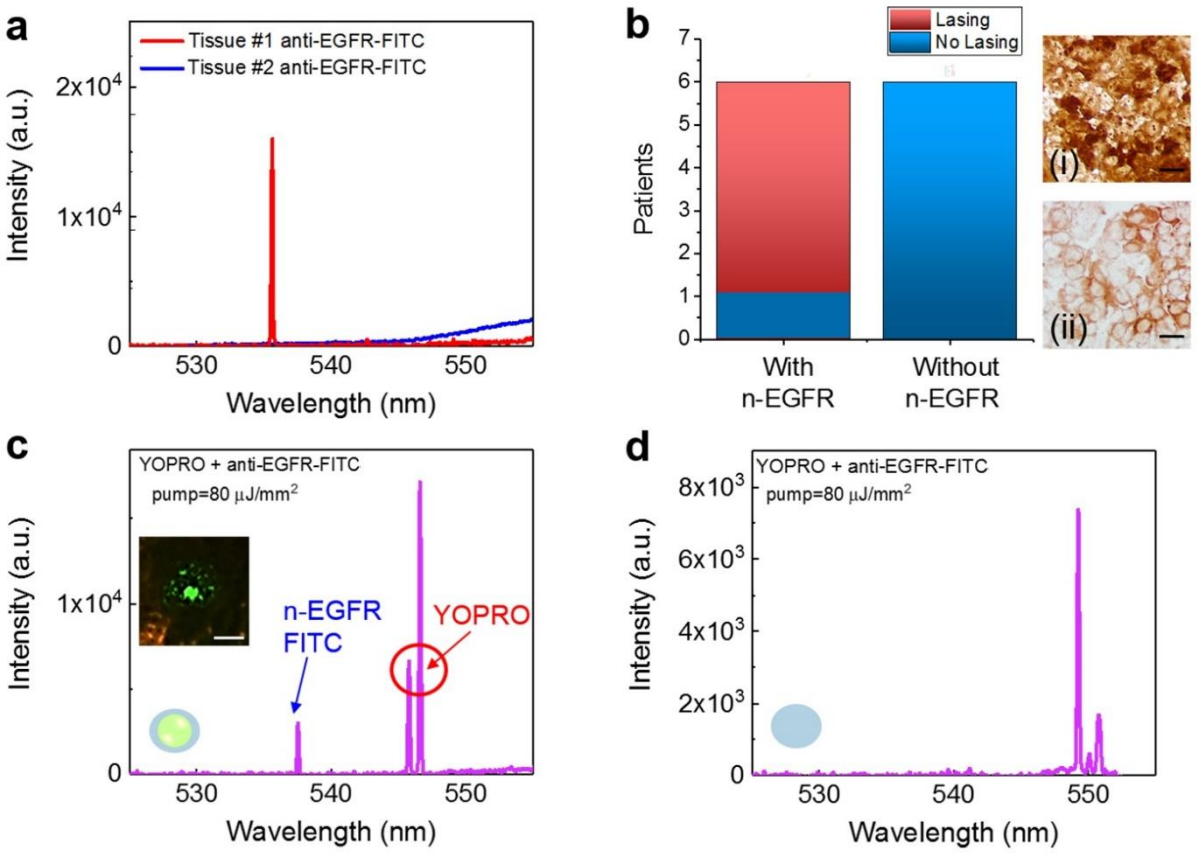

Figure 5.21. Multiplexed lasing in lung cancer tissues. (a) Lasing spectra of Type #1 (red curve) and Type #2 (blue curve) tissues stained with anti-EGFR-FITC. Pump energy density=80 μJ/mm². (**b)** Statistics of the EGFR lasing results for positive and negative n-EGFR lasing from 12 patients (P21-P32). Details and H&E images are provided in Fig. 5.20. (i) Brightfield IHC image of a human lung cancer tissue with n-EGFR (Tissue type #1). (ii) Brightfield IHC of a human lung cancer tissue without n-EGFR overexpression (Tissue type #2). (**c)** Lasing spectra of a Type #1 tissue dual-stained with YOPRO and EGFR-anti-FITC. The laser was focused on a single nucleus within the lung cancer tissue. The pump energy density was set above the threshold for both YOPRO and FITC under single excitation wavelength. The inset CCD image is the demonstration of a n-EGFR laser emission, which indicates that EGFR co-localizes with the nucleus. (**d)** Lasing spectra of a Type #2 tissue dual-stained with YOPRO and anti-EGFR-FITC. The laser was focused on a single nucleus within the lung cancer tissue. Note that the slight increase in the background emission beyond 550 nm in (a) and (c) is due to the fluorescence leaking out of the FP cavity caused by the reduced reflectivity of the dielectric mirror. Scale bars, 20 μm.

EGFR expressions in nucleus and cytoplasm, as a result of the huge spectral overlap between YOPRO and FITC (Fig. 5.22). In contrast, lasing signals of the two dyes can be observed and distinguished spectrally for Type #1 tissue. As shown in Fig. 5.21(c), two sharp lasing peaks appear at 537 nm and 547 nm when the tissue was pumped at the nucleus, which is the evidence of dual lasing from both EGFR and nucleic acids. The inset of Fig. 5.21(c) shows a CCD image, which confirms the presence of EGFR in the nucleus. Note that since the lasing threshold of FITC is much higher than that of for YOPRO, the lasing intensity from FITC is lower than that from YOPRO under the same pump energy density. Also note that even at higher pump energy densities at which higher order modes may emerge, the lasing spectra of YOPRO and FITC can still be distinguished due to their very narrow emission bands. As a negative control, for Type #2 tissue (Fig. 5.21(d)) only lasing spectrum from YOPRO was obtained when the tissue was pumped at the nucleus, no lasing signal from EGFR was observed, indicating that no EGFR or very low EGFR exists in the nucleus.

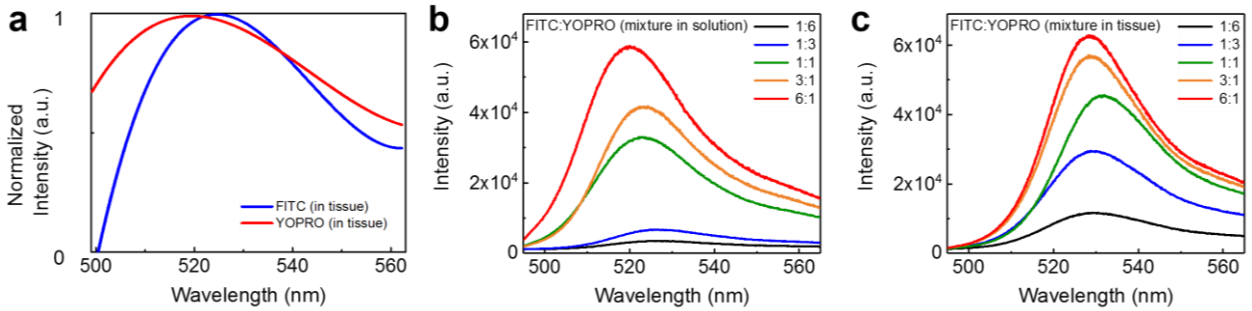

Figure 5.22. Fluorescence emission spectra of YOPRO and FITC. (a) Normalized fluorescence emission spectra of FITC (blue curve) and YOPRO (red curve) when they were used individually to stain the tissue. Huge spectral overlap (~100 nm) between the two dyes is obvious. **(b)** Significant fluorescence spectra of mixture solutions of FITC and YOPRO with various molar ratios. Note that YOPRO fluorescence emission can be detected only when it binds to nucleic acids. Therefore, the emission in (b) is predominantly from FITC. **(c)** Fluorescence spectra measured from lung cancer tissues by staining the tissues with the mixture solutions of FITC and YOPRO at various molar ratios. It is obvious that the fluorescence emission from FITC and YOPRO cannot be resolved. All pump energy density=30 μJ/mm^2. Excitation wavelength=465 nm.

5.4.7. Applications in colon cancer tissues

Finally, we applied the LEM to other types of tissues and proteomic biomarkers to validate its broad utility. In Fig. 5.23 we examined three different important cancer biomarkers (EGFR, p53 and Bcl-2) in human colon cancer tissues. For the purpose of tissue characterization, Figs. 5.23(a-c) present the IHC and confocal IF images of a colorectal cancer tissue labeled with the corresponding antibodies (i.e., anti-EGFR, anti-mutant p53, and anti-Bcl-2), showing a high amount of EGFR, p53 and Bcl-2 in the nuclei of the respective tissues. Similar to the procedures used previously, the lasing emissions from those colon tissues labeled with anti-EGFR-FITC, anti-mutant p53-FITC, and anti-Bcl-2-FITC were achieved in Figs. 5.23(d-f), when the nuclei were pumped. Our results show that lasing is achieved when there exist a high amount of biomarkers within the nuclei, which can be used for immunodiagnosis of various nuclear biomarkers. Despite the existence of multiple lasing peaks at the high pump energy density, the laser emission band is still approximately only 5 nm, showing the potential capability of multiplexed detection. The corresponding lasing threshold curves are presented in Figs. 5.24(a-c), showing that the lasing threshold is on the order of 200 $\mu J/mm^2$.

Besides cancer cells, the same technology can be extended to stroma cells (cancer-associated fibroblasts) that have overexpressed biomarkers. For example, Fig. 5.25 gives a lasing example using a colon tissue expressed with Bcl-2. Recent reports have revealed that the interaction between stromal cells and tumor cells plays a major role in cancer growth and progression[178]. Moreover, stromal gene expression have also demonstrated to define poor-prognosis subtypes in several cancers[179,180]. Therefore the capability to observe tumor stroma lasing will be of potential significance to predict clinical outcomes and strengthen clinical prognostic factors.

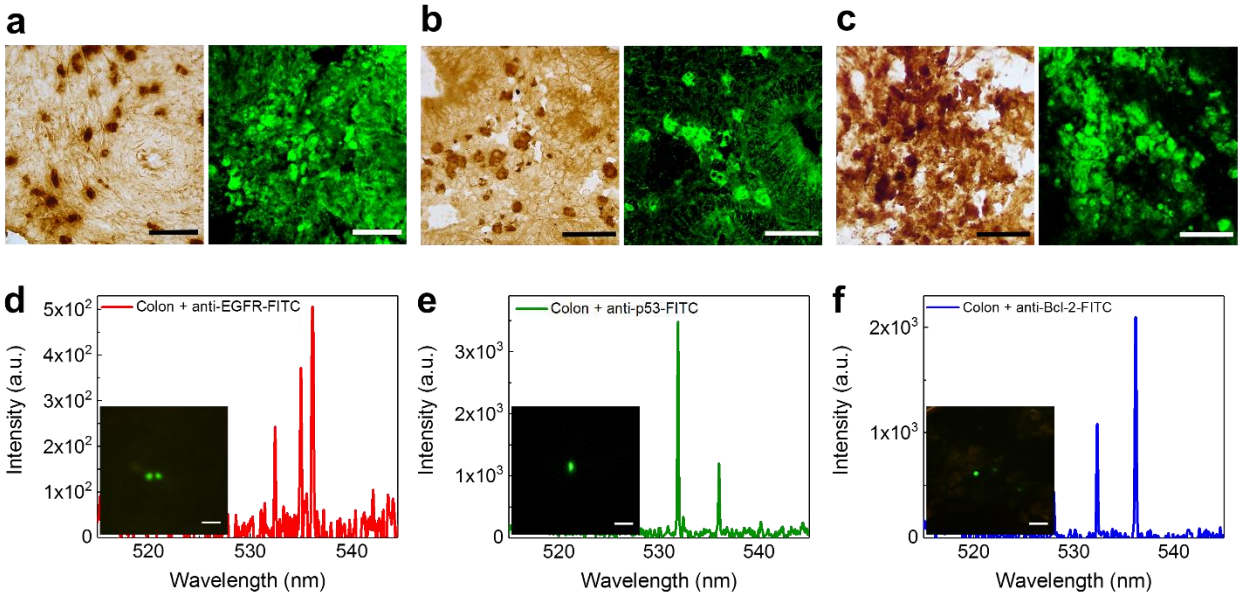

Figure 5.23. Lasing in colon cancer tissues with FITC conjugated antibodies. (a-c) Bright field IHC and confocal microscopic images of human colon cancer tissues with n-EGFR (**a**), n-p53 (**b**), and n-Bcl-2 (**c**) overexpression. (**d-f)** Lasing spectrum of colon cancer tissue prepared with anti-EGFR-FITC (**d**), anti-p53-FITC (**e**), and anti-Bcl-2-FITC (**f**). The insets in **d-f** shows the CCD image of representative "lasing stars" from the colon tissues when pumped at the nuclei. Pump energy density=220 μJ/mm^2, 280 μJ/mm^2, and 300 μJ/mm^2 for (d)-(f), respectively. Corresponding threshold plots can be found in Fig. 5.24. In total, 3 tissue samples from 3 different colon carcinoma patients (N=3) were used in (d-f). All scale bars for (a-c) 50 μm; (d-f) 5 μm.

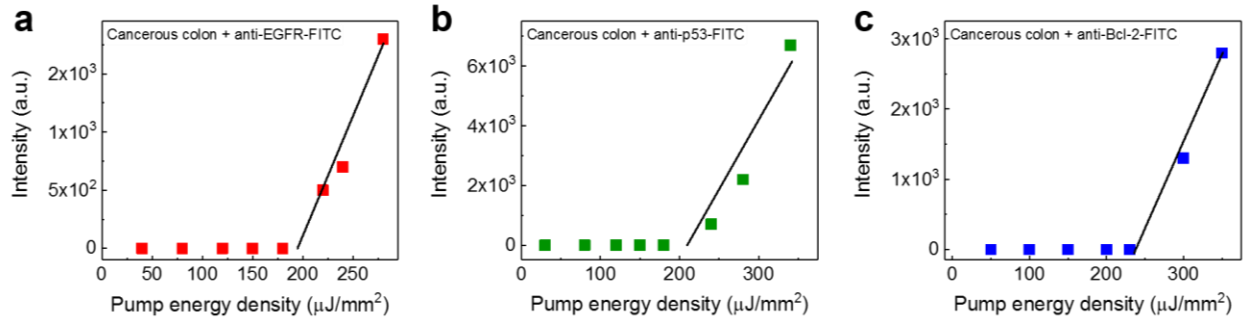

Figure 5.24. Lasing threshold of colon cancer tissue labeled with antibodies. Spectrally integrated (530 nm – 540 nm) laser output as a function of pump energy density for colon cancer tissue labeled with (**a**) anti-EGFR-FITC, (**b**) anti-mutant p53-FITC, and (**c**) anti-Bcl-2-FITC antibodies. The fitted lasing threshold is about 182 μJ/mm^2, 200 μJ/mm^2, and 230 μJ/mm^2 for **a**, **b**, and **c**, respectively. Solid lines show the linear fit above the threshold. Tissue thickness=15 μm. Excitation wavelength=465 nm.

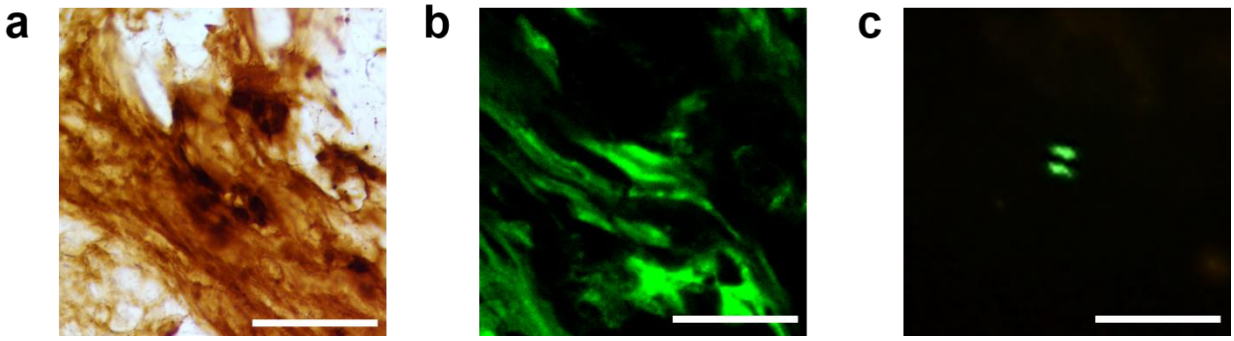

Figure 5.25. Lasing in tumor stroma. (**a)** IHC image of a colon cancer tissue labeled with anti-Bcl-2 antibodies, which shows high expression of Bcl-2 in the tumor stroma. (**b)** Confocal IF image of the colon stroma labeled with anti-Bcl-2-FITC. **(c)** CCD image showing two lasing stars from a stroma cell nucleus in a colon tissue. Note that (a-c) are not from the same cells, but from the same pieces of tissues. All scale bars, 50 μm.

5.5 Conclusion

In this chapter, we have developed a laser-emission based imaging tool (LEM) that takes advantage of the high intensity, high background suppression, and high spectral/spatial resolution of the laser emission. We have further tested its validity in early stage cancer diagnosis and evaluation of various nuclear biomarkers (nucleic acids, EGFR, p53, and Bcl-2) in human cancer tissues, which may significantly benefit the current clinical practice by providing complementary information that the conventional H&E, IHC, and IF are unable or difficult to obtain. Laser-emission-based cancer screening and immunodiagnosis might find use in precision medicine and facilitate research in cell biology.

As an outlook, below we discuss a few possible areas that deserve further exploration in the near future. (1) Conventional methods (H&E, IHC and IF) are known to be more subjective and may cause significant variations in tissue evaluation from one pathologist to another[166-168,181].

The LEM can potentially provide a means to quantify the number of sites within a cell that have different levels of biomarker expression and the number of cells that express high nuclear biomarkers. In Fig. 5.12, each lasing cell was counted only once even though there might be multiple lasing stars present inside the lasing cell. Despite this significantly simplified way of categorization, the LEM is already able to distinguish cancer and normal tissues. On the other hand, we have discussed that the lasing stars in cancer tissues may have different lasing thresholds due to different biomarker concentrations. By ramping the pump energy density, the histogram of the lasing stars with different thresholds can be constructed, which may allow us to sub-categorize the cancer tissue (e.g., in terms of severity and sensitivity to therapies). We will work closely with pathologists to develop algorithms that can make best use of this new information for more objective evaluation of cancer tissues. (2) Fundamentally, through the LEM we have found that there exist multiple sites within a nucleus that have high biomarker expressions. Further interdisciplinary collaboration is needed to elucidate mechanisms of the occurrence of those spots and how to make use of them in cancer diagnosis/prognosis.

(3) While dual detection (2-plexed detection) was achieved in this work, there is no doubt that the LEM platform is capable to accommodate more fluorophores. For instance, in Fig. 5.26(a) lasing emission from a third dye (high-affinity nucleic acid dye - SYTOX Blue) was achieved, which is centered on 500 nm with a band width less than 5 nm. Furthermore, we demonstrate that at least four lasing emission wavelengths can be clearly distinguished within the range of 500 nm – 550 nm in Fig. 5.26(b). In the future, high wavelength multiplexicity of the lasing emission will be explored for better characterization of cells and tissues.

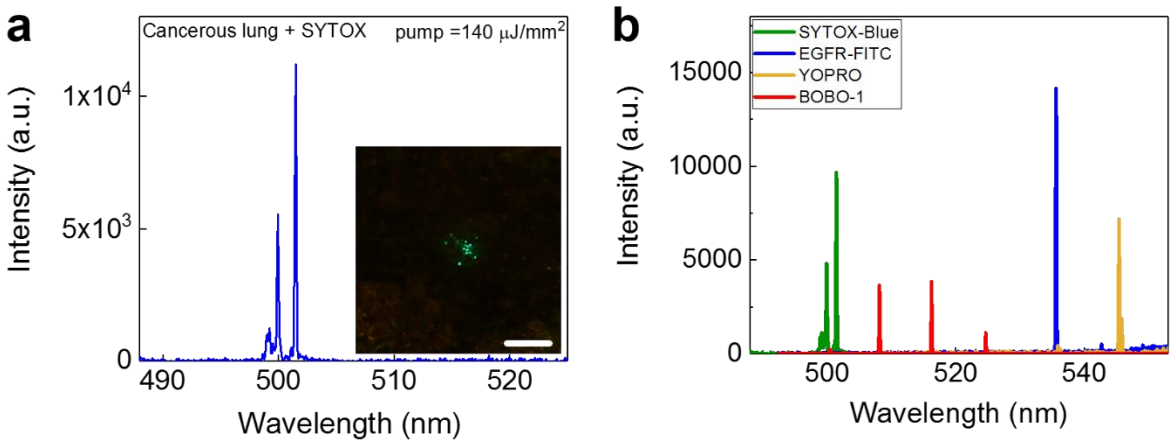

Figure 5.26. Four color multiplexed lasing in tissue. (a) Lasing spectra of lung cancer tissue labeled with 0.25 mM SYTOX Blue (SYTOX) nucleic acid dye. The inset shows the CCD image of lasing stars from several nuclei simultaneously. Pump energy density=140 μJ/mm^2. Scale bar, 40 μm. (**b)** Superposition of the lasing spectra of four dyes, SYTOX, BOBO-1 iodide, FITC (conjugated with EGFR), and YOPRO, shows multiple wavelength channels can be accommodated even within a 50 nm band, suggesting the possibility of highly wavelength-multiplexed detection using laser emission. Excitation wavelength=465 nm for all dyes.

Chapter 6

Monitoring Neuronal Activites and Networks with Neuron Lasers

So far in Chapter 2 to Chapter 5 we have demonstrated the potential applications of optofluidic lasers in various tissues. Finally, here in Chapter 6 we present an ongoing research work which will show potential for future monitoring of biological networks and tissues. Thus here we investigate the lasing properties of living cells in a biological network (multicellular network). This is particularly significant since cellular networks are the most fundamental formation of all tissues in living body. The ability to study the multicellular functions in networks will provide more insights for tissue engineering as well as the development of improved diagnostics and therapeutics. Therefore, here we used living neurons as an example to demonstrate lasing in neuronal networks (neuron lasers). Optical recording of calcium transients during spontaneous neuronal activities was demonstrated via "neuron lasers" with up to 1000-fold improvement in sensitivity. This work provides a novel approach to monitoring neuronal network dynamics and brain-on-chip neurophotonic applications.

6.1 Introduction

Calcium ions generate versatile intracellular signals that govern prevalent physiological processes and critical functions in several cell types, especially neurons[182]. For decades, calcium imaging has been a powerful approach to monitoring the calcium dynamics during neuronal activities in huge networks[183,184]. In particular, recent studies have revealed that spontaneous

calcium spikes have huge implications on neurological disorders, neuronal signaling, and brain circuits[185]. However, current techniques such as fluorescence-based measurements are not sufficiently sensitive to detect or monitor the extremely subtle changes in calcium concentrations, as the relative fluorescence change ($\Delta F/F$) is usually on the order of only 0.1[186,187]. Consequently, spontaneous neuronal activities are often missed as noise. A better ability to visualize spatial/temporal transients in cytosolic calcium levels resulting from spontaneous neuron activities will deepen and broaden our understanding of the pathophysiological mechanisms in neuroscience.

To date, laser emission from biological materials have demonstrated the distinct advantages over fluorescence, as described in the previous chapters. In particular, laser emission possesses the ability to amplify very subtle changes at the molecular level, leading to orders of magnitude increase in detection sensitivity and imaging contrast[6]. Taking advantage of such features, here we aim to detect the subtle Ca^{2+} concentration changes in live primary neurons by laser emissions. Lasing in neurons with a sub-cellular and single-spike resolution were explored to analyze the intracellular calcium dynamics during spontaneous neuronal activities *in vitro*. In addition, lasing from single isolated neurons and from neurons within a neuronal network were both recorded, showing 100-1000 times improvement in the sensing signal.

6.2. Experimental concept and design

Fig. 6.1(a) illustrates the concept of such a neuron laser, in which the primary cortical neurons labeled with Oregon Green BAPTA-1 (OGB-1) is sandwiched inside a Fabry-Pérot microcavity formed by two dielectric mirrors. The inset shows the fluorescence image of neurons stained with OGB-1 on top of a mirror. Microspheres (5 μm in diameter) were used as spacers to ensure the cavity length for cellular lasing. As illustrated in Fig. 6.1(b), the unique threshold behavior of the neuron laser can be explored for sensitive detection of spontaneous neuronal

activities. At the resting potential, no neuronal activity and hence no Ca^{2+} spiking occur. Therefore, the laser is operated below its threshold and only extremely weak background is observed. When a spontaneous spike occurs, the increase in Ca^{2+} concentration results in the emergence of the lasing emission. This sharp cut-off characteristic before and after lasing ensures orders of magnitude improvement in detection sensitivity.

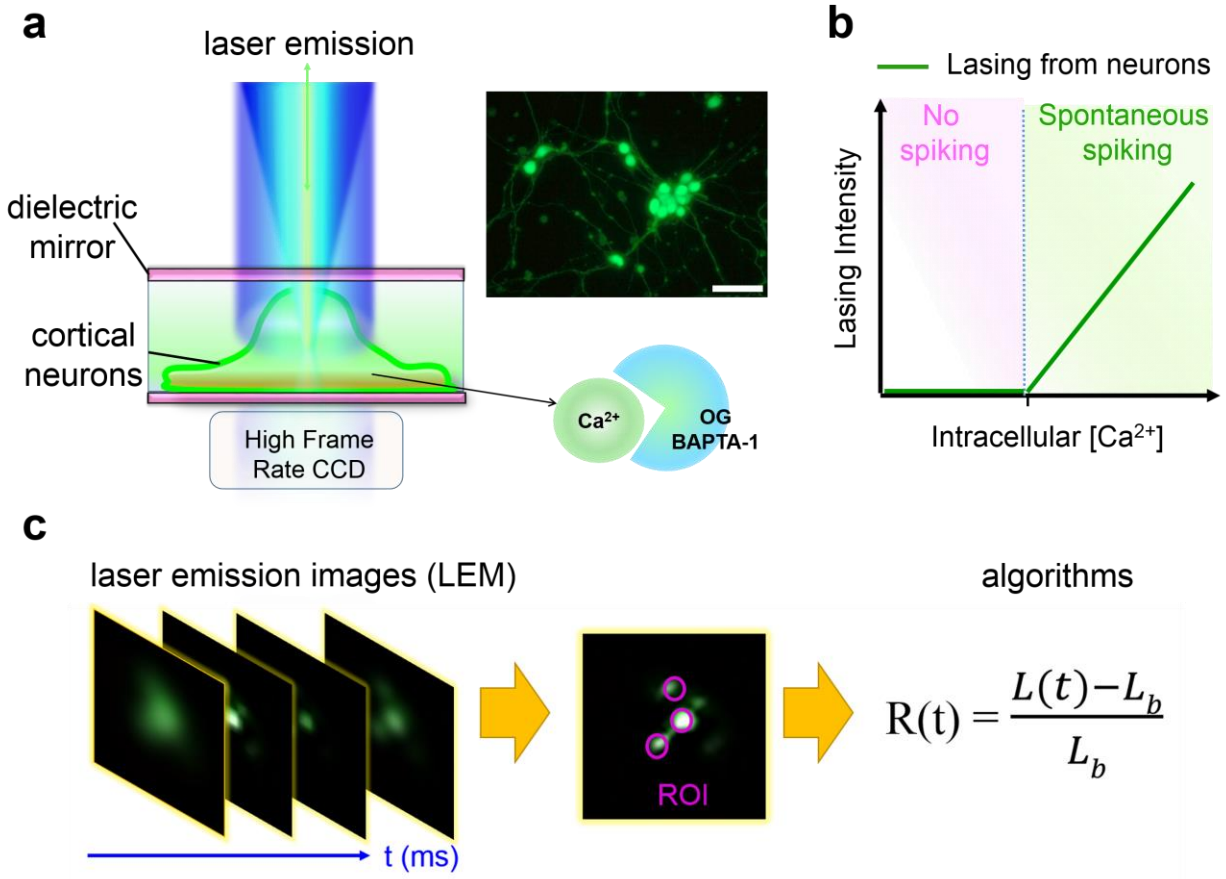

Figure 6.1. Concept of optical recording with neuron laser. (a) Schematic of the experimental configuration of a neuron laser. The inset shows the fluorescence image of OGB-1 labeled primary rat cortical neurons cultured on mirrors. Scale bar, 30 μm. **(b)** Output intensity from neuron lasers as a function of intracellular Ca^{2+} concentration. Under the fixed pump intensity, only when intracellular Ca^{2+} reaches above the baseline concentration (~50 nM) can the lasing emission start to emerge. **(c)** The protocol of image processing for monitoring neuronal activities. Different region of interest (ROI) were selected on the LEM images over a period of time, then calculated by the algorithms.

6.3. Materials and methods

For this particular research, primary cortical neurons from rat (Thermofisher #A15586) were selected as our model. The mirrors were first autoclaved and coated with poly-D-lysine and laminin (Sigma #127-2.5) for 30 mins, to ensure the cell growth and attachment. The cortical neurons were then cultured on top of the mirrors within cell culture medium (Thermofisher #21103049) and incubated at 37C for 3-5 days before further observation. The neurons were then stained with Oregon Green BAPTA-1 (OGB-1) by dissolving the OGB-1 AM ester in pluronic acid pluoronic-127 (in DMSO) to reach a final concentration of 25 uM in the culture medium. After incubation for 3 hours, the neurons were washed with PBS before measurements.

Optical recording of neurons was performed by collecting series of laser emission images from high speed CCD (frame rate of 5 fps). The optical setup is shown in Fig. 6.1(c). The recorded laser images over a series of time period were then transformed by equation:

$$\mathrm{R(t)} = \frac{L(t) - L_b}{L_b}$$

where L(t) is defined as the measured laser emission intensity from a certain ROI on the LEM image. R(t) is defined as the variation (relative changes) of laser emission intensity over a period of time. L_b is defined as the minimum laser emission intensity within the period of time, which is used as the baseline signal here. The algorithms was developed in *Python*, in which the baseline of the selected neuron emission is the minimum intensity within the time period. The intensity for each region of interests (ROI) is calculated by using the average intensity of the surrounding pixels (9 pixel in total) regarding the ROI. The excitation wavelength is 475 nm while using an OPO pump of 20 ns pulse width.

6.4. Results and discussion

6.4.1. Lasing with calcium indicators

OGB-1 is known as a calcium indicator and has higher fluorescence (or laser gain) in the presence of Ca^{2+}. The fluorescence emission spectra of OGB-1 with and without the presence of Ca^{2+} is shown in Fig. 6.2(a), in which the relative fluorescence change ($\Delta F/F$) is less than 0.1. As a comparison, the laser emission spectra of OGB-1 (pure dye) and OGB-1 with Ca^{2+} is plotted in Fig. 6.2(b). We can clearly see that no emission can be observed in pure OGB-1 (blue curve), however, a huge laser emission is generated when OGB-1 is mixed with Ca^{2+}. In contrast to Fig. 6.2(a), the relative intensity change is more than 100, which is 3 orders magnitude larger than conventional fluorescence. The amplification process of laser emission can thus be applied to monitor those subtle interactions of intracellular biomolecules in living cells. The corresponding spectrally integrated laser emission versus pump energy density presented in Fig. 6.2(c) shows the lasing threshold of approximate 120 $\mu J/mm^2$. To characterize the OGB-1 laser, in Fig. 6.2(d) we investigated the lasing threshold of pure OGB-1 (50 μM) mixed with various concentrations of free Ca^{2+}. Note that here in Fig. 6.2 we used this concentration to mimic neurons because the effective intracellular OGB-1 concentration in neurons is measured to be 50 μM in average during our staining process. It is shown that the lasing threshold increases with the decreased Ca^{2+} concentration, which is expected. In particular, a drastic difference in the lasing threshold can be seen when the Ca^{2+} concentration is in the range of 50 nM – 100 nM, which suggests that OBG-1 and its lasing emission can be used to monitor the subtle transients of spontaneous calcium spike activities, as the spontaneous Ca^{2+} concentration in neurons is within the same range of 50 nM – 100 nM[182].

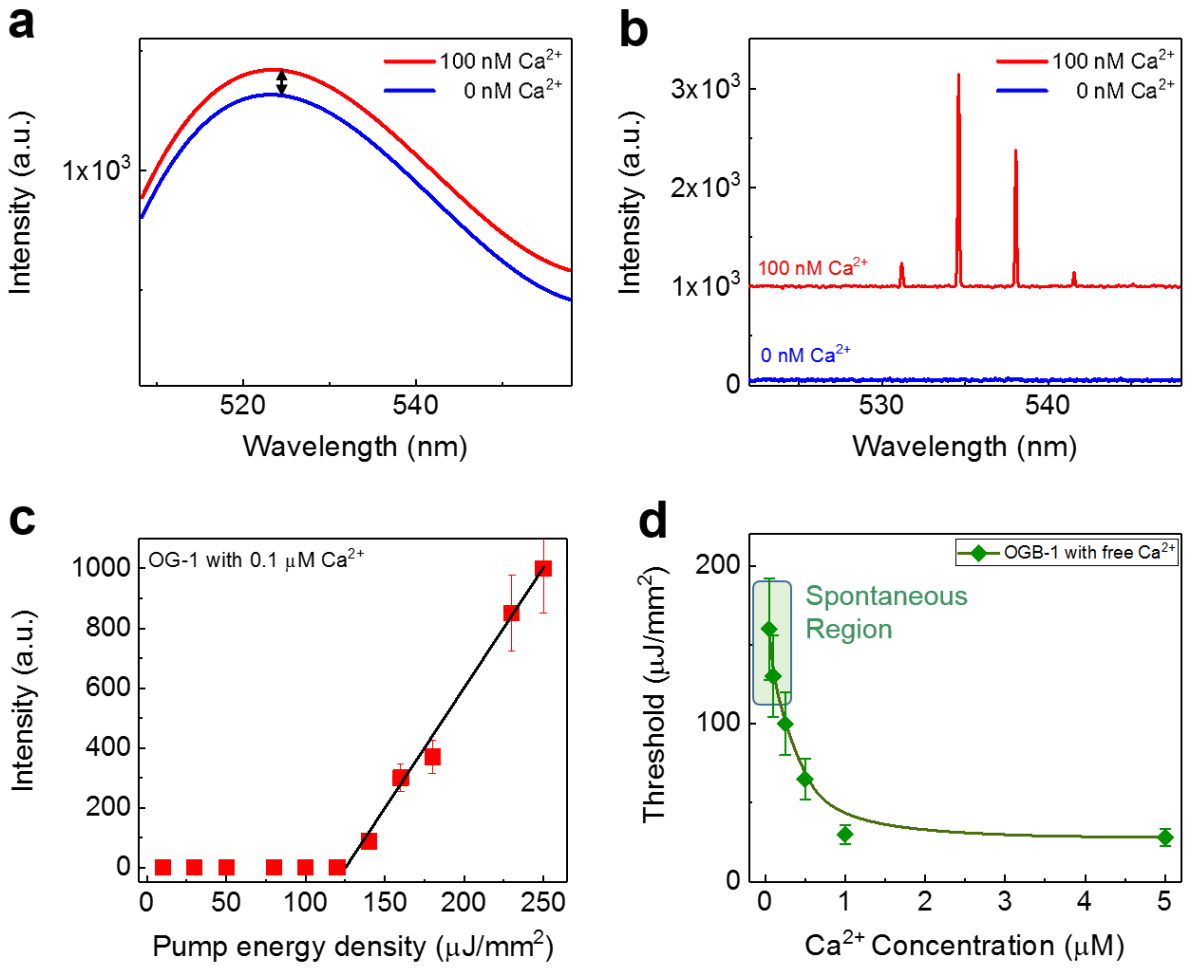

Figure 6.2. Lasing with calcium indicator OGB-1. (a) Fluorescence emission spectra of pure OGB-1 (blue curve) and OGB-1 mixed with 100 nM of free Ca^{2+} (red curve). **(b)** Lasing emission spectra of pure OGB-1 (blue curve) and OGB-1 mixed with 100 nM of free Ca^{2+} (red curve) under a pump energy density of 280 $\mu J/mm^2$. **(c)** Spectrally integrated (530 nm – 545 nm) laser output as a function of pump energy density extracted from the spectra in (b). The solid lines are the linear fit above the lasing threshold, indicating a lasing threshold of 120 $\mu J/mm^2$. **(d)** Lasing threshold calibration of pure dye (OGB-1) mixed with different free Ca^{2+} concentrations. The shaded green area depicts the spontaneous calcium spiking region (50-100 nM). The excitation wavelength is 475 nm while using an OPO pump of 20 ns pulse width.

6.4.2. Lasing in living neurons

In Fig. 6.3(a) we demonstrated for the first time, a "neuron laser" when the neuron was labeled with 25 μM OGB-1. A single mode lasing profile was first observed when the pump energy density is slightly above the lasing threshold. Multiple lasing modes emerge as the pump increases in Fig. 6.3(a). The inset shows an example of a bright field image of a single neuron with laser emissions within the cell soma. The corresponding spectrally integrated laser emission versus pump energy density presented in Fig. 6.3(b) shows the lasing threshold of approximate 150 $\mu J/mm^2$ for the neuron at the resting potential. As visualized by the CCD images in the inset of Fig. 6.3(b), no lasing was observed when the pump was below 150 $\mu J/mm^2$.

In contrast, sharp lasing emission emerges as the pump intensity increases, while the signal-to-background ratio is measured to be 500. Subcellular laser emissions can be observed only from specific sites in the neuron. Note that although the neuron in Fig. 6.3(a) was at the resting potential (no spontaneous Ca^{2+} spiking), the lasing emission could still be obtained at relatively high pump energy densities (i.e., >150 $\mu J/mm^2$). However, the lasing threshold is expected to be much lower when the neuron undergoes spiking or firing behaviors. Furthermore, we investigated the spatial resolution of such neuron laser images in Fig. 6.3 (c). The inset shows that lasing emission could be achieved from both the soma and dendrites of neuron, while the FWHM was measured to be approximately 950 nm.

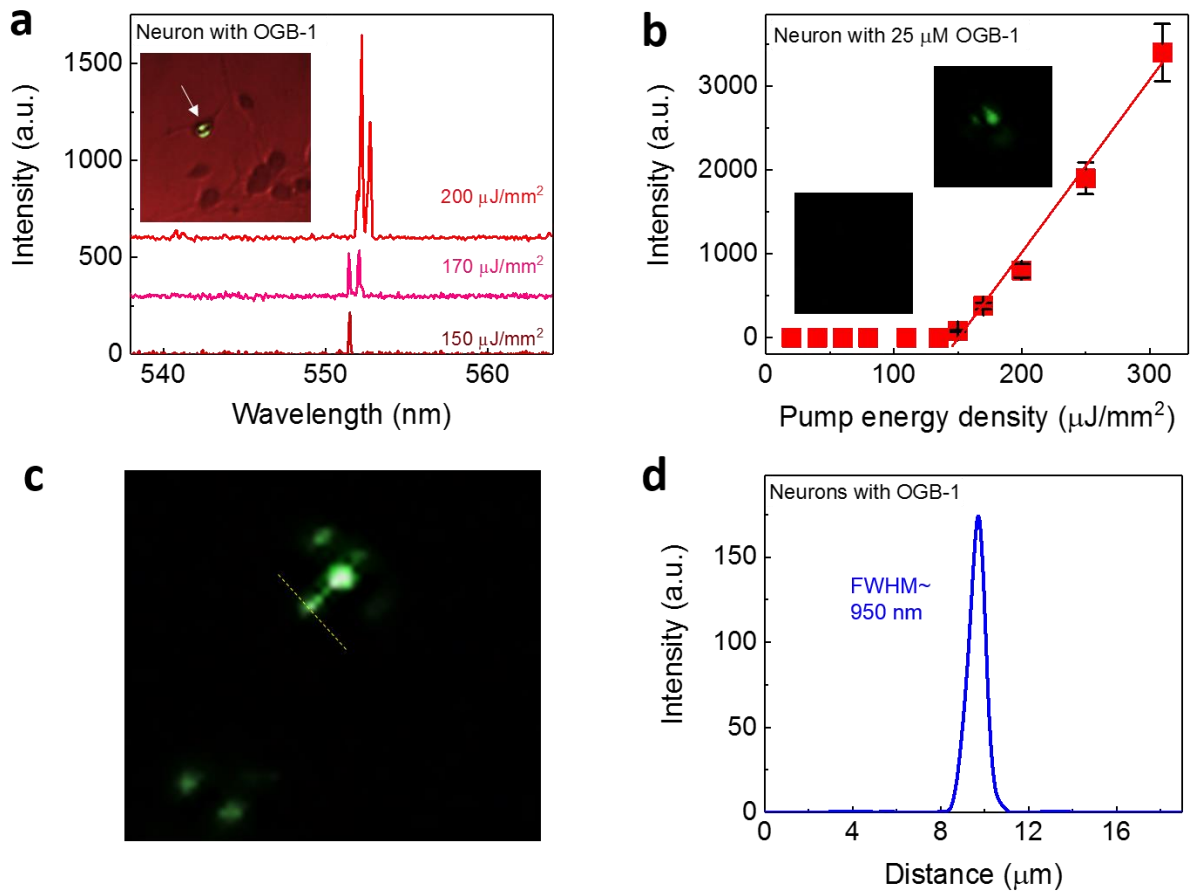

Figure 6.3. Lasing in living neurons. (a) Lasing spectra from a single neuron in vitro labeled with 25 μM OGB-1 under various pump energy densities at the resting potential. The inset shows the bright field a CCD image of a single neuron with sub-cellular laser emissions in the soma, as indicated by the arrow. **(b)** Spectrally integrated laser output as a function of pump energy density extracted from (a). The solid lines are the linear fit above the lasing threshold, indicating a lasing threshold of 150 μJ/mm^2. **(c)** CCD image of laser emissions from neurons. The dashed line measures the lasing profile over a single dendrite. **(d)** The FWHM of extracted from the dashed line in (c), which gives a submicron resolution of 950 nm.

6.4.3. Calcium imaging of spontaneous neuronal activity

Moving forward, here we aim to demonstrate optical recording/imaging of intracellular spontaneous calcium signals in neurons by using neuron laser emissions. As such, the pump energy density was fixed at 150 μJ/mm^2. As discussed previously, at the resting potential, no lasing

emission would be observed. However, with the spontaneous neuronal activities, calcium spikes occur, resulting in the emergence of lasing emission. The laser emission CCD images of a single isolated neuron is shown in the inset of Fig. 6.4(a). The calcium transients of individual neuron caused by spontaneous soma activity was recorded over 90 seconds, as plotted in Fig. 6.4(a). Significantly, the relative changes in lasing intensity (ΔL/L), where L is defined as the baseline intensity before lasing and ΔL is the lasing emission intensity above the background, ranges from 20 to 50, >100-fold improvement over the traditional fluorescence based measurement. In order to validate that all the CCD images recorded are from lasing emissions, we selected two representative signals at 48s and 82s, as plotted in Figs. 6.4(b) and (c), respectively.

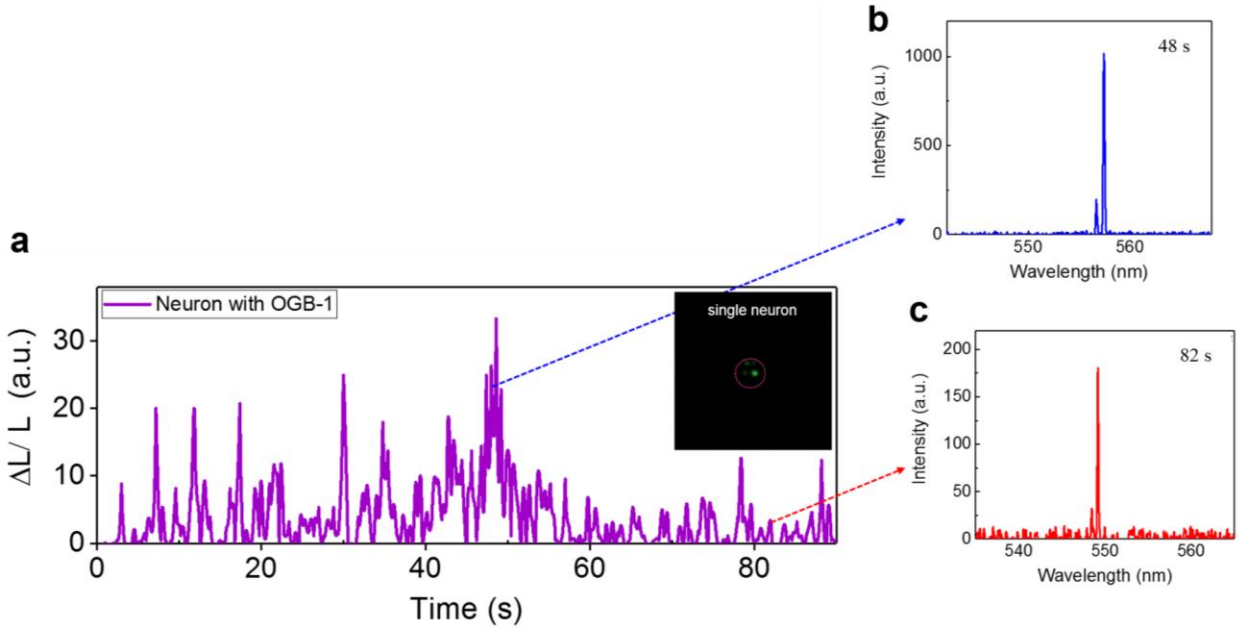

Figure 6.4. Optical recording of spontaneous activity in single neuron. (a) Optical recording of calcium transients caused by spontaneous neuronal activity over 90 seconds measured from neuron. The inset shows the CCD image of laser emission from a single neuron. **(b)** Lasing spectrum measured at 48 sec. **(c)** Lasing spectrum measured at 82 sec. The red shift of lasing peak wavelength is highly the result of Ca^{2+} concentration variation within the neuron soma.

6.4.4. Biologically controlled lasing in neuronal networks

Finally, lasing in neuronal networks was achieved. Based on the similar protocols, the calcium transients of neurons within a neuronal network was recorded and analyzed. Two types of intra-cellular interactions are presented here in Fig. 6.5, resulting in significant changes in neuron laser output. First, as shown in Fig. 6.5(a), the CCD image (left) clearly shows the laser emissions of three individual neurons (n1, n2, and n3). The calcium transients of neurons in neuronal networks were recorded simultaneously in Fig. 6.5(b), in which the $\Delta L/L$ can be as high as 100 due to the recurring stimuli and interactions among neurons. The time traces also show correlation between n1, n3, and n3 in calcium spikes. Secondly, another example is given in Fig. 6.6(a), the calcium transients of neurons (n1 and n2) in neuronal networks were recorded simultaneously. According to the two inset CCD images in Fig. 6.6(a), we can clearly see that only n1 show significant lasing emissions at 22s (blue trace), while n2 is completely dark with no lasing signal. Conversely, only n2 show lasing emissions at 32 s (red trace), while n1 turns completely dark and no lasing is observed. This is the result of interactions (energy transfer) between two neurons, suggesting that neuron lasers can be biologically switched on/off based on intercellular calcium dynamics. In order to validate that all the CCD images recorded are from lasing emissions, we selected two representative signals at 22 s (blue curve) and 32s (red curve), as plotted in the inset spectra of Fig. 6.6(b), respectively.

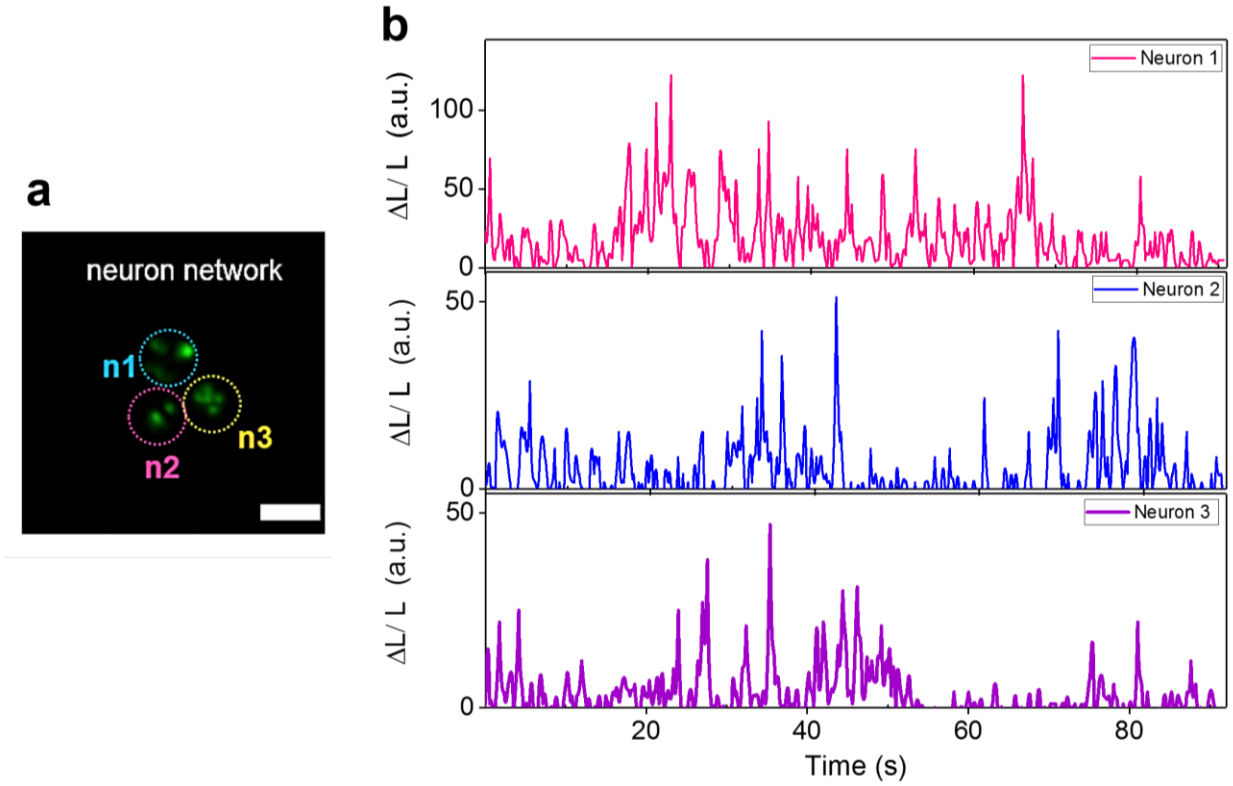

Figure 6.5. Optical recording in neuronal networks. (a) CCD image of laser emission from a neuron network formed by 3 neurons (n1, n2, and n3). **(b)** Optical recording of calcium transients caused by spontaneous neuronal activity over 90 seconds measured from neuron-n, neuron-n2, and neuron-n3 in (a). Scale bar, 15 μm.

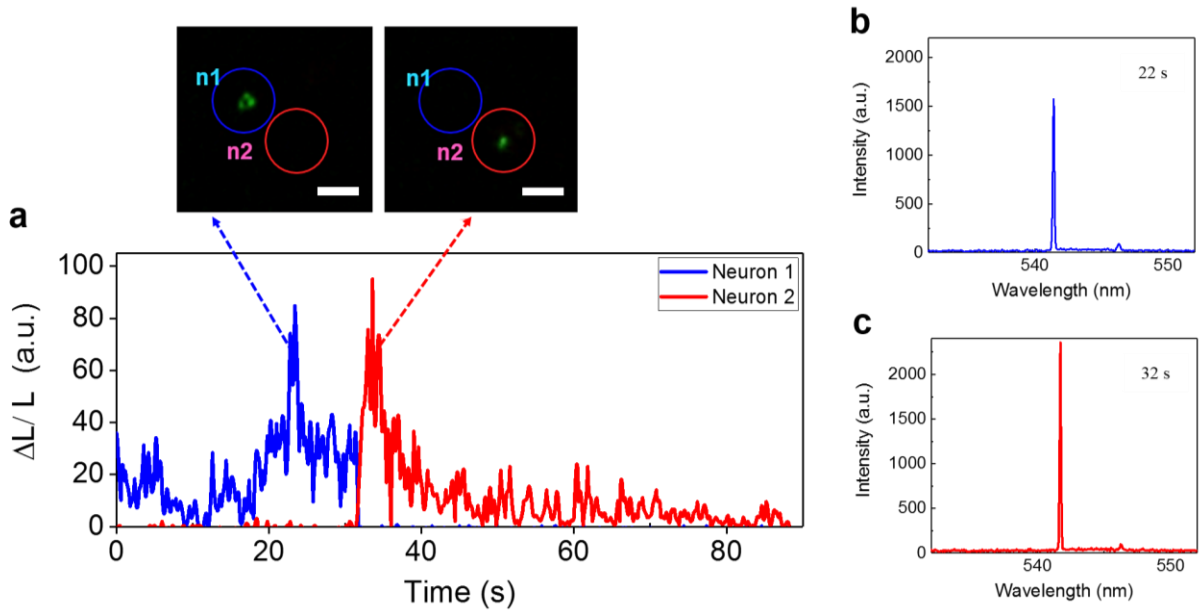

Figure 6.6. Interactions of neuron lasers in neuronal network. (a) Optical recording of calcium transients caused by spontaneous neuronal activity over 90 seconds measured from neuron-n1 and neuron-n2 in a network. The above CCD images show the laser emission switching between two neurons (n1 and n2). **(b)**. Lasing spectrum measured at 22 sec from n1. **(c)**. Lasing spectrum measured at 32 sec from n2. Scale bars, 15 μm.

6.5. Conclusion

For the first time, we demonstrated a neuron laser and employed laser emission to detect the subtle transients of intracellular calcium dynamics in neurons *in vitro*. Lasing in single neuron and neuronal networks were biologically controlled by spontaneous neuronal activities. Calcium imaging and recording of spontaneous neuronal spike activities were demonstrated, in which the relative changes (ΔL/L) were significantly improved 100-1000 fold in comparison with that obtained by fluorescence based measurement. Highly interaction and correlation between neurons also resulted in complex lasing emission spikes. Our work not only opens the door to optical recording of intracellular dynamics in neuronal networks, but provides an ultra-sensitive detection method for brain-on-chip applications and neuro-analysis.

Chapter 7

Summary and Outlook

In this dissertation, we have successfully developed the first biolasers at the tissue level by using different micro-cavities and several types of tissues. Furthermore, we evidently demonstrated that the proposed tissue lasers can be applied to a variety of tissues to differentiate various diseases and cancers for future clinical applications. Our work represents a critical milestone to implement optofluidic lasers in tissues, which opens a door to a plethora of applications in bioimaging and biosensing with superior contrast and high spectral/spatial resolution.

In contrast to conventional fluorescence, the laser output from tissues provides a number of optical parameters unseen in fluorescence, such as the lasing threshold of various biomarkers, lasing mode spatial distribution, lasing mode competition, and lasing gain clamping. We will conduct further investigations to understand how those parameters reflect the underlying biological and physiological processes of cancerous tissues as well as to achieve better spectral and spatial resolution. Other potential applications will also be explored, including, but are not limited to, Pap smear stain examination, intraoperative image-guided neurosurgery and tumor resection, and Fluorescence In-Site Hybridization (FISH). Technically, currently the FP tissue laser is operated in a multi-mode regime. While the lasing emission band is much narrower than that in fluorescence, it is still about 10 nm wide, which limits multiplexing capability. Eventually a single-mode tissue

laser will be pursued using either shorter cavity length or external optical feedback, in which case the lasing band can be far below 1 nm (currently 0.2 nm, limited by the spectrometer resolution).

However, there are a few challenges which needs to overcome in the future. First, advanced design of biocompatiable and wearable laser cavity is required to develop *in vivo* lasing experiments in animals and human. The current setup does not allow to perform *in vivo* sensing; however, by using spasers or distributed feedback lasers, we may possible to achieve that in the future. Secondly, 3D information and z-sectioning is very important for tissue imaging while laser emission only provides a stacked information of the tissue. By using fiber-probes, we may be able to render or map the cells in different directions to gain the 3D insights. Thirdly, laser requires the fluorophore to reach a certain concentration in order to overcome the threshold; however, the sites with very low concentrations may be dismissed when below the lasing threshold. As such, the development of higher-Q factor device is required in order to enhance the sensitivity and dynamic range for future laser-based detection.

Last but not the least, we envision that this study will have significant impact in the following areas. (1) It will provide a new and powerful platform technology, which is complementary to conventional fluorescence based methods, for cell analysis and tissue analysis, both *in vitro* and *in vivo*. (2) The optofluidic laser based detection principle and protocol developed in this research are broadly applicable to any laser cavities and any bio-species, and therefore, will lead to the development of novel on-chip devices for future clinical diagnosis, prognosis, and therapy. (3) Beyond biology and biomedicine, the study of the optofluidic tissue lasers will provide in-depth understanding of how light interacts with living organisms and biological materials, which will be significant for the development of novel bio-control photonic devices such as bio-

controllable optofluidic lasers, DNA optical switches, DNA computation, and optofluidic photosynthesis systems.

Bibliography

1 Li, Z. & Psaltis, D. Optofluidic dye lasers. *Microfluid. Nanofluid.* **4**, 145–158 (2007).

2 Lee, W. *et al.* A quasi-droplet optofluidic ring resonator laser using a micro-bubble. *Appl. Phys. Lett.* **99**, 091102 (2011).

3 Lee, W. *et al.* Tunable single mode lasing from an on-chip optofluidic ring resonator laser. *Appl. Phys. Lett.* **98**, 061103 (2011).

4 Chen, Y. *et al.* Optofluidic microcavities: Dye-lasers and biosensors. *Biomicrofluidics* **4**, 043002 (2010).

5 Monat, C., Domachuk, P. & Eggleton, B. J. Integrated optofluidics: A new river of light. *Nature Photon.* **1**, 106-114 (2007).

6 Fan, X. & Yun, S.-H. The potential of optofluidic biolasers. *Nat. Methods* **11**, 141-147 (2014).

7 He, L., Özdemir, Ş. K. & Yang, L. Whispering gallery microcavity lasers. *Lasers Photon. Rev.* **7**, 60-82 (2013).

8 Wang, W. *et al.* Optofluidic laser array based on stable high-Q Fabry-Perot microcavities. *Lab Chip* **15**, 3862-3869 (2015).

9 Wu, X. *et al.* Optofluidic laser for dual-mode sensitive biomolecular detection with a large dynamic range. *Nature Commun.* **5**, 3779 (2014).

10 Vannahme, C., Maier-Flaig, F., Lemmer, U. & Kristensen, A. Single-mode biological distributed feedback laser. *Lab Chip* **13**, 2675-2678 (2013).

11 Ta, V. D., Caixeiro, S., Fernandes, F. M. & Sapienza, R. Microsphere Solid ‐ State Biolasers. *Adv. Opt. Mater.* **5** (2017).

12 Christiansen, M. B., Kristensen, A., Xiao, S. & Mortensen, N. A. Photonic integration in k-space: Enhancing the performance of photonic crystal dye lasers. *Appl. Phys. Lett.* **93**, 231101 (2008).

13 Chen, Y. *et al.* Colloidal quantum dot random laser. *Opt. Express* **19**, 2996-3003 (2011).

14 Wu, X., Chen, Q., Sun, Y. & Fan, X. Bio-inspired optofluidic lasers with luciferin. *Appl. Phys. Lett.* **102**, 203706 (2013).

15 Nizamoglu, S., Gather, M. C. & Yun, S. H. All-Biomaterial Laser using Vitamin and Biopolymers. *Adv. Mater.* **25**, 5943-5947 (2013).

16 Li, Z. & Psaltis, D. Optofluidic dye lasers. *Microfluid. Nanofluid.* **4**, 145-158, doi:10.1007/s10404-007-0225-9 (2008).

17 Jonáš, A. *et al.* In vitro and in vivo biolasing of fluorescent proteins suspended in liquid microdroplet cavities. *Lab Chip* **14**, 3093-3100 (2014).

18 Chen, Q. *et al.* Highly sensitive fluorescent protein FRET detection using optofluidic lasers. *Lab Chip* **13**, 2679-2681 (2013).

19 Gather, M. C. & Yun, S. H. Bio-optimized energy transfer in densely packed fluorescent protein enables nearmaximal luminescence and solid-state lasers. *Nature Commun.* **5**, 5722 (2014).

20 Chen, Q., Kiraz, A. & Fan, X. Optofluidic FRET lasers using aqueous quantum dots as donors. *Lab Chip* **16**, 353-359 (2016).
21 Shopova, S. I., Farca, G., Rosenberger, A. T., Wickramanayake, W. M. S. & Kotov, N. A. Microsphere whispering-gallery-mode laser using HgTe quantum dots. *Appl. Phys. Lett.* **85**, 6101-6103 (2004).
22 Levy, U., Campbell, K., Groismanb, A., Mookherjea, S. & Fainman, Y. On-chip microfluidic tuning of an optical microring resonator. *Appl. Phys. Lett.* **88**, 111107 (2006).
23 Zhang, X., Lee, W. & Fan, X. Bio-switchable Optofluidic Lasers Based on DNA Holliday Iunctions. *Lab Chip* **12**, 3673-3675 (2012).
24 Erickson, D., Rockwood, T., Emery, T., Scherer, A. & Psaltis, D. Nanofluidic tuning of photonic crystal circuits. *Opt. Lett.* **31**, 59-61 (2006).
25 Li, Z., Zhang, Z., Emery, T., Scherer, A. & Psaltis, D. Single mode optofluidic distributed feedback dye laser. *Opt. Express* **14**, 696-701 (2006).
26 Wu, X. *et al.* Optofluidic laser for dual-mode sensitive biomolecular detection with a large dynamic range. *Nature Commun.* **5**, 3779 (2014).
27 Sun, Y. & Fan, X. Distinguishing DNA by Analog-to-Digital-like Conversion by Using Optofluidic Lasers. *Angew. Chem. Int. Ed.* **51**, 1236-1239 (2012).
28 Cho, S., Humar, M., Martino, N. & Yun, S. H. Laser Particle Stimulated Emission Microscopy. *Phys. Rev. Lett.* **117**, 193902 (2016).
29 Chen, Y.-C., Chen, Q., Zhang, T., Wang, W. & Fan, X. Versatile tissue lasers based on high-Q Fabry–Pérot microcavities. *Lab Chip* **17**, 538-548 (2017).
30 Chen, Y.-C., Chen, Q. & Fan, X. Lasing in blood. *Optica* **3**, 809-815 (2016).
31 Ozdemir, S. K. *et al.* Highly sensitive detection of nanoparticles with a self-referenced and self-heterodyned whispering-gallery Raman microlaser. *Proc. Natl. Sci. Acad. USA* **111**, E3836–E3844 (2014).
32 Bog, U. *et al.* On-chip microlasers for biomolecular detection via highly localized deposition of a multifunctional phospholipid ink. *Lab Chip* **13**, 2701–2707 (2013).
33 Chen, Q. *et al.* Self-assembled DNA tetrahedral optofluidic lasers with precise and tunable gain control. *Lab Chip* **13**, 3351-3354 (2013).
34 Zhang, X., Lee, W. & Fan, X. Bio-switchable optofluidic lasers based on DNA Holliday junctions. *Lab Chip* **12**, 3673-3675, doi:10.1039/c2lc40183e (2012).
35 Gather, M. C. & Yun, S. H. Single-cell biological lasers. *Nature Photon.* **5**, 406-410 (2011).
36 Humar, M. & Yun, S. H. Intracellular microlasers. *Nature Photon.* **9**, 572-576 (2015).
37 Humar, M., Gather, M. C. & Yun, S.-H. Cellular dye lasers: lasing thresholds and sensing in a planar resonator. *Opt. Express* **23**, 27865-27879 (2015).
38 Gourley, P. L. Biocavity laser for high-speed cell and tumour biology. *J. Phys. D: Appl. Phys.* **36**, R228 (2003).
39 Gourley, P. *et al.* Ultrafast Nanolaser Flow Device for Detecting Cancer in Single Cells. *Biomed. Microdevices* **7**, 331-339 (2005).
40 Gourley, P. L. & Naviaux, R. K. Optical phenotyping of human mitochondria in a biocavity laser. *IEEE J. Sel. Top Quantum Electron.* **11**, 818-826 (2005).
41 Song, Q. *et al.* Random lasing in bone tissue. *Opt. Lett.* **35**, 1425-1227 (2010).
42 Polson, R. C. & Vardeny, Z. V. Random lasing in human tissues. *Appl. Phys. Lett.* **85**, 1289-1291 (2004).
43 Choi, S. H. & Kim, Y. L. The Potential of Naturally Occurring Lasing for Biological and Chemical Sensors. *Biomed. Eng. Lett.* **4**, 201-212 (2014).

44 Wu, X., Sun, Y., Suter, J. D. & Fan, X. Single mode coupled optofluidic ring resonator dye lasers. *Appl. Phys. Lett.* **94**, 241109 (2009).
45 Helbo, B., Kristensen, A. & Menon, A. A micro-cavity fluidic dye laser. *J. Micromech. Microeng.* **13**, 307–311 (2003).
46 Kou, Q., Yesilyurt, I. & Chen, Y. Collinear dual-color laser emission from a microfluidic dye laser. *Appl. Phys. Lett.* **88**, 091101, doi:10.1063/1.2179609 (2006).
47 Aubry, G., Méance, S., Haghiri-Gosnet, A.-M. & Kou, Q. Flow rate based control of wavelength emission in a multicolor microfluidic dye laser. *Microelectron. Eng.* **87**, 765-768 (2010).
48 Aubry, G. *et al.* A Multicolor Microfluidic Droplet Dye Laser with Single Mode Emission. *Appl. Phys. Lett.* **98**, 111111 (2011).
49 Gather, M. C. & Yun, S. H. Single-cell biological lasers. *Nature Photon.* **5**, 406-410, doi:10.1038/nphoton.2011.99 (2011).
50 Gather, M. C. & Yun, S. H. Lasing from Escherichia coli bacteria genetically programmed to express green fluorescent protein. *Opt. Lett.* **36**, 3299-3301 (2011).
51 Kuehne, A. J. C. *et al.* A switchable digital microfluidic droplet dye-laser. *Lab Chip* **11**, 3716-3719 (2011).
52 Chen, Y.-C., Chen, Q. & Fan, X. Optofluidic chlorophyll lasers. *Lab Chip* **16**, 2228-2235 (2016).
53 Chen, Y.-C. *et al.* Laser-emission imaging of nuclear biomarkers for high-contrast cancer screening and immunodiagnosis. *Nature Biomedical Engineering* **1**, 724-735 (2017).
54 Sun, X., Feng, P., Xu, X., Guo, H., Ma, J., Chi, et al. A chloroplast envelope-bound PHD transcription factor mediates chloroplast signals to the nucleus. *Nat. Commun.* **2** (2011).
55 Jarvis, P. L.-J., E. Biogenesis and homeostasis of chloroplasts and other plastids. *Nat. Rev. Mol. Cell Biol.* **14**, 787-802 (2013).
56 Azzi, W. A. a. J. R. chlorophyll energy levels and electron flow in photosynthesis. *Proc. Natl. Acad. Sci.* **61** (1968).
57 Adhyaksa, G. W. P., Prima, E. C., Lee, D. K., Ock, I., Yatman, S., Yuliarto, B., & Kang, J. K. A Light Harvesting Antenna Using Natural Extract Graminoids Coupled with Plasmonic Metal Nanoparticles for Bio‐Photovoltaic Cells. *Adv. Energy Matter*. **4** (2014).
58 Parusel, A. B., & Grimme, S. A theoretical study of the excited states of chlorophyll a and pheophytin a. *J. Phys. Chem.* **104**, 5395-5398. (2000).
59 De Boni, L., Correa, D. S., Pavinatto, F. J., dos Santos, D. S., & Mendonca, C. R. Excited state absorption spectrum of chlorophyll a obtained with white-light continuum. *J. Chem. Phys.* **126**, 165102-165102. (2007).
60 Losev, A. P., Sagun, E. I., Kochubeev, G. A., & Nichiporovich, I. N. Fluorescence quantum yields, lifetimes, and critical distances for energy transfer for chlorophyll α and its pheophytin in solutions. *J. Appl. Spec.* **45**, 798-803 (1986).
61 Leupold, D., Struck, A., Stiel, H., Teuchner, K., Oberländer, S., & Scheer, H. Excited-state properties of 20-chloro-chlorophyll a. *Chem. Phys. Lett.* **170**, 478-484 (1990).
62 Hindman, J. C., Kugel, R., Svirmickas, A., & Katz, J. J. Chlorophyll lasers: Stimulated light emission by chlorophylls and Mg-free chlorophyll derivatives. *Proc. Natl. Acad. Sci.* **74**, 5-9 (1977).
63 Mackinney, G. Absorption of light by chlorophyll solutions. *J. biol. Chem* **140**, 315-322 (1941).

64 Shopova, S. I., Zhu, H., Fan, X. & Zhang, P. Optofluidic ring resonator based dye laser. *Appl. Phys. Lett.* **90**, 221101 (2007).
65 White, I. M., Oveys, H. & Fan, X. Liquid Core Optical Ring Resonator Sensors. *Opt. Lett.* **31**, 1319-1321 (2006).
66 Han, K. *et al.* Fabrication and Testing of Microfluidic Optomechanical Oscillators. *J. Vis. Exp.*, e51497 (2014, doi:10.3791/51497).
67 Lacey, S. *et al.* Versatile microfluidic lasers based on opto-fluidic ring resonators. *Opt. Express* **15**, 15523-15530 (2007).
68 Shopova, S. I. *et al.* Opto-fluidic ring resonator lasers based on highly efficient resonant energy transfer. *Opt. Express* **15**, 12735-12742 (2007).
69 White, I. M. *et al.* Versatile waveguide-coupled opto-fluidic devices based on liquid core optical ring resonators. *Appl. Phys. Lett.* **91**, 241104 (2007).
70 Schaafsma, B. E. *et al.* The clinical use of indocyanine green as a near ‐ infrared fluorescent contrast agent for image ‐ guided oncologic surgery. *J. Surg. Oncol.* **104**, 323-332 (2011).
71 Alander, J. T. *et al.* A review of indocyanine green fluorescent imaging in surgery. *J. Biomed. Imaging* **2012**, 7 (2012).
72 Kokudo, N. & Ishizawa, T. Clinical application of fluorescence imaging of liver cancer using indocyanine green. *Liver Cancer* **1**, 15-21 (2012).
73 Troyan, S. L. *et al.* The FLARE™ intraoperative near-infrared fluorescence imaging system: a first-in-human clinical trial in breast cancer sentinel lymph node mapping. *Ann. Surg. Oncol.* **16**, 2943-2952 (2009).
74 Boni, L. *et al.* Clinical applications of indocyanine green (ICG) enhanced fluorescence in laparoscopic surgery. *Surg. Endosc.* **29**, 2046-2055 (2015).
75 Woitzik, J., Horn, P., Vajkoczy, P. & Schmiedek, P. Intraoperative control of extracranial-intracranial bypass patency by near-infrared indocyanine green videoangiography. *J. Neurosurg.* **102**, 692-698 (2005).
76 Kraft, J. C. & Ho, R. J. Interactions of indocyanine green and lipid in enhancing near-infrared fluorescence properties: the basis for near-infrared imaging in vivo. *Biochem.* **53**, 1275-1283 (2014).
77 Vinegoni, C. *et al.* Indocyanine green enables near-infrared fluorescence imaging of lipid-rich, inflamed atherosclerotic plaques. *Sci. Transl. Med.* **3**, 84ra45-84ra45 (2011).
78 Yoneya, S. *et al.* Binding properties of indocyanine green in human blood. *Invest. Ophthalmol. Vis. Sci.* **39**, 1286-1290 (1998).
79 Zheng, C. *et al.* Indocyanine green-loaded biodegradable tumor targeting nanoprobes for in vitro and in vivo imaging. *Biomaterials* **33**, 5603-5609 (2012).
80 Ogawa, M., Kosaka, N., Choyke, P. L. & Kobayashi, H. In vivo molecular imaging of cancer with a quenching near-infrared fluorescent probe using conjugates of monoclonal antibodies and indocyanine green. *Cancer Res.* **69**, 1268-1272 (2009).
81 Fang, C. *et al.* Illuminating necrosis: From mechanistic exploration to preclinical application using fluorescence molecular imaging with indocyanine green. *Sci. Rep.* **6** (2016).
82 Wang, K. *et al.* Direct wavefront sensing for high-resolution in vivo imaging in scattering tissue. *Nat. Commun.* **6** (2015).
83 Lu, G. & Fei, B. Medical hyperspectral imaging: a review. *J. Biomed. Opt.* **19**, 010901-010901 (2014).

84 Judy, R. P. *et al.* Quantification of tumor fluorescence during intraoperative optical cancer imaging. *Sci. Rep.* **5** (2015).
85 Lue, N. *et al.* Portable optical fiber probe-based spectroscopic scanner for rapid cancer diagnosis: a new tool for intraoperative margin assessment. *PLoS One* **7**, e30887 (2012).
86 Chen, Q. *et al.* Highly sensitive fluorescent protein FRET detection using optofluidic lasers. *Lab Chip* **13**, 2679–2681 (2013).
87 Aas, M., Chen, Q., Jonáš, A., Kiraz, A. & Fan, X. Optofluidic FRET lasers and their applications in novel photonic devices and biochemical sensing. *IEEE J. Sel. Top. Quantum Electron.* **22**, 1-15 (2016).
88 Chen, Q., Ritt, M., Sivaramakrishnan, S., Sun, Y. & Fan, X. Optofluidic lasers with a single molecular layer of gain. *Lab Chip* **14**, 4590-4595 (2014).
89 Lee, W. & Fan, X. Intracavity DNA Melting Analysis with Optofluidic Lasers. *Anal. Chem.* **84**, 9558–9563 (2012).
90 Sabapathy, V., Mentam, J., Jacob, P. M. & Kumar, S. Noninvasive Optical Imaging and In Vivo Cell Tracking of Indocyanine Green Labeled Human Stem Cells Transplanted at Superficial or In-Depth Tissue of SCID Mice. *Stem Cells Int.* **2015** (2015).
91 Balaiya, S., Brar, V. S., Murthy, R. K. & Chalam, K. Effects of Indocyanine green on cultured retinal ganglion cells in-vitro. *BMC Res. Notes* **2**, 236 (2009).
92 Yamada, T. *et al.* In vitro differentiation of embryonic stem cells into hepatocyte ‐ like cells identified by cellular uptake of indocyanine green. *Stem Cells* **20**, 146-154 (2002).
93 Abels, C., Karrer, S. & BÃ, W. Indocyanine green and laser light for the treatment of AIDS-associated cutaneous Kaposi's sarcoma. *Br. J. Cancer* **77**, 1021 (1998).
94 Holt, D. *et al.* Intraoperative near-infrared fluorescence imaging and spectroscopy identifies residual tumor cells in wounds. *J. Biomed. Opt.* **20**, 076002-076002 (2015).
95 Matthes, R. *et al.* Revision of guidelines on limits of exposure to laser radiation of wavelengths between 400 nm and 1.4 µm. *Health Phys.* **79**, 431-440 (2000).
96 Berezin, M. Y. *et al.* Rational approach to select small peptide molecular probes labeled with fluorescent cyanine dyes for in vivo optical imaging. *Biochem.* **50**, 2691-2700 (2011).
97 Desmettre, T., Devoisselle, J. & Mordon, S. Fluorescence properties and metabolic features of indocyanine green (ICG) as related to angiography. *Surv Ophthalmol.* **45**, 15-27 (2000).
98 Jung, B., Vullev, V. I. & Anvari, B. Revisiting Indocyanine green: effects of serum and physiological temperature on absorption and fluorescence characteristics. *IEEE J. Sel. Top. Quant.* **20**, 149-157 (2014).
99 Mihara, M. *et al.* Uterus autotransplantation in cynomolgus macaques: intraoperative evaluation of uterine blood flow using indocyanine green. *Hum. Reprod.* **26**, 3019-3027 (2011).
100 Unno, N. *et al.* Indocyanine green fluorescence angiography for intraoperative assessment of blood flow: a feasibility study. *Eur. J. Vasc. Endovasc. Surg.* **35**, 205-207 (2008).
101 Cherrick, G. R., Stein, S. W., Leevy, C. M. & Davidson, C. S. Indocyanine green: observations on its physical properties, plasma decay, and hepatic extraction. *Journal of Clinical Investigation* **39**, 592 (1960).
102 Agarwal, A. *Fundus fluorescein and indocyanine green angiography: a textbook and atlas*. (SLACK Incorporated, 2007).
103 Lee, S. *et al.* Fully integrated high-speed intravascular optical coherence tomography/near-infrared fluorescence structural/molecular imaging in vivo using a clinically available near-

infrared fluorescence–emitting indocyanine green to detect inflamed lipid-rich atheromata in coronary-sized vessels. *Circ. Cardiovasc. Interv.* **7**, 560-569 (2014).
104 van den Biesen, P. R., Jongsma, F. H., Tangelder, G. J. & Slaaf, D. W. Yield of fluorescence from indocyanine green in plasma and flowing blood. *Ann. Biomed. Eng.* **23**, 475-481 (1995).
105 Mordon, S., Devoisselle, J. M., Soulie-Begu, S. & Desmettre, T. Indocyanine green: physicochemical factors affecting its fluorescencein vivo. *Microvascular research* **55**, 146-152 (1998).
106 Wang, W. *et al.* Optofluidic laser array based on stable high-Q Fabry–Pérot microcavities. *Lab Chip* **15**, 3862–3869 (2015).
107 Ziegler, J., Djiango, M., Vidal, C., Hrelescu, C. & Klar, T. A. Gold nanostars for random lasing enhancement. *Optics express* **23**, 15152-15159 (2015).
108 Noginov, M. A. *et al.* Demonstration of a spaser-based nanolaser. *Nature* **460**, 1110-1113 (2009).
109 Liu, P. *et al.* Dextran based sensitive theranostic nanoparticles for near-infrared imaging and photothermal therapy in vitro. *Chem. Comm.* **49**, 6143-6145 (2013).
110 Zheng, J. *et al.* A multimodal nano agent for image-guided cancer surgery. *Biomater.* **67**, 160-168 (2015).
111 Mordant, D. *et al.* Spectral imaging of the retina. *Eye* **25**, 309-320 (2011).
112 Sun, Y., Shopova, S. I., Wu, C.-S., Arnold, S. & Fan, X. Bioinspired optofluidic FRET lasers via DNA scaffolds. *Proc. Natl. Acad. Sci. USA* **107**, 16039-16042 (2010).
113 Schubert, M. *et al.* Lasing within live cells containing intracellular optical micro-resonators for barcode-type cell tagging and tracking. *Nano Lett.* **15**, 5647-5652 (2015).
114 Nizamoglu, S. *et al.* A Simple Approach to Biological Single-Cell Lasers Via Intracellular Dyes. *Adv. Opt. Mater.* **3**, 1197–1200 (2015).
115 Caixeiro, S., Gaio, M., Marelli, B., Omenetto, F. G. & Sapienza, R. Silk‐Based Biocompatible Random Lasing. *Adv. Opt. Mater.* **4**, 998-1003 (2016).
116 Polson, R. & Vardeny, Z. V. Cancerous tissue mapping from random lasing emission spectra. *J. Opt.* **12**, 024010 (2010).
117 Liu, X. *et al.* Random laser action from a natural flexible biomembrane-based device. *Journal of Modern Optics* **63**, 1248-1253 (2016).
118 Wang, C.-S., Chang, T.-Y., Lin, T.-Y. & Chen, Y.-F. Biologically inspired flexible quasi-single-mode random laser: An integration of Pieris canidia butterfly wing and semiconductors. *Sci. Rep.* **4**, 6736 (2014).
119 Chinen, A. B. *et al.* Nanoparticle probes for the detection of cancer biomarkers, cells, and tissues by fluorescence. *Chemical reviews* **115**, 10530-10574 (2015).
120 Vendrell, M., Maiti, K. K., Dhaliwal, K. & Chang, Y.-T. Surface-enhanced Raman scattering in cancer detection and imaging. *Trends in biotechnology* **31**, 249-257 (2013).
121 Muthana, M. *et al.* Directing cell therapy to anatomic target sites in vivo with magnetic resonance targeting. *Nature Commun.* **6**, 8009 (2015).
122 Orth, A., Tomaszewski, M. J., Ghosh, R. N. & Schonbrun, E. Gigapixel multispectral microscopy. *Optica* **2**, 654-662 (2015).
123 Gerdes, M. J. *et al.* Highly multiplexed single-cell analysis of formalin-fixed, paraffin-embedded cancer tissue. *Proc. Natl. Sci. Acad. USA* **110**, 11982-11987 (2013).
124 Zhou, L. *et al.* Single-band upconversion nanoprobes for multiplexed simultaneous in situ molecular mapping of cancer biomarkers. *Nature Commun.* **6** (2015).

125 Zavaleta, C. L. *et al.* Multiplexed imaging of surface enhanced Raman scattering nanotags in living mice using noninvasive Raman spectroscopy. *Proc. Natl. Sci. Acad. USA* **106**, 13511-13516 (2009).
126 Clark, B. A., Alloosh, M., Wenzel, J. W., Sturek, M. & Kostrominova, T. Y. Effect of diet-induced obesity and metabolic syndrome on skeletal muscles of Ossabaw miniature swine. *Am. J. Physiol. Endocrinol. Metab.* **300**, E848-E857 (2011).
127 Spangenburg, E. E., Pratt, S. J., Wohlers, L. M. & Lovering, R. M. Use of BODIPY (493/503) to visualize intramuscular lipid droplets in skeletal muscle. *BioMed. Res. Intl.* **2011** (2011).
128 Scriven, D. R., Dan, P. & Moore, E. D. Distribution of proteins implicated in excitation-contraction coupling in rat ventricular myocytes. *Biophys. J.* **79**, 2682-2691 (2000).
129 Bedner, E. *et al.* High affinity binding of fluorescein isothiocyanate to eosinophils detected by laser scanning cytometry: a potential source of error in analysis of blood samples utilizing fluorescein-conjugated reagents in flow cytometry. *Cytometry* **36**, 77-82 (1999).
130 Agarwal, S. R., Clancy, C. E. & Harvey, R. D. Mechanisms restricting diffusion of intracellular cAMP. *Sci. Rep.* **6** (2016).
131 Galas, J. C., Peroz, C., Kou, Q. & Chen, Y. Microfluidic dye laser intracavity absorption. *Appl. Phys. Lett.* **89**, 224101 (2006).
132 Marquez, G., Wang, L. V., Lin, S.-P., Schwartz, J. A. & Thomsen, S. L. Anisotropy in the absorption and scattering spectra of chicken breast tissue. *Appl. Opt.* **37**, 798-804 (1998).
133 Bandres, M. A. & Gutiérrez-Vega, J. C. Ince–Gaussian beams. *Opt. Lett.* **29**, 144-146 (2004).
134 Schwarz, U. T., Bandres, M. A. & Gutiérrez-Vega, J. C. Observation of Ince–Gaussian modes in stable resonators. *Opt. Lett.* **29**, 1870-1872 (2004).
135 Tearney, G. *et al.* Determination of the refractive index of highly scattering human tissue by optical coherence tomography. *Opt. Lett.* **20**, 2258-2260 (1995).
136 Kienle, A. & Hibst, R. Light guiding in biological tissue due to scattering. *Phys. Rev. Lett.* **97**, 018104 (2006).
137 Ranasinghesagara, J. & Yao, G. Effects of inhomogeneous myofibril morphology on optical diffraction in single muscle fibers. *J. Opt. Soc. Am. A* **25**, 3051-3058 (2008).
138 Jacques, S. L. Optical properties of biological tissues: a review. *Phys. Med. Biol.* **58**, R37-R61 (2013).
139 Zijp, J. R. & ten Bosch, J. J. Optical properties of bovine muscle tissue in vitro; a comparison of methods. *Physics in medicine and biology* **43**, 3065 (1998).
140 Atencio, J. D., y Montiel, S. V. & Jacques, S. *Monte Carlo modeling of light propagation in neonatal skin*. (INTECH Open Access Publisher, 2011).
141 Mack, C. P., Somlyo, A. V., Hautmann, M., Somlyo, A. P. & Owens, G. K. Smooth muscle differentiation marker gene expression is regulated by RhoA-mediated actin polymerization. *J. Biol. Chem.* **276**, 341-347 (2001).
142 Siegman, A. E. *Lasers*. (University Science Books, 1986).
143 Hunger, D. *et al.* A fiber Fabry-Perot cavity with high finesse. *New J. Phys.* **12**, 065038 (2010).
144 Hunger, D., Deutsch, C., Barbour, R. J., Warburton, R. J. & Reichel, J. Laser micro-fabrication of concave, low roughness features in silica. *AIP Advances* **2**, 012119 (2012).
145 Kiraz, A., Chen, Q. & Fan, X. Optofluidic Lasers with Aqueous Quantum Dots. *ACS Photon.* **2**, 707-713 (2015).

146 Zink, D., Fischer, A. H. & Nickerson, J. A. Nuclear structure in cancer cells. *Nat. Rev. Cancer* **4**, 677-687 (2004).
147 Swarup, V. & Rajeswari, M. Circulating (cell-free) nucleic acids–a promising, non-invasive tool for early detection of several human diseases. *FEBS Lett.* **581**, 795-799 (2007).
148 Schwarzenbach, H., Hoon, D. S. & Pantel, K. Cell-free nucleic acids as biomarkers in cancer patients. *Nat. Rev. Cancer* **11**, 426-437 (2011).
149 Morgan, M. A. & Shilatifard, A. Chromatin signatures of cancer. *Genes & Dev.* **29**, 238-249 (2015).
150 Lo, H. & Hung, M. Nuclear EGFR signalling network in cancers: linking EGFR pathway to cell cycle progression, nitric oxide pathway and patient survival. *Br. J. Cancer* **94**, 184-188 (2006).
151 Traynor, A. M. *et al.* Nuclear EGFR protein expression predicts poor survival in early stage non-small cell lung cancer. *Lung Cancer* **81**, 138-141 (2013).
152 Wang, L. *et al.* Evaluation of Raman spectroscopy for diagnosing EGFR mutation status in lung adenocarcinoma. *Analyst* **139**, 455-463 (2014).
153 Sarkis, A. S. *et al.* Prognostic value of p53 nuclear overexpression in patients with invasive bladder cancer treated with neoadjuvant MVAC. *J. Clin. Oncol.* **13**, 1384-1390 (1995).
154 Manne, U. *et al.* Prognostic significance of Bcl-2 expression and p53 nuclear accumulation in colorectal adenocarcinoma. *Int. J. Cancer* **74**, 346-358 (1997).
155 Porter, L. A. & Donoghue, D. J. Cyclin B1 and CDK1: nuclear localization and upstream regulators. *Prog. Cell Cycle Res.* **5**, 335-348 (2003).
156 Konety, B. R. & Getzenberg, R. H. Nuclear structural proteins as biomarkers of cancer. *J. Cell. Biochem.* **75**, 183-191 (1999).
157 Rakha, E. A. *et al.* Prognostic markers in triple‐negative breast cancer. *Cancer* **109**, 25-32 (2007).
158 Dekanić, A. *et al.* Strong nuclear EGFR expression in colorectal carcinomas is associated with cyclin-D1 but not with gene EGFR amplification. *Diagn. Pathol.* **6**, 1 (2011).
159 Pereira, N. B. *et al.* Nuclear localization of epidermal growth factor receptor (EGFR) in ameloblastomas. *Oncotarget* **6**, 9679 (2015).
160 Xia, W. *et al.* Nuclear expression of epidermal growth factor receptor is a novel prognostic value in patients with ovarian cancer. *Mol. Carcinog.* **48**, 610-617 (2009).
161 Müller, W., Schneiders, A., Hommel, G. & Gabbert, H. Prognostic value of bcl-2 expression in gastric cancer. *Anticancer Res.* **18**, 4699-4704 (1997).
162 Beer, D. G. *et al.* Gene-expression profiles predict survival of patients with lung adenocarcinoma. *Nat. Med.* **8**, 816-824 (2002).
163 Ludwig, J. A. & Weinstein, J. N. Biomarkers in cancer staging, prognosis and treatment selection. *Nat. Rev. Cancer* **5**, 845-856 (2005).
164 Irish, J. M., Kotecha, N. & Nolan, G. P. Mapping normal and cancer cell signalling networks: towards single-cell proteomics. *Nat. Rev. Cancer* **6**, 146-155 (2006).
165 Levenson, R. M., Borowsky, A. D. & Angelo, M. Immunohistochemistry and mass spectrometry for highly multiplexed cellular molecular imaging. *Lab Invest.* **95**, 397-405 (2015).
166 Collins, L. G., Haines, C., Perkel, R. & Enck, R. E. Lung cancer: diagnosis and management. *Am. Fam. Physician* **75**, 56-63 (2007).
167 Silvestri, G. A. *et al.* Noninvasive staging of non-small cell lung cancer: ACCP evidenced-based clinical practice guidelines (2nd ed.). *Chest* **132**, 178S-201S (2007).

168 Yu, K.-H. *et al.* Predicting non-small cell lung cancer prognosis by fully automated microscopic pathology image features. *Nat. Commun.* **7** (2016).
169 Vansteenkiste, J., Dooms, C. & De Leyn, P. Early stage non-small-cell lung cancer: challenges in staging and adjuvant treatment: evidence-based staging. *Ann. Oncol.* **21**, vii189-vii195 (2010).
170 Shi, S.-R., Cote, R. J. & Taylor, C. R. Antigen retrieval immunohistochemistry: past, present, and future. *J. Histochem. Cytochem.* **45**, 327-343 (1997).
171 Arnould, L. *et al.* Trastuzumab-based treatment of HER2-positive breast cancer: an antibody-dependent cellular cytotoxicity mechanism. *Brit. J. Cancer* **94**, 259-267 (2006).
172 Wu, L. & Qu, X. Cancer biomarker detection: recent achievements and challenges. *Chem. Soc. Rev.* **44**, 2963-2997 (2015).
173 Gourley, P. Semiconductor microlasers: A new approach to cell–structure analysis. *Nat. Med.* **2**, 942-944 (1996).
174 Wei, Y. *et al.* Starch-Based Biological Microlasers. *ACS nano* (2016).
175 Beljanski, M. *The Regulation of DNA Replication and Transcription*. (Demos Medical Publishing, 2013).
176 Lane, A. N. & Fan, T. W.-M. Regulation of mammalian nucleotide metabolism and biosynthesis. *Nucleic Acids Res.* **43**, 2466-2485 (2015).
177 Pliss, A., Kuzmin, A. N., Kachynski, A. V. & Prasad, P. N. Nonlinear optical imaging and Raman microspectrometry of the cell nucleus throughout the cell cycle. *Biophys. J.* **99**, 3483-3491 (2010).
178 Bremnes, R. M. *et al.* The role of tumor stroma in cancer progression and prognosis: emphasis on carcinoma-associated fibroblasts and non-small cell lung cancer. *J. Thorac. Oncol.* **6**, 209-217 (2011).
179 Finak, G. *et al.* Stromal gene expression predicts clinical outcome in breast cancer. *Nat. Med.* **14**, 518-527 (2008).
180 Calon, A. *et al.* Stromal gene expression defines poor-prognosis subtypes in colorectal cancer. *Nat. Genet.* **47**, 320-329 (2015).
181 Grilley-Olson, J. E. *et al.* Validation of interobserver agreement in lung cancer assessment: hematoxylin-eosin diagnostic reproducibility for non-small cell lung cancer: the 2004 World Health Organization classification and therapeutically relevant subsets. *Arch. Pathol. Lab. Med.* **137**, 32-40 (2012).
182 Grienberger, C. & Konnerth, A. Imaging calcium in neurons. *Neuron* **73**, 862-885 (2012).
183 Göbel, W. & Helmchen, F. In vivo calcium imaging of neural network function. *Physiology* **22**, 358-365 (2007).
184 Stosiek, C., Garaschuk, O., Holthoff, K. & Konnerth, A. In vivo two-photon calcium imaging of neuronal networks. *Proc. Natl. Acad. Sci.* **100**, 7319-7324 (2003).
185 Marom, A., Shor, E., Levenberg, S. & Shoham, S. Spontaneous Activity Characteristics of 3D "Optonets". *Front. in Neurosci.* **10** (2016).
186 Foster, B. L. *et al.* Spontaneous neural dynamics and multi-scale network organization. *Front. in Syst. Neurosci.* **10** (2016).
187 Katona, G. *et al.* Fast two-photon in vivo imaging with three-dimensional random-access scanning in large tissue volumes. *Nat. Meth.* **9**, 201-208 (2012).